Yong Geng

Master

Old Cellulose for New Multifunctional Networks

Dissertação para obtenção do Grau de Doutor em
Ciência e Engenharia de Materiais

Orientador: Maria Helena Figueiredo Godinho,
Professora Auxiliar com Agregação, FCT/UNL
Co-orientador: Pedro Lúcio Maia Marques de Almeida,
Professor Adjunto, ISEL

Júri:

Presidente: Prof. Doutor Pedro Manuel Corrêa Calvente Barahona
Arguente(s): Prof. Doutor Eugene Terentjev
Prof. Doutor Pedro Manuel Alves Patrício da Silva
Vogais: Prof. Doutor Rogério Manuel dos Santos Simões
Prof. Doutor João Luís Maia Figueirinhas
Prof. Doutor Carlos Manuel dos Santos Rodrigues da Cruz
Prof. Doutora Maria Helena Figueiredo Godinho
Prof. Doutora Maria Teresa Varanda Cidade
Prof. Doutora Maria Madalena Alves Campos de Sousa Dionísio Andrade
Prof. Doutor Pedro Lúcio Maia Marques de Almeida

FACULDADE DE CIÊNCIAS E TECNOLOGIA
UNIVERSIDADE NOVA DE LISBOA

September 2013

Acknowledgements

How time flies! It has been almost four years since I came to Portugal - a totally new world for me. I still remember the picture: four years ago at 1:00 AM in the Lisbon airport my supervisors and my friends waiting for me with my name written on a paper. My life as a PhD student started from that point on. Now, I am going to submit my thesis on time, which would be impossible without the help of many people.

Firstly, I would like to thank my supervisors Prof. Maria Helena Godinho and Prof. Pedro Marques de Almeida. They changed my life and gave me so much help here. I still remember two years before, when I had the accident even during the surgery process in the hospital, they took care of me very well just like family to make me feel better, which I will remember for my whole life. I would say without their help I couldn´t have lived here. Also, they provided many valuable ideas and advices during my research and with the overall thesis carefully revision. During my work for the past four years, my supervisors didn´t just tell me how to do research but also aided me to be a kind and responsible person in this career as well as in this different world. However my life would be, they will impact my whole life and will be my supervisors forever.

Secondly, I also would like to thank Prof. Carlos Manuel Cruz for his help during my first year of research as BI grant researcher. I also express my thanks to Prof. João Luis Figueirinhas and Prof. António Gabriel Feio for their valuable discussions, advices and collaboration, which were important for my research and helped in some parts of my PhD work.

I also express my thankfulness to Prof. Eugene Terentjev from Cambridge, Prof. Peter Palffy-Muhoray and Prof. Oleg Lavrentovich from Kent University and Prof. Slobodan Zumer from Slovenia for their collaboration and help.

I would like to thank Prof. Pedro Brogueira for his assistance on AFM measurements.

I would like to thank my friends and colleagues Prof. Maria Teresa Cidade, Prof. João Paulo Borges, Dr. Luís Filipe Pinto, Dr. Ana Catarina Trindade, Dr. João Paulo Canejo, Dr. Susete Fernandes, Dr. Sudarshan Kundu, Dr. Alexandra Carvalho, Dr. Luis Ever Aguirre, Ana Baptista and all the other friends that are too many to mention. They always gave me warmly encouragement, help and spent with me a lot of their time.

I am also obliged to the Professors and colleagues from the Departamento de Ciência dos Materiais of FCT/UNL and also from CENIMAT/I3N.

I acknowledge Portugal to give me the education through the support provided by the Portuguese Science and Technology Foundation with the grant of SFRH/BD/63574/2009. Portugal is such a

beautiful and peaceful country, and it is my second homeland in my mind. It is much developed compare to China and I learnt a lot from here. I am proud of it.

I would like to acknowledge the Research Projects with references: PTDC/CTM/099595/2008, PTDC/CTM-POL/1484/2012, PTDC/CTM/101776/2008, PTDC/FIS/110132/2009, and PEst-C/CTM/LA0025/2011 (Strategic Project - LA 25-2011-2012), from the Portuguese Foundation for Science and Technology, for partially support the research performed on the scope of my thesis.

I would like to express my thankfulness to Prof. Liangbin Li. He introduced me to polymer science and helped me to come and to study in Portugal.

I would like to thank my parents and sister for their incessantly support and for their always crucial always presence in my life. I am proud of them.

Last but not least, I wish all the people mentioned above happy and healthy forever and I will fight all my life in order to not disappoint them.

Yong Geng

Lisboa

Abstract

Cellulose is considered to be the most abundant and renewable natural polymer on earth. It is the main component of plant cells. The exploration of the utility and applications of this material and its derivatives has never stopped since human´s birth.

It is well known that cellulose based materials can generate films and fibers, which can be, for instance, produced from cellulosic solutions. The Cellulose rich chemical structure allows different behaviors of the polymer in solution, which is the driving force for diverse films and fibers features.

The main goal of this work is the manufacture and characterization of new application of the renewable cellulosic-based materials, which are at the origin of stimuli-responsive and/or functional soft films and fibers. The several materials obtained have in common the main chain cellulose backbone but present different liquid crystalline properties.

Firstly rheology coupled to nuclear magnetic resonance techniques (rheo-NMR) were used to characterize a cellulose-water based liquid crystalline solution in order to establish structure/properties relationships, which were the basis to improve the design of films and fibers produced in the framework of this work. The results achieved were at the origin of a paper published in Macromolecules.

Then films were produced and due to their structure and enhanced mechanical properties, different applications were realized by producing cellulosic gratings, which mimic the periodic structures that can be found in some petals of plants and a soft cellulose moisture motor was built for the first time. Two manuscripts were published, one related to the grating mimics, in Macromolecular Chemistry and Physics, and the other one dedicated to the mechanical properties and the bending of a cellulosic film controlled by moisture action in Scientific Reports (Nature Publishing Group).

Concerning cellulosic fibers, two methods were selected to fabricate micro/nano networks. In order to produce suspended aligned arrays, electrospinning was chosen due to its versatility. On the obtained nano/micro cylinders, nematic and cholesteric droplets were threaded producing necklaces of liquid crystal beads for the first time. The fiber changes not only the topology of the droplet but also distorts its spherical shape to an approximately ellipsoidal droplet. An additional cylindrical surface with planar anchoring along the droplet's long axis was also added. Designing nematic and cholesteric liquid crystal microdroplets on thin long threads opened new routes to produce fiber waveguides decorated with complex microresonators. Two Soft Matter scientific papers were published based on this work (One was chosen as the cover of that issue).

Finally, nano-fibers produced by cellulose acid hydrolises were prepared and a new electro-optical sensor was built up and characterized and the results published in Liquid Crystals journal.

Throughout this work Landau-de-Gennes theory was used in order to interpret and understand some of the experimental results achieved.

Content

List of Figures

List of Tables

List of Abbreviations

ε_0	Dielectric constant of vacuum
$\Delta\chi$	Anisotropy in the magnetic susceptibility
$\Delta\varepsilon$	Dielectric anisotropy
$\overline{Ms}$	Average moles of substitution
3D	Three dimensional
5CB	*4'-n-pentyl-4-cyanobiphenyl*
5CB*	*(s)-4'-(3-methylpentyl)-4-cyanobiphenyl*
AC	Alternating current
AFM	Atomic force microscopy
APC	Acetoxypropylcellulose
B	Magnetic field
BNC	Bacterial nanocellulose
BS	Bipolar structure
CA	Cellulose acetate
CLC	Cholesteric liquid-crystal
DC	Direct current
$\overline{DS}$	Average of degree of substitution
DMac	Dimethylacetamide
DP	Degree of polymerization
DS	Degree of substitution
s	Defect strength
DSS	Diametric spherical structure
E	Electric field
F	Free energy
HPC	Hydroxypropylcellulose
HEC	Hydroxyethylcellulose
K	Elastic constant
K_1	Splay elastic constant
K_2	Twist elastic constant
K_3	Bend elastic constant
λ	Wavelength
LC(s)	Liquid crystal(s)
LCD	Liquid crystal display
LCN	Liquid crystal networks
LCP	Liquid-crystalline polymer
LCST	Lower critical solution temperature
LDG	Landau-de Gennes
MCC	Microcrystalline cellulose
MFC	Microfibrillated cellulose
MRI	Magnetic resonance imaging
$\overline{MS}$	Average molar substitution
$\overline{Mw}$	Average molecular weight

N*	Chiral nematic
NCC	Nanocrystalline cellulose
NI	Nematic to isotropic
NLC	Nematic liquid crystal
NMR	Nuclear Magnetic resonance
p	Pitch
P	Pressure
Par	Parallel
PBS	Planar bipolar structure
PEEK	Polyether ether ketone
PDLC	Polymer dispersed liquid crystal
Per	Perpendicular
POM	Polarized optical microscopy
Q	Symmetric tensor order parameter
q_0	Wave number
r	Radius
Rheo-NMR	Rheology coupled with Nuclear Magnetic Resonance
RSS	Radial spherical structure
S	Order parameter
SALS	Small angle light scattering
SEM	Scanning electronic microscopy
TEM	Transmission electron microscopy
TGB	Twist grain boundary
wt % or *% w/w*	Weight percentage

Chapter 1 Introduction

In this introductory chapter we recall the essential aspects of cellulose related to the formation of self-assembled systems as well as the basic knowledge of nematic and cholesteric liquid crystals. These notes will allow the introduction of the main topic of this work, which was focused on studies and applications of cellulose-based liquid crystalline systems.

1.1 Cellulose and Cellulose Derivatives

Anselme Payen in 1838 found a fibrous component in higher plant cell walls[1], with a unique chemical structure, which he named cellulose. Cellulose is the most abundant and renewable organic material on earth. It is the main component structural material by which plants, trees, as well as grasses sustain the strength to stay upright or stand loads.[2] This structural material is organized as microfibrils, which are linked together to form fibers. It can be biosynthesized by some living organisms ranging from higher to lower plants, some amoebae, sea animals, bacteria and fungi.[3,4]

In this part of chapter 1, we decided to first introduce cellulose at a molecular level, which is crucial to analyze higher structural organizations of this macromolecule: the supramolecular level comprising crystal and molecular structures and hydrogen-bonding associations and the morphological organization of the crystals into microfibrils, layers, cell walls and tissues. The fabrication and

application of nanocrystals, as well as cellulose derivatives are also addressed in order to introduce the liquid crystalline chiral cellulosic systems in the second part of this chapter.

1.1.1 Cellulose

The history of the structural study of cellulose goes hand in hand with the history of polymer science. In fact cellulose is the most extensively studied polymer during the introduction of the macromolecular concept. The macromolecular nature of cellulose was determined at the beginning of the 20th century. [5]

1.1.1.1 Molecular Structure

Cellulose consists of a linear polysaccharide composed of *β-D*-glucopyranose units linked together by *β*-1-4- linkages [6]. (The basic chemical structure of cellulose is presented in Figure 1-1)

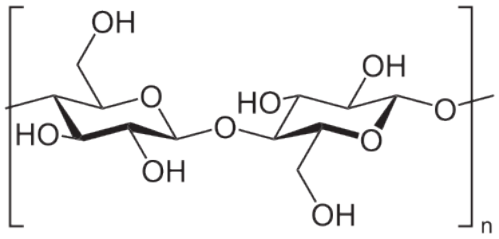

Figure 1-1 Basic chemical structure of cellulose showing cellobiose repeat unit. [7]

The established numbering of the carbon and oxygen atoms in the ring is shown in Figure 1-2. There are two attached oxygen atoms (O1 and O5) at C1, hydroxyl substituents (O2 and O3) at C2 and C3, one attached oxygen (O4) atom at C4, and one hydroxymethyl (C6 and O6) group at C5. Inter-unit linkages are insured by 1 and 4 positions. The oxygen atom at the glycosidic bond is O1, the oxygen in the ring is O5, O2 and O3 are those in the secondary alcohols and O6 is in the primary alcohol. The acetal center at C1 exists along the entire polymeric structure except at one end of the macromolecule where it is a reducing hemiacetal center. [8]

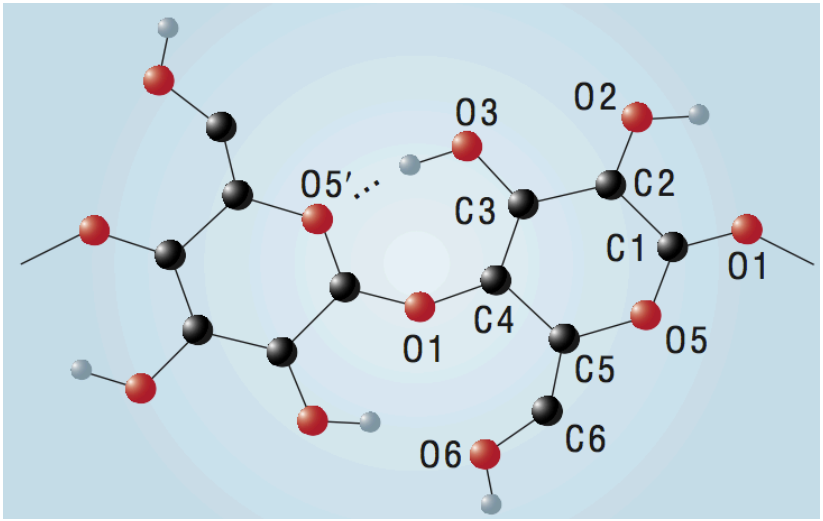

Figure 1-2 Numbering system for carbon and oxygen atoms in two consecutive glucosyl units of cellulose. The O3–H···O5 hydrogen bond shown is present in all crystalline forms of cellulose, but the pattern of hydrogen bonding from O2 and O6 varies. Hydrogen atoms are shown in grey.[8]

The basic unit of cellulose results from cyclization of *D*-glucose into the six membered pyranose shape. Two anomers result from cyclization. The stereoisomer β equatorial configuration is found in cellulose molecular structure. The hydroxyl groups and their equatorial conformation on glucose residues as well as their ability to form hydrogen bonds play a major role in directing the crystalline packing and also in governing the physical properties of cellulose. The inter- and intra-molecular hydrogen bonds as can be seen in Figure 1-2 contribute differently to the formation of microfibrils with high strength. The O3–H···O5 hydrogen bond can be found in all crystal types, while the hydrogen bonds between O2 and O6 vary in different type of crystals, as will be discussed in the next section. [3]

Many properties of cellulose depend on the degree of polymerization, the number of basic units that makes up the polymer molecules in Figure 1-1 (*n*), which depends on cellulose source and treatment. [2]

Cellulose from wood pulp has typical chain lengths between 300 and 1700 units; cotton and other plant fibers as well as bacterial celluloses have chain lengths ranging from 800 to 10,000 units. Typically, native celluloses have *n* values higher than regenerated celluloses. Purification methods seem to reduce the cellulose degree of polymerization to the value of 2500. [3]

1.1.1.2 Cellulose Supramolecular Structure

X-ray diffraction patterns of native cellulose were the first scientific evidence of the existence of crystalline regions. Cellulose can form several kinds of crystalline structures, for example *I*, *II*, III_I and

IV$_1$ defined by different unit cell parameters (Table 1-1). Nature cellulose consists of cellulose *I*, which is a composite of two allomorphs I_α and I_β. I_α can be converted into I_β, which is more stable, by annealing. Cellulose produced by bacteria and algae is enriched in I_α while cellulose of higher plants consists mainly of I_β. Cellulose in regenerated cellulose fibers is cellulose *II*. The conversion of cellulose *I* to cellulose *II* is not reversible, suggesting that cellulose *I* is metastable and cellulose *II* is stable. With various chemical treatments it is possible to produce cellulose *III* and cellulose *IV* structures.[3,9]

Table 1-1 Unit cells for cellulose I_α, I_β, II, III_1, and IV_1.[3]

Type	Space group	Chains numbers	Unit cell					
			a (Å)	*b* (Å)	*c* (Å)	α (°)	β (°)	γ (°)
I_α	P1	1	6.717	5.962	10.4	118.08	114.8	80.37
I_β	$P2_1$	2	7.784	8.201	10.38	90	90	96.55
II	$P2_1$	2	8.03[10]	9.04	10.36	90	90	117.1
III_1	$P2_1$	1	4.450	7.85	10.31	90	90	105.1
IV_1	P1	2	8.03	8.13	10.34	90	90	90

Cellulose I_α and I_β structures were investigated in detail and it was found that cellulose chain can approximate to a flat ribbon, with alternate glucose units facing in opposite directions. They are locked in this position by a hydrogen bond between a hydroxyl group (O3–H) of one glucose unit and the ring oxygen (O5′) of the next. All the cellulose chains lie parallel, hydrogen-bonded edge to edge.[8] The sheets of chains so formed are stacked on top of one another with a stagger, along the microfibril, that differs between the I_α and I_β forms. Most of these features were already known or guessed, but there was a mystery about the forces that held sheets of chains together in a stack.[8] Hydrophobic bonding had been suggested because[8], with the polar hydroxyl groups ranged along the edges of each ribbon-like chain, its upper and lower faces are relatively nonpolar. However *Nishiyama et al.*[11,12] point out that the chains are also correctly configured to provide an ordered multiplicity of weak C–H···O hydrogen bonds from one sheet to the next as shown in Figure 1-3.

Nishiyama et al.[11,12] determined the crystal and molecular structure together with the hydrogen-bonding system in cellulose using synchrotron and neutron diffraction data recorded from oriented fibrous samples prepared by aligning cellulose microcrystals from tunicin[11] and the cell wall of the freshwater alga Glaucocystis nostochinearum[12]. The X-ray data were used to determine the C and O atom positions.[11,12] The positions of hydrogen atoms involved in hydrogen bonding were determined from a Fourier-difference analysis using neutron diffraction data collected from hydrogenated and deuterated samples. Each crystalline form has two alternative hydrogen-bond networks that differ only in the positions of the hydroxyl protons on O2 and O6. For I_α the resulting structure is a one-chain triclinic unit cell with all glucosyl linkages and hydroxymethyl groups identical. However, adjacent

sugar rings alternate in conformation giving the chain a cellobiosyl as repeating chain unit. The chains organize in sheets packed in a "parallel-up" fashion. Adjacent chains are linked by a *zig-zag*, repeating O–H···O–H··· motif. For I_β type crystal, the structure consists of two parallel chains having slightly different conformations and organized in sheets packed in a "parallel-up" fashion, with all hydroxymethyl groups adopting the *tg* conformation.[8,11,12]

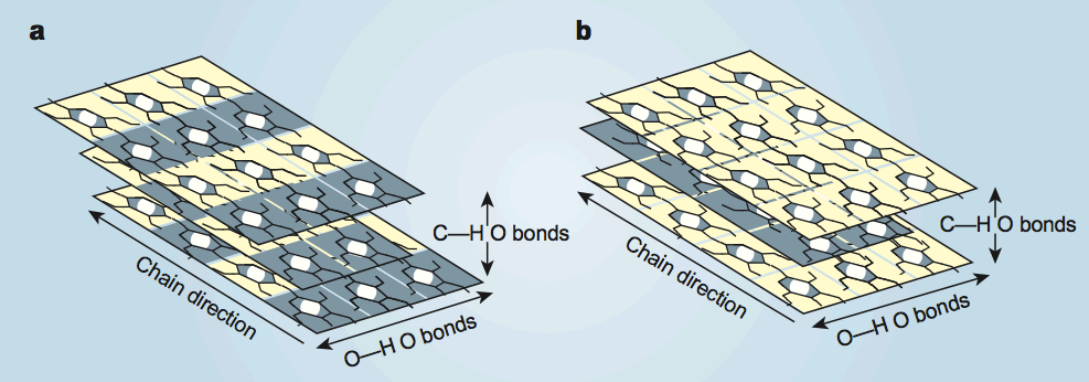

Figure 1-3 Symmetry and directions of hydrogen bonding in cellulose. **a**, Cellulose I_α, in which all chains are crystallographically identical but alternating glucose units in each chain, shaded grey and yellow, differ slightly in conformation. **b**, Cellulose I_β, in which chains of two distinct kinds are arranged in alternating sheets. Chains passing through the origin and centre of the unit cell are shaded respectively yellow and grey.[8]

1.1.1.3 Cellulose Morphological Structure

The morphological structure of cellulose describes the organization of crystals into microfibrils, cell walls, fibers, tissues and other cellulosic arrangements. Nature cellulose occurs generally as fibers while regenerated cellulose can be transformed into different materials as fibers, films or other products with morphology largely different from that of native cellulose. The morphology of these regenerated products depends not only on the processing conditions but also on the solvent used and the regeneration process.

The cellulose nature micro fibril is assumed to be the basic structural component of cellulose, formed during the biosynthesis. Each micro fibril can be considered as a string of cellulose crystals linked along the micro fibril axis by disordered amorphous domains, *e. g.*, twists and kinks.[6] Actually, the chains aggregate to form a fibril, which is a long thread-like bundle of molecules laterally stabilized by intermolecular hydrogen bonds, as shown in Figure 1-4. Individual cellulose microfibrils can have diameters ranging from 2 to 20 *nm* depending on the cellulose source. For example it was found that the *Valonia* cellulose microfibrils, have 20 *nm* width and are much larger than those found for wood holocellulose.[6,14]

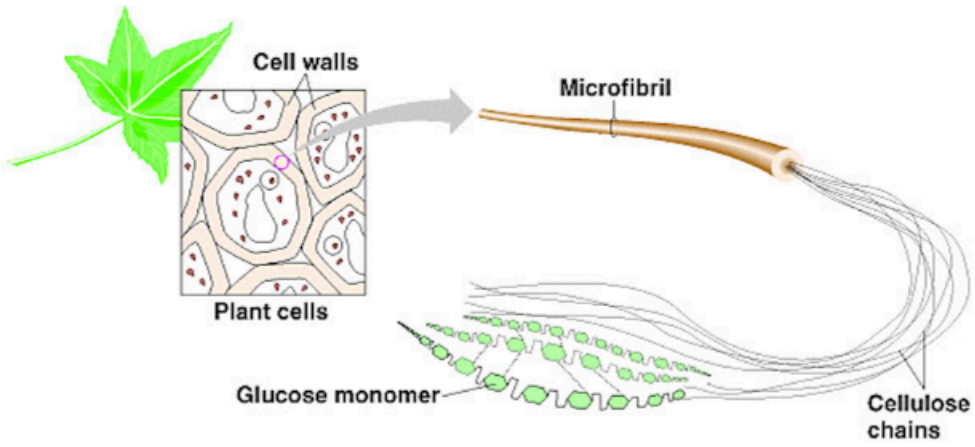

Figure 1-4 Scheme of the cellulose cell wall and micro fibril organization.[13]

The hydrolysis of cellulose into smaller polysaccharides or completely into glucose units is relatively difficult compared to the breakdown of other polysaccharides called cellodextrins, because cellulose molecules bind strongly to each other. Processes do exist however for the breakdown of cellulose such as the *Lyocell* process, which uses a combination of heated water and acetone to break down the cellulose filaments.[3]

1.1.2 Nanocrystalline Cellulose (NCC), Fabrication and Applications

Nowadays, much research activity is devoted to new forms of cellulose named nanocrystals, whiskers, nanofibrils, nanofibers and crystallites[15-22]. Three main types of nanocelluloses were identified; microfibrillated cellulose (MFC), nanocrystalline cellulose (NCC) and bacterial nanocellulose (BNC) (Table 1-2)[23], depending on their dimensions, preparation and processing methods as well as cellulosic source. These cellulosic objects possess in common one dimension in the nanometre range and are referred to generally as nanocelluloses.

Nanocelluloses can be isolated from forest, agricultural residues and wood by using different methods, which include chemical, physical or enzymatic processes[18,20,23]. Another way to obtain such cellulosic materials is from glucose by bacteria[24-28]. In a singular way, nanocelluloses can combine cellulose properties with nanoscale materials characteristics due to their large surface area, unique morphology, low density, renewable nature; wide variety of filler available through the world; low energy consumption; high specific properties; modest abrasively during processing; mechanical strength, and biodegradability. In addition, they can be easily (chemically) modified[29-33].

Table 1-2 The family of nanocellulose materials[23].

Type of nanocellulose	microfibrillated cellulose (MFC)	nanocrystalline cellulose (NCC)	bacterial nanocellulose (BNC)
Selected references and synonyms	microfibrillated cellulose, nanofibrils and microfibrils, nanofibrillated cellulose	cellulose nanocrystals, crystallites, whiskers, rodlike cellulose microcrystals	bacterial cellulose, microbial cellulose, biocellulose
Typical sources	wood, sugar beet, potato tuber, hemp, flax	wood, cotton, hemp, flax, wheat straw, mulberry bark, ramie, Avicel, tunicin, cellulose from algae and bacteria	low-molecular-weight sugars and alcohols
Formation and average size	delamination of wood pulp by mechanical pressure before and/or after chemical or enzymatic treatment diameter: 5–60 *nm* length: several micrometres	acid hydrolysis of cellulose from many sources diameter: 5 – 70 *nm* length: 100 – 250 *nm* (from plant celluloses); 100 *nm* to several micrometers (from celluloses of tunicates, algae, bacteria)	bacterial synthesis diameter : 20–100 *nm* ; different types of nanofiber networks

In this work we used nanocrystalline celluloses (NCCs) (chapter 3), which are also known as whiskers and consist of rodlike cellulose crystals with widths of 5 - 70 *nm* and lengths between 100 *nm* to several micrometers (Table 1-2).

Cellulose nano/micro-crystal suspensions were firstly reported at the end of 1940s by *Rånby*.[34] NCCs were generated by the liberation of crystalline regions of the semicrystalline cellulosic fibers by hydrolysis with mineral acids[35]. This chemical process starts with the removal of polysaccharides bound at the fibril surface and is followed by the cleavage and destruction of the more readily accessible amorphous regions to liberate rodlike crystalline cellulose sections[36]. When the appropriate level of glucose-chain depolymerization has been reached, the acidic mixture is diluted, and the residual acids and impurities are completely removed by repeated centrifugation and extensive dialysis[23]. A mechanical process, typically sonication, which disperses the nanocrystals as a uniform stable suspension, follows the hydrolysis. The structure, properties, and phase-separation behavior of cellulose-nanocrystal suspensions are strongly dependent on the type of mineral acid used and its concentration, the hydrolysis temperature and time, and the intensity of the ultrasonic irradiation[16,37-39]. The type of mineral acid used in the hydrolysis step was described to have a great influence on the surface properties of the nanocrystals. Crystals generated with hydrochloric acid exhibit poor colloidal stability[29,40] while those hydrolyzed with sulfuric acid undergo some surface sulfation and are therefore stabilized by strong electrostatic repulsion between the anionic sulfate ester groups at the surface[34,41]. Owing to their highly repulsive character, NCC suspensions prepared with sulfuric acid

exhibit higher colloidal stabilities. The dimensions of crystals were also found to vary on the extent of the hydrolysis; a longer reaction time produced shorter crystals[42,43]. An example of a film produced after dialysis can be seen in Figure 1-5. The NCCs were produced from micro avicel by sulfuric acid hydrolysis.

The free crystals dimensions and morphology depend upon the degree of cellulose crystallinity. Similar to nanocelluloses, NCCs can be isolated from a wide variety of cellulosic sources, which include plants[29,38,44], microcrystalline cellulose[45], animals[46,47], bacteria[24,28], and algae[22,32,48]. Because of their length and crystallinity Tunicin whiskers have been a preferred source. Nanocrystals of several microns in length can be liberated[46,47], for instance from bacteria[24,28] although it is expensive and not widely available, which limits its use for a large-scale production. Nowadays the preferred sources for NNCs production are wood and cotton, due to their natural abundance, widespread availability, cellulose content and uniformity[49].

Gray[16,50-53] and other authors[54-56] performed initial research on cellulose nanocrystals by using filter paper and related products owing to their availability in the laboratory and purity.

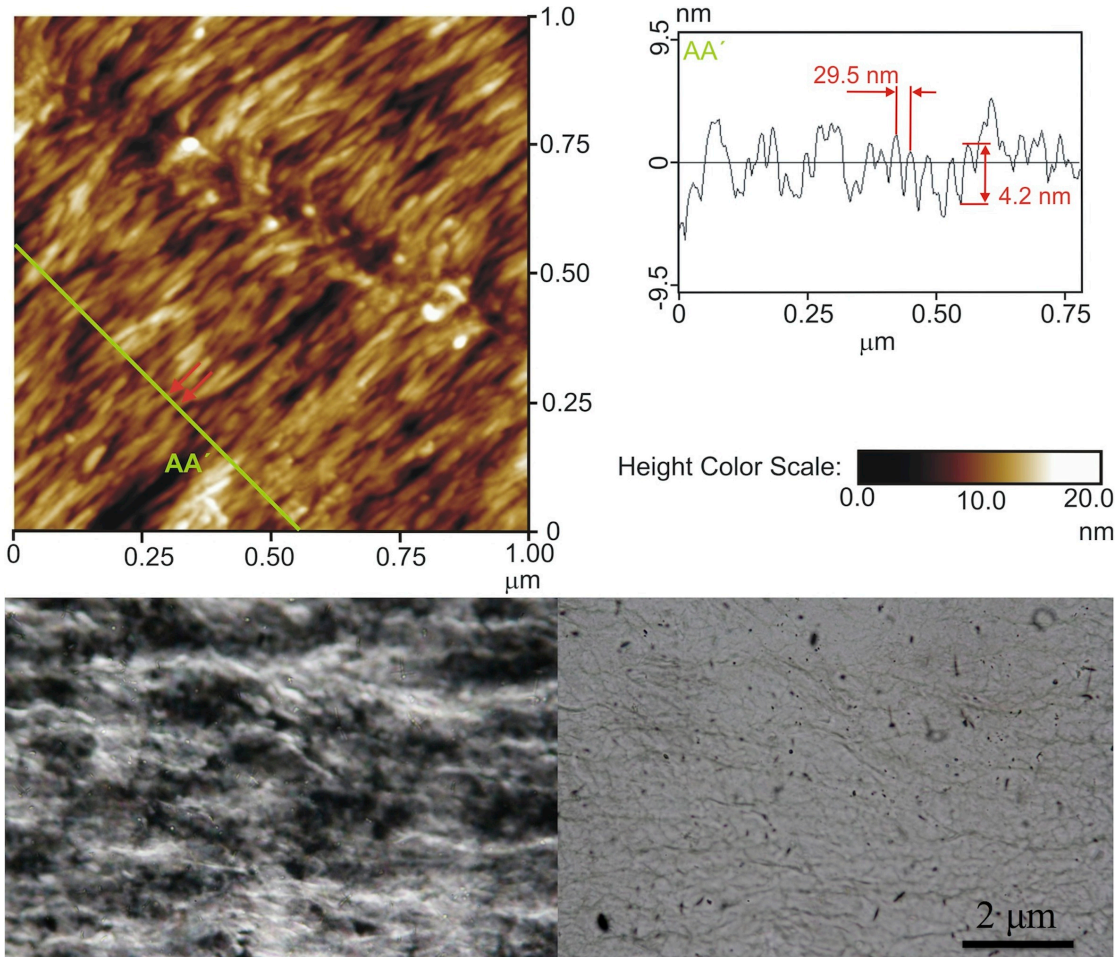

Figure 1-5 **Top:** AFM scan image with the plot of a typical profile, **bottom:** polarized optical Microscopy pictures (left under crossed polarizers and right with parallel polarizers).

These nano-crystals may also show different geometries, depending on their biological source; for example, algal cellulose membrane displays a rectangular structural arrangement, whereas both bacterial and tunicate cellulose chains have a twisted-ribbon geometry[6,57,58].

Transmission electron microscopy (TEM) is a suitable technique to observe dried NCCs suspensions and was used to first reveal the presence of aggregates of needle-shaped particles, while further analyses of these rods with electron diffraction and X-ray scattering demonstrated that they had the same crystalline structure as the original fibers.[59,60]

NCC has attracted a great deal of interest in the nano-composites field due to their appealing intrinsic properties.

NCCs can be used as filler into amorphous polymer matrices. The use of small axial ratios fibers with a theoretical elastic modulus of 138 *GPa* [61], similar to that of steel, and a large surface area of several hundreds of square meters per gram[32] was found an interesting option for composite materials preparation. *Favier*[46] showed, for the first time, that a significant increase of the modulus could be achieved for latex rubbery matrices if NCCs were incorporated. Thereafter many other composite matrices were investigated including synthetic[19,62-64] and natural polymers[32,65-69] as well as elastomers[70-73]. The mechanical performance of polymer-NCC composite materials was the main goal sought by the previous studies.

In a more recently work *Capadona et al.*[74] described a very interesting system of NCC particles dispersed in polymer matrix, which can mimic the sea cucumbers mechanical responsive behavior. In their system, when the whiskers are well dispersed into the solvent, the hydrogen bonds between the NCC are destroyed by forming the hydrogen bonds between whiskers and solvent molecules, leading to a lower elastic modulus state called "switched off" state. By evaporating the solvent, the bonds between cellulose-whiskers are rebuilt, which leads to the high modulus state called "switched on" state. By the competition of these two process they try to mimic the sea cucumbers' ability to rapidly and reversibly alter the stiffness. This architecture and strong interactions among the whiskers maximize stress transfer and therewith the overall elastic modulus of the nano-composite. They demonstrated even larger modulus changes (4200 to 1.6 *MPa*) upon exposure to emulated physiological conditions

Wu et al. [75] prepared PMMA composites by solution casting with the reinforcement of NCC. They demonstrated a marked increase in storage modulus from 1.5 *GPa* for pure PMMA to 5 *GPa* for the composite sheet containing 10 *wt %* NCC at 35 °*C* due to the high modulus of cellulose crystals.

1.1.3 Cellulose Derivatives

Cellulose is insoluble in most organic solvents due to its supramolecular structure. This fact implies that the great majority of cellulose derivatives available in the market are fabricated through chemical heterogeneous reactions[76].

Cellulose combines carbohydrate and polymer chemistry, which affect cellulose reactions and properties. The intermolecular interactions, cross-linking reactions, degree of polymerization, distribution of functional groups on the repeating units along polymer chains are some crucial parameters that determine cellulose chemistry and handling.

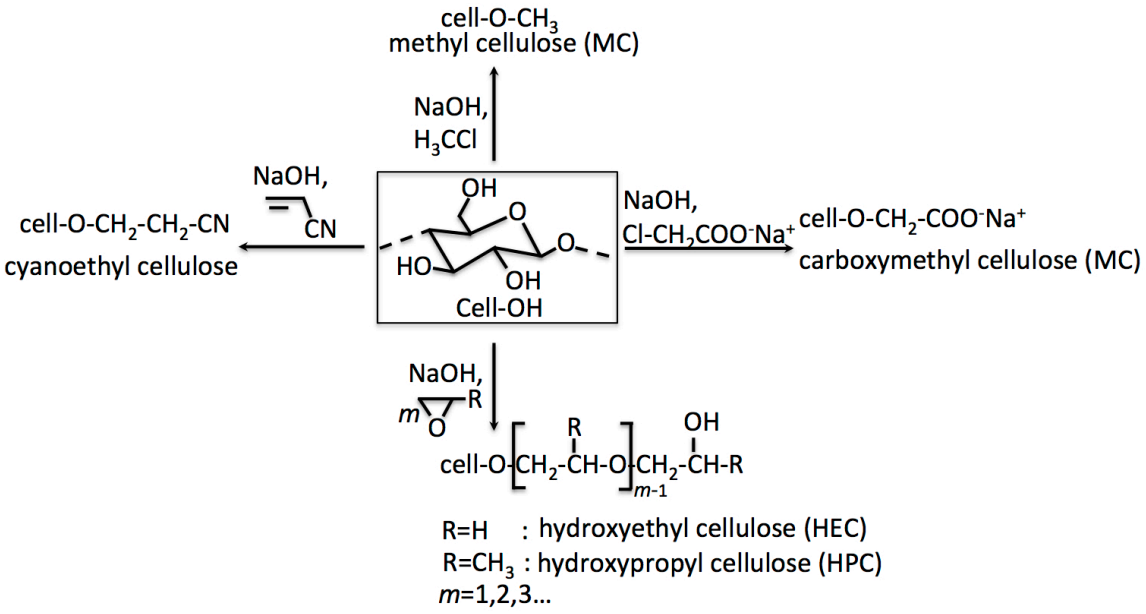

Figure 1-6 Examples of commercial cellulose ethers[25].

Cellulose is a polyfunctional polymer and cellulose derivatives can be obtained by chemical reaction of the three hydroxyl groups available in each repeating cellulose unit. The determination of the degree of substitution along the chain as well as the effect of syntheses procedure on the degree of polymerization is not simple. In fact, several factors like reagents, oxygen, mechanical and thermal loads can disturb the stability of the chain-forming acetal groups. Cellulose derivatives degree of substitution is highly affected by the difference in reactivity between the primary accessible hydroxyl group at C6 and the secondary acidic and close to the acetal function group at C2. The difference in reactivity between C6 and C2 can be exploited for selective reactions of cellulose, but it is limited by the hydrogen bond networks[25]. For heterogeneous reactions, the accessibility and reactivity of the hydroxyl groups are limited by hydrogen bond-breaking activation steps and by interaction with the reaction media. Therefore, usual organic chemistry reactions are not straightway applicable to

cellulose substitution[77]. A great amount of preparative work on the laboratory scale has been developed over the past years with cellulose solvent systems in order to break hydrogen bonds and minimize the influence of the supramolecular network[78]. As a consequence, new types of cellulose derivatives have been synthesized and the understanding of reaction mechanisms, reaction control, structure–property relationships (solubility, film formation, stability), and structure analysis has been increased[84]. Until now, it has not been possible to transfer the homogeneous reactions to technical scale, as the control of aprotic dipolar media and salt components are still a problem[25].

The chemical modification of C1, C3 and C6 hydroxyl cellulose groups are most of the times referred in literature as reactions characteristic of alcohols[79,80]. In this sense esterification and etherification are the most frequently mentioned[81].

Acids chlorides, acid anhydrides or acids in the presence of a dehydrating agent can esterify cellulose. Depending on the acids used two types of cellulose esters are found in literature, esters of inorganic acids and esters of organic acids. Cellulose nitrate is an inorganic acid cellulosic ester while an example of cellulose ester of organic acid is cellulose acetate.

Cellulose esters, contrary to cellulose, are soluble in a wide variety of solvents. The degree of substitution can be controlled and a variety of esters can be produced. These cellulose derivatives have a lot of applications for the production of fibers, films, coatings and membranes.

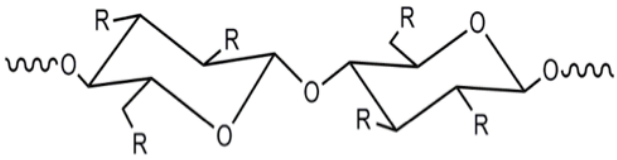

$R\text{-}OCH_2CH(OR')CH_3\ CH_3$ or -OH
(R'- H or $CH_2CH(OH)CH_3$)

Figure 1-7 Molecular structure of HPC[81].

The etherification of cellulose can be accomplished by Williamson ether synthesis and Michael addition. For the first case alkyl halides or alkylene oxides are used while acrylic or related unsaturated compounds are used for the second type of syntheses. Williamson reactions are the most used to synthesize methylcellulose, ethylcellulose and carboxymethylcellulose. Propylene oxide and ethylene oxide are used to obtain hydroxypropylcellulose and hydroxyethylcellulose, respectively, by ring-opening reactions. Cyanoethylcellulose can be produced by Michael addition by reaction of acrylonitrile with alkali cellulose. Cellulose ethers are used as additives in various industries including food, paint, oil recovery, paper, cosmetics, pharmaceuticals, adhesives, printing, agriculture, ceramics, textiles, detergents, building materials and others[82,83].

In chapters 2, 3, and 4 cellulose ether, hydroxypropylcellulose (HPC) was used, so in this chapter we decided to speak in more detail about this kind of cellulose derivatives. Cellulose ethers are a wide range family of cellulose derivatives but hydroxyalkyl ethers of cellulose are an important class in which the most common ethers found in literature and with a wide range of applications are HPC and hydroxyethylcellulose (HEC). These hydroxyalkyl ethers are synthesized by reaction of cellulose with propylene (HPC) and ethylene oxide (EC). The synthesis reactions are schematically represented in Figure 1-6. The epoxide reaction not only occurs with cellulose hydroxyl groups, but also can pursuit at newly formed hydroxyl groups (Figure 1-7), which implies the formation of side chains with different lengths. In order to take this in account the extent of substitution is described by the average degree of substitution ($\overline{DS}$) and average molar substitution ($\overline{MS}$), which is set as the average number of hydroxyalkyl groups per glucose unit. While $\overline{MS}$ values can be greater than three, values of $\overline{DS}$ are always in the range between zero and three. Typical commercial HEC molar substitution values are in between 1.5 and 3.5 and $\overline{DS}$ values in the range of $0.8 < \overline{DS} < 1.8$, while $\overline{MS}$ for HPC varies from 3.5 to 4.5 and DS from 2.2 to 2.8[82,84]. The carbons at which the hydroxyalkylation takes place have different reactivity; the new side chain hydroxyl group carbon has the highest reactivity compared with carbons, C6, C2 and C3 [82,84]. The reactivity of the side chain hydroxyl is higher for HEC, which does not sense the steric hindrance promoted by the methyl groups present in HPC[81].

HPC as well as HEC are non-ionic polymers[78] and the thermoplastic HPC is soluble in cold water and in a great variety of polar organic solvents. Its tendency to generate liquid crystalline phases in the presence of these solvents will be described later in this chapter.

1.2 Cellulose Chiral Nematic Order

The following chapters describe the original work performed with liquid crystalline systems. All the innovative work involves cellulose and/or cholesteric and nematic phases. Due to this we decided to give in this chapter a brief introduction to liquid crystalline nematic and chiral nematic phases as well as cellulosic liquid crystalline materials.

1.2.1 Brief Introduction to Nematic and Chiral Nematic Phases

Solids can be either crystalline or/and amorphous, while common liquids and gases do not present any long range (comparing with molecular dimensions) order and are always considered as amorphous phases[85,86]. In crystalline phases the molecules or atoms are regularly confined into three-dimensional lattices[85]. About 120 years ago, it was found that some materials, which could flow above melting temperature, could still exhibit some birefringence, detected by optical polarized microscopy, characteristic of the crystalline phase. Those phases, observed between the solid and the liquid, were named liquid crystals or mesophases[87,88]. For liquid crystals, the mechanical and symmetry properties are intermediate between the crystals and the liquids[89].

The classification of mesophases is essentially based on their symmetry and three main classes were identified: nematics, smectics and columnar phases[90]. The type of liquid crystals that may be obtained depends on the structure of the constituent molecules or group of molecules. Nematics can be made of elongated or disk-like molecules[91]. A variety of phenomena and transitions amongst liquid crystalline phases can be induced by external parameters and by the nature of the constituent molecules[92].

Liquid crystalline phases can be induced by temperature variation or by changing the concentration of the molecules in appropriate solvents. The first are called thermotropic while the second are lyotropic liquid crystals.

Nematic phase

The word nematic was suggested by *G. Friedel* in 1920[93]. In Greek it means thread, and refers to certain thread-like defects that are usually observed for these kinds of liquid crystals. Figure 1-8 shows a nematic liquid crystal sample sandwiched between two glass plates favoring tangential boundary conditions for the elongated molecules characteristics of these materials. Singularity points (black points) appear connected by black branches, indicating the local direction of the optical axis orientation, tangent to the director (will be discussed later in this chapter). Outside the core, molecular orientation varies slowly. Two defect types with four or two branches can be identified. In this particular photo disclination lines (thin threads) can also be observed. Normally these thin threads evolve and completely disappear in a few minutes. In this case they probably got caught on dust particles or on the surfaces. The threads, normal to the glass plates, are observed along their axis. On turning the polarizers, the extinction branches can rotate and a sign can be associated with each defect, + if the branch rotation follows that of the polarizers and – if they turn the opposite way.

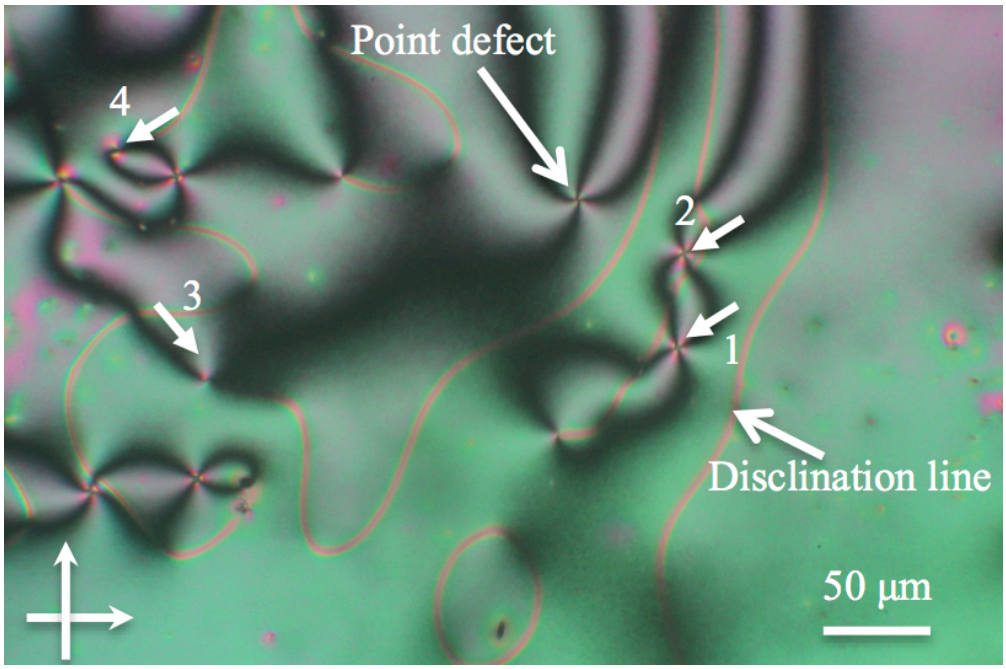

Figure 1-8 Schlieren texture observed between crossed polarizers with a nematic giving tangential boundary conditions on the glass slide. Disclination lines in the bulk can also be observed.

A schematic representation of the arrangement of molecules in the nematic phase made up of rod-like molecules is shown in Figure 1-9. The molecules tend to align on the average along some common axis, which is labeled by a unit vector, or director $\boldsymbol{n}$[90,94]. It is assumed that molecules are free to turn about their axis. This medium is optically uniaxial being the optical axis parallel to the director [94]. Macroscopically there appears to exist complete rotational symmetry around the nematic orientation, reflected by all the macroscopic tensor properties[89]. The nematics have no long-range correlation between the centers of mass of the molecules[95,96] and the axis of uniaxial symmetry has no polarity but the constituent molecules may be polar. Boundary conditions and external fields can impose the orientation of the nematic. Without special measures, the boundary conditions will vary over a substrate. This leads to the variation in the director pattern, and thus to differences in birefringence. A characteristic texture with threads corresponding to discontinuities in a director pattern, varying continuously over distances much larger than the molecular dimensions, can be observed in Figure 1-8.

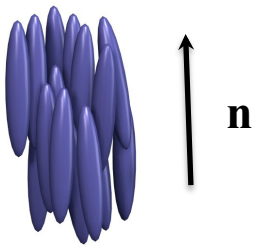

Figure 1-9 Schematic representation of molecules in nematic uniaxial phase built up of rod-like molecules[97].

The liquid like and uniaxial symmetry exhibited by nematics reflect upon nuclear magnetic resonance (NMR) spectrum. Line splittings, absent in conventional isotropic liquids, can be observed as well as narrow spectrum lines due to rapid molecular motions characteristic of liquids. [89,90,98]

Usually different techniques are needed to identify the presence of a liquid crystalline phase, which include polarizing optical microscopy (POM), X-rays, differential scanning calorimetry (DSC) and NMR.

Order parameter

Rigid rods are the simplest type of molecules to give nematic phases. Here we use rod like nematic as an example to describe the order parameter. The axis of one rod will be labeled by a unit vector ***a***. The rod is assumed to have complete cylindrical symmetry about ***a***. The direction of the nematic axis ***n***, the average direction of the alignment of the molecules, will be taken as the *z*-axis of the laboratory frame[86].

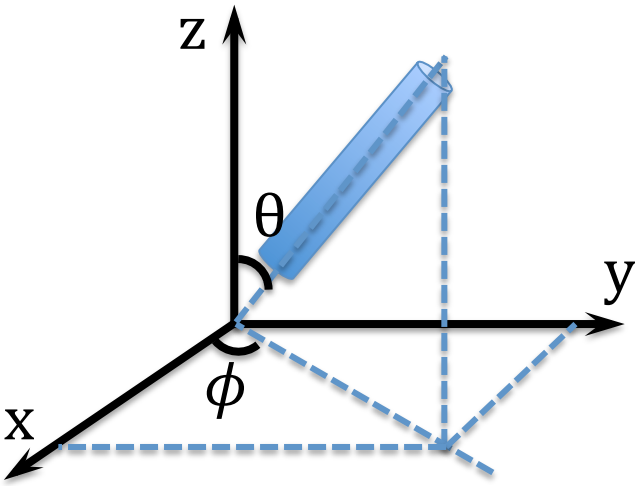

Figure 1-10 The coordinates of a rod used to define the order parameter tensor.

$$a_x = \sin\theta \ \cos\emptyset$$

$$a_y = \sin\theta \ \sin\emptyset$$

$$a_z = \cos\theta$$

$$d\Omega = \sin\theta \ d\theta d\emptyset$$

$$\theta = 0 \sim \pi$$

$$\emptyset = 0 \sim 2\pi$$

The state of alignment of the rods can be described by a distribution function $f(\theta,\emptyset)d\Omega$, $f(\theta,\emptyset)$ is the probability of finding a rod in a small solid angle of $d\Omega$ around the direction of $(\theta,\emptyset)$.

The order parameter is given by:

$$S = \frac{1}{2} < (3\,cos^2\,\theta - 1) > = \int f(\theta)\frac{1}{2}(3\,cos^2\,\theta - 1)d\Omega$$

Equation 1-1[1]

Based on Landau´s general description of phase transition, *de Gennes* developed the phenomenological model of the NI phase transitions, which is called Landau-de Gennes (LDG) theory[99,100]. The LDG theory has the ability to capture the most relevant aspects of the phase transitions[99,101-103]. The model was constructed independent of the detailed nature of the interactions and the molecular structures. It is well described in literature[99,101-103] and here we will speak briefly about Landau-de Gennes free energy.

Landau theory describes a phenomenological depiction of the phase transition, which involves a change of the medium symmetry. Generally, the more symmetric (less ordered) phase corresponds to higher temperature and the less symmetric (high ordered) to lower temperature. The difference in the symmetry between the two phases can be represented by the order parameter. The mathematical description of the theory is based on the idea that the thermodynamic quantities that describe these phases can be obtained by expanding the thermodynamic potential in powers of the order parameter [100].

The nematic state is described by the symmetric tensor order parameter Q with zero trace[99]. Since the thermodynamic potential is a scalar, the expansion can only contains terms that are invariant combinations of the elements $Q_{\alpha\beta} = 0$ of the order parameter. In general the free energy F can be expanded as following[90,98]:

$$F = F_0 + \frac{1}{2}ATr(Q^2) + \frac{1}{3}BTr(Q^3) + \frac{1}{4}CTr(Q^4) + \frac{1}{5}D[Tr(Q^2)\times Tr(Q^3)] + \frac{1}{6}E[Tr(Q^2)]^3$$

Equation 1-2

[1] For instance, if $f(\theta)$ strongly peaked around the angle $\theta = 0\ or\ \pi$, so $\cos\theta = \pm 1$ and *S*=1. If $\theta = \frac{\pi}{2}$ we will get *S*=-0.5. If it is isotropic phase: So $f(\theta)$ will be constant in the whole space, $\int f\,(\theta)d\Omega = 1$, $f(\theta)\int d\Omega = 1$, $f(\theta)\int \sin\theta\ d\theta d\emptyset = 1$, $f(\theta) = \frac{1}{4\pi}$, $< cos^2\theta > = \int cos^2\theta\, f(\theta)\sin\theta\, d\theta d\emptyset = \frac{1}{4\pi}\int_0^\pi cos^2\theta \sin\theta\, d\theta \int_0^\pi d\emptyset = \frac{1}{3}$, so, $S = \frac{1}{2} < (3\,cos^2\,\theta - 1) > = 0$

Where the F_0 is the free energy of the isotropic phase. The coefficients of *A, B, C*, … are functions of Pressure (*P*) and Temperature (*T*). The equilibrium state can be obtained by minimizing *F* with respect to *Q* for the fixed *P* and *T*.

Deformation of LCs

In the absence of external constraints $\nabla \boldsymbol{n} = 0$. If $a|\nabla \boldsymbol{n}| \ll 1$, where *a* is a typical molecular distance, and assuming the temperature and pressure fixed (the local order parameter *S* constant) the free energy *f*, associated with the elastic distortion, can be expanded in a power series of successive spatial derivatives of $\boldsymbol{n}$[95].

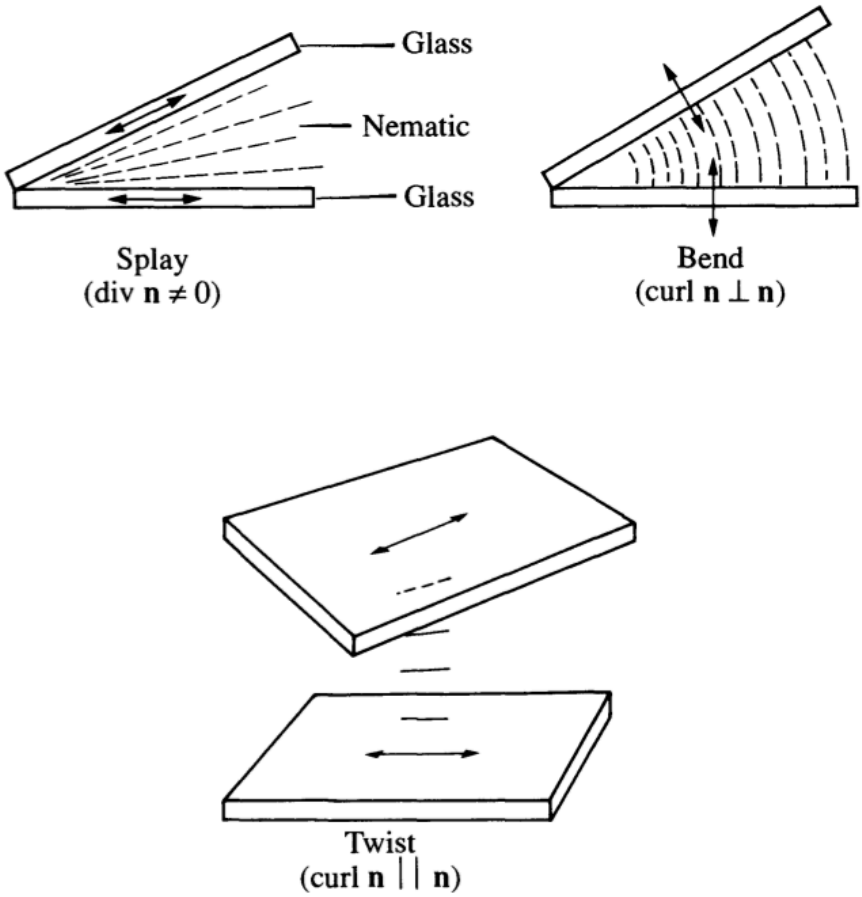

Figure 1-11 Three types of deformation occurring in nematics. The figure shows how each type may be obtained by suitable glass walls treatment (strong surface anchoring conditions)[98,104].

The simplified expression for the distortion free energy, f_d, which can be used in most practical conditions where the surface forces are strong enough to impose a well-defined direction to $\boldsymbol{n}$ at the surface (strong anchoring), is the following:

$$F_d = \frac{1}{2}K_1(div\ \boldsymbol{n})^2 + \frac{1}{2}K_2(\boldsymbol{n}\cdot curl\ \boldsymbol{n})^2 + \frac{1}{2}K_3(\boldsymbol{n}\times curl\ \boldsymbol{n})^2$$

Equation 1-3

K_x *(x=1, 2, 3…)* are elastic constants, K_1 corresponds to splay, K_2 to twist and K_3 to bend (shown in Figure 1-11).

Equilibrium conditions in the bulk can be obtained by minimization of the distortion energy, with fixed boundary conditions for $\boldsymbol{n}$. The influence of external fields, magnetic and electric fields can be included in the free energy expression. For example, if a magnetic field is applied to an usual nematic where $\chi_a = \chi_{||} - \chi_\perp$ is positive, with $\chi_{||}$ and $\chi_\perp$ the magnetic susceptibilities of the medium, parallel and normal to the director, respectively, the free energy becomes:

$$f = f_d - \frac{1}{2}\chi_a(\boldsymbol{n}.\boldsymbol{H})^2$$

Equation 1-4

The distortions of the nematic $\boldsymbol{n}(\boldsymbol{r})$ can be abrupt and a thread-like texture, similar to Figure 1-8 is common observed for nematic samples.

Understanding the defects and textures characteristics of liquid crystalline phases is vital for several reasons; normally a given type of liquid crystal structure presents a characteristic texture, for example a nematic liquid crystal usually exhibits a schlieren texture. In some cases a network of defects can stabilize the formation of complex liquid crystalline phases[89,90,105-109] (for example blue phases[110] and Twist Grain Boundary (TGB) phases[111]). Without the stabilizing defects effect these unusual mesophase structures probably would not exist[90]. Another important implication of the defect formation is their impact on devices fabrication[112]. The defects, discontinuities, inhomogeneties in liquid crystal layers can drastically affect the optics, contrast and performance of the display[113]. Topological defects may also play a significant role in case of defect mediated phase transitions. [90] Several types of nematic planar wedge disclinations were identified and studied. By simple observation of a nematic texture, under cross polarizers, the determination of the spatial variation of the director around point singularities defects can be determined[89,105-107,109]. For example, in Figure 1-8, the distribution of the director around 1, 2, 3 and 4 point singularities are given in Figure 1-12.

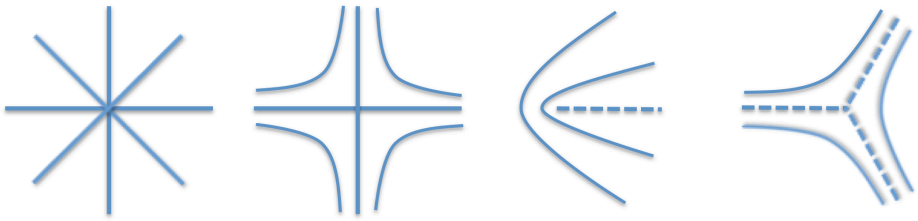

m = +1 m = -1 m = +1/2 m = -1/2

Figure 1-12 Geometrical arrangement of the molecules at the sample surface around point defects 1, 2, 3 and 4 shown in Figure 1-8.

1.2.1.2 Chiral liquid crystals

Chirality in liquid crystals has been the subject of intense research in recent years, and is directly responsible for their important technological applications [90,92,113]. An object (or molecule), which cannot be transformed into their mirror image, by rotation or translation, is called chiral. The term chiral implies that a molecular structure is asymmetric and handed. The presence of chiral molecules in a liquid crystal can have various consequences.

Historically, the chiral nematic phase is called cholesteric phase because the first thermotropic liquid crystalline materials exhibiting this phase were cholesterol derivatives[93]. However, today many different types of chiral materials are available that generate the chiral nematic phase and these have no resemblance to the cholesterol derivatives. Locally, the phase structure of a chiral nematic is very similar to a nematic material, *i. e.,* the centers of gravity have no long-range order and the molecular orientation shows a preferred axis indicated by a director ***n***. However, the asymmetry of the constituent molecules causes a small gradual rotation of the director ***n***. This gradual rotation of ***n*** describes a helix which has a specific temperature-dependent pitch $P=2\pi/q_0$. (q_0 is the wave number) The pitch of the helix is defined as the longitudinal distance in which the angle of twist has made one complete *360* ° revolution[90,92,95,114]. Instead of the uniform alignment of the director field occurring in the achiral phases, the chiral phases usually exhibit a helical structure Figure 1-13. If the cholesteric pitch P is comparable to the wavelength of visible light, a well-oriented cholesteric sample between two plates treated in homeotropic anchoring exhibits specular reflections, which are considered as Bragg reflections of the light on the periodic cholesteric structure, the wavelength of the light is $\lambda_o = n_o P$, [95] where n_0 is the ordinary refractive index.

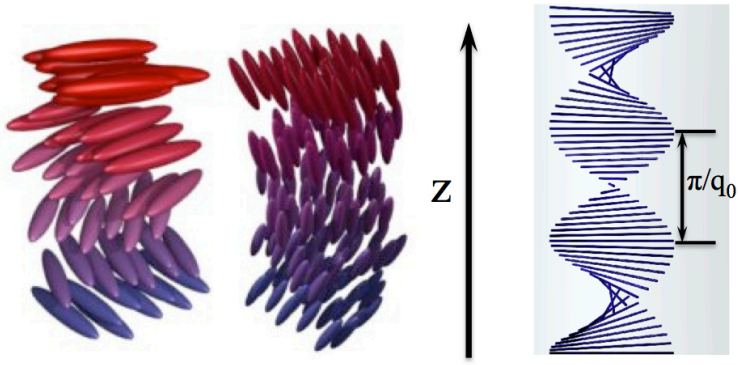

Figure 1-13 The structure of the cholesteric phase. The arrangement of molecules is periodic along z and the spatial period $\frac{\pi}{q_o}$ is equal to one-half of the pitch (P). (The successive planes have been drawn for convenience, but do not have any specific physical meaning.)

In the ideal chiral nematic phase the director $\boldsymbol{n}(\boldsymbol{r})$ varies in space according to the law:

$$n_x = \cos\theta$$

$$n_y = \sin\theta$$

$$n_z = 0$$

$$\theta = q_0 z + constant$$

where the helical axis along z as shown in Figure 1-13.

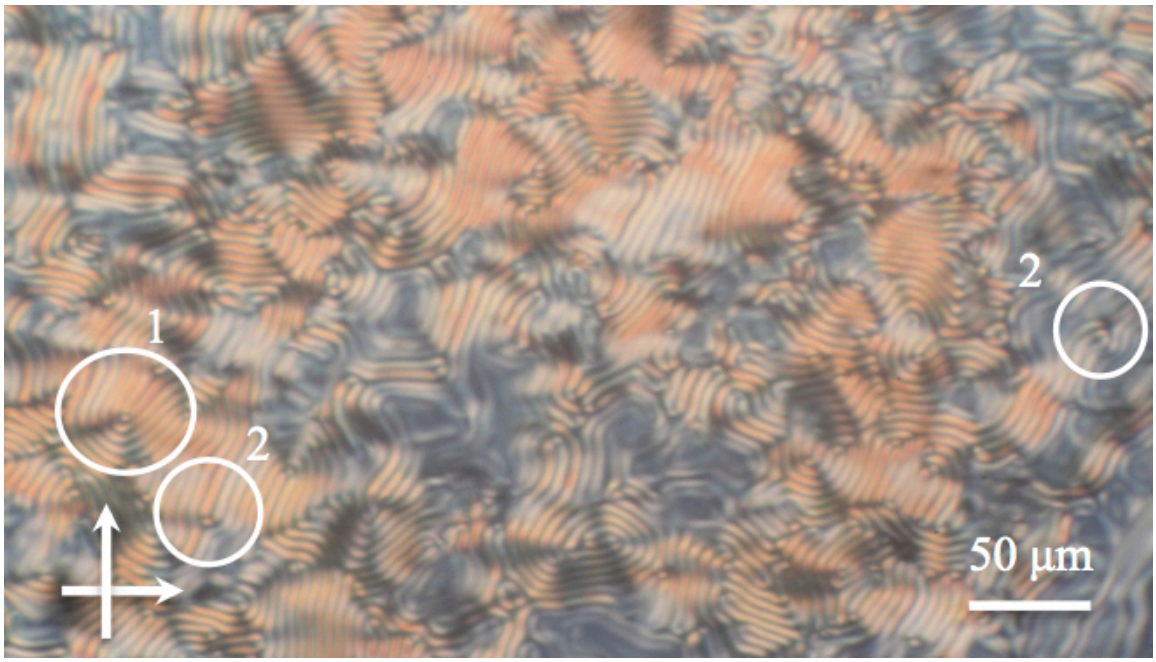

Figure 1-14 Crossed polarizers POM picture of chiral nematic phase (mixture of 5CB and 5CB*). Fan-shaped texture. The elementary patterns *1* and *2* are drawn in Figure 1-15. The value of the pitch for this sample is $P = 8.3\ \mu m$.

When we discuss about the distortion free energy about the chiral nematic phases, we have to add a term to Equation 1-3 and get the new deformation free energy:

$$F_d = \frac{1}{2}K_1(div\ \boldsymbol{n})^2 + \frac{1}{2}K_2(\boldsymbol{n}\cdot curl\ \boldsymbol{n} + \boldsymbol{q_0})^2 + \frac{1}{2}K_3(\boldsymbol{n}\times curl\ \boldsymbol{n})^2$$

Equation 1-5

The cholesteric phases present characteristic textures under the polarizing microscope, in transmission, or in reflection. These textures depend on several parameters, anchoring conditions at the boundaries, sample shape and size, helical pitch and external fields. If the helix axis is normal to the sample surfaces the cholesteric pitch can be determined. In fact the fan-shaped texture shown in Figure 1-14 is a common example of a cholesteric texture in which the cholesteric layers are normal to the glass plates and free to turn in the sample plane. Half of the pitch can be estimated by measuring the length between two dark lines. Another characteristic cholesteric texture, well described by Bouligand[115], is the polygonal field, which is obtained when the cholesteric layers are no longer vertical, but present a tilt with respect to the glass plates. By POM observation this texture is characterized by having an upper and a lower plate focusing, this texture is common in cellulose liquid crystalline materials and will be referred latter in this chapter.

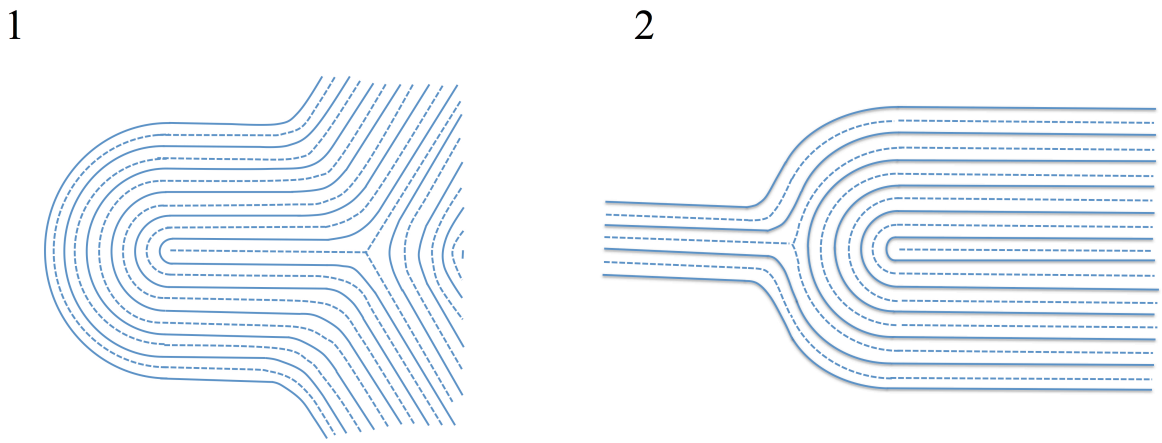

Figure 1-15 Patterns encountered in the fan-shaped texture (see Figure 1-14, *1* and *2*) according to Y. Bouligand´s work[116].

1.2.2 Liquid Crystalline Properties of NCCs

Revol and co-workers discovered that NCCs water suspensions can organize into a chiral nematic phase[117] previously described in this chapter for small molecules, which can be preserved upon air-drying, resulting in iridescent films[118]. The interesting optical and liquid crystalline properties of

NCCs suspensions and colored films were the subject of several studies and reviews[18,20,23,41,118-121].

Low contents of NCCs in water can present a biphasic concentration range in which the isotropic and the chiral nematic phases are in equilibrium as shown in Figure 1-16 [34,36,44]. As the concentration of nano cellulose is further increased, the suspension becomes completely liquid crystalline[36] and textures characteristics of nematic chiral phases develop as the fan-texture, observed under cross polarizers, shown in Figure 1-16 b. The self-induced parallel alignment phenomenon of the NCC that occurs above a critical concentration is attributed to the well-known Gibbs free energy driven self-orientation phenomenon of rod-like species to give nematic order.[20] The ordered phase is a liquid crystal and such behavior was first reported by *Ranby*.[36]

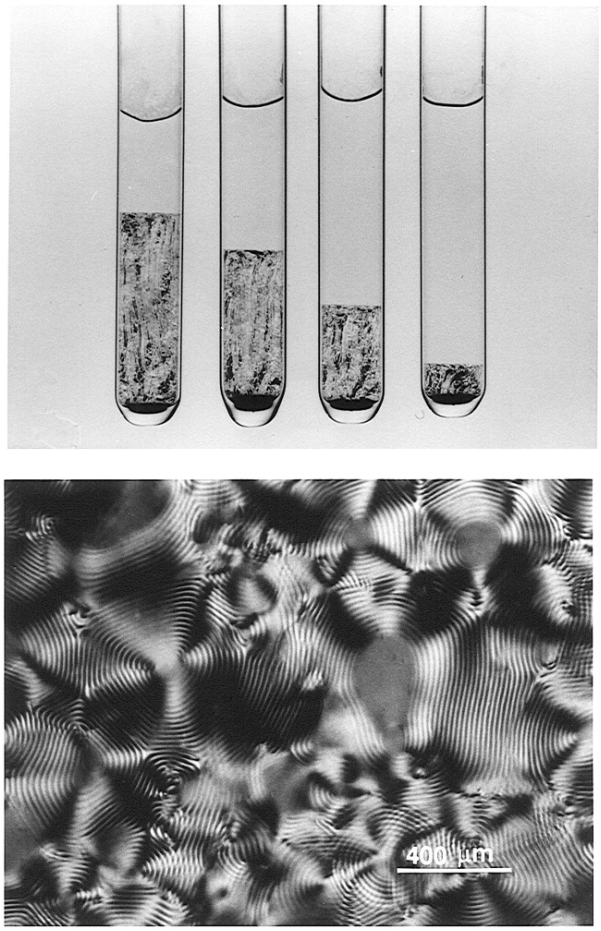

Figure 1-16 **a** (top) Phase separation of cellulose suspension in pure water at different crystallite concentrations. From left to right, the sample concentrations are 8.78, 7.75, 6.85, and 5.78 *wt %*,respectively. **b** (bottom) Chiral nematic texture of the anisotropic phase of a cellulose suspension. [44]

In fact, *Gray et al.* studied the formation of ordered phases of acid-hydrolyzed cellulose suspensions as a function of cellulose crystallite concentration and added electrolyte (HCl, NaCl, and KCl) concentrations. A chiral nematic phase formed when the suspension concentration was higher than

5.14×10^{-6} nm^{-3} in water.[44] The chiral nematic pitch of the anisotropic phase decreased with increasing NCC concentration and with added electrolyte concentration. Apparently, a decrease in double layer thickness increases the chiral interactions between the crystallites. [44]

Further more *Gray et al.* discovered that NCC rods with the diameters of 17-20 *nm* and the length in the interval of 100-200 *nm* could self assemble and generate solid films with symmetric focal conic textures observed by polarized-light (Figure 1-17) in which the line defects form a pair of perpendicular, antiparallel, and confocal parabolas.[122] The film´s surface was analyzed by atomic force microscopy and a regular array of large and small elevations were observed as shown in Figure 1-17 and Figure 1-18 along a high degree of rods orientation. The modulation of the films microstructure by computer revealed that many structural layers terminate at the film surface (Figure 1-18).

The alignment of nano cellulose crystals solutions can be achieved by external magnetic and electric fields, which promote the alignment of the phase structure producing regular single domains [41,123].

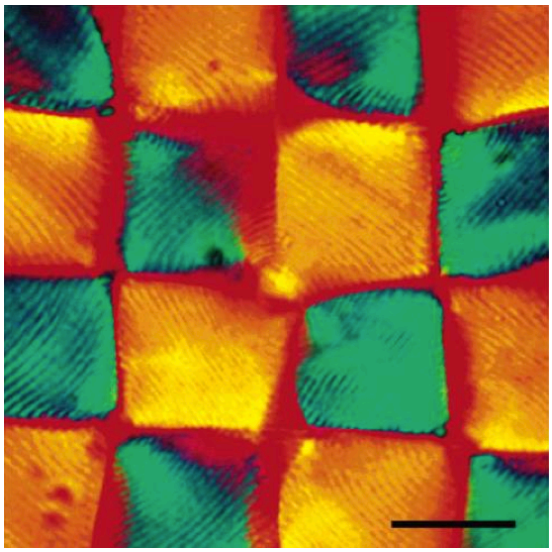

Figure 1-17 Square lattice with crossed polarizers and full-wave retardation plate inserted into the microscope. Scale bar 20 μm. [122]

Another interesting study related to NCCs liquid crystalline characteristics showed that freestanding mesoporous silica films with long-range chiral nematic ordering may be obtained by using NCCs templates. The chiral nematic organization and high surface area of NCCs can accurately be replicated in the inorganic solid. The helical structure of the mesoporous films results in chiral reflectance that can be tuned across the entire visible spectrum and into the near-infrared. (Figure 1-19) [124]

This work opens new horizons on NCCs applications as colored structural materials.

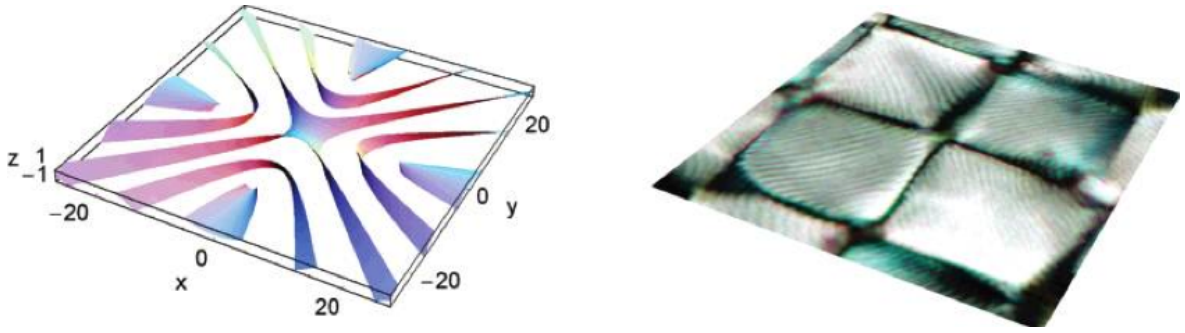

Figure 1-18 Layer tilting in the center of a Parabolic focal conics structure with a focal length of 11 μm, layer spacing 1.375 μm. For clarity, only every fourth layer is shown. The corresponding area of a p-arabolic focal conics is shown in the photomicrograph on the right. [122]

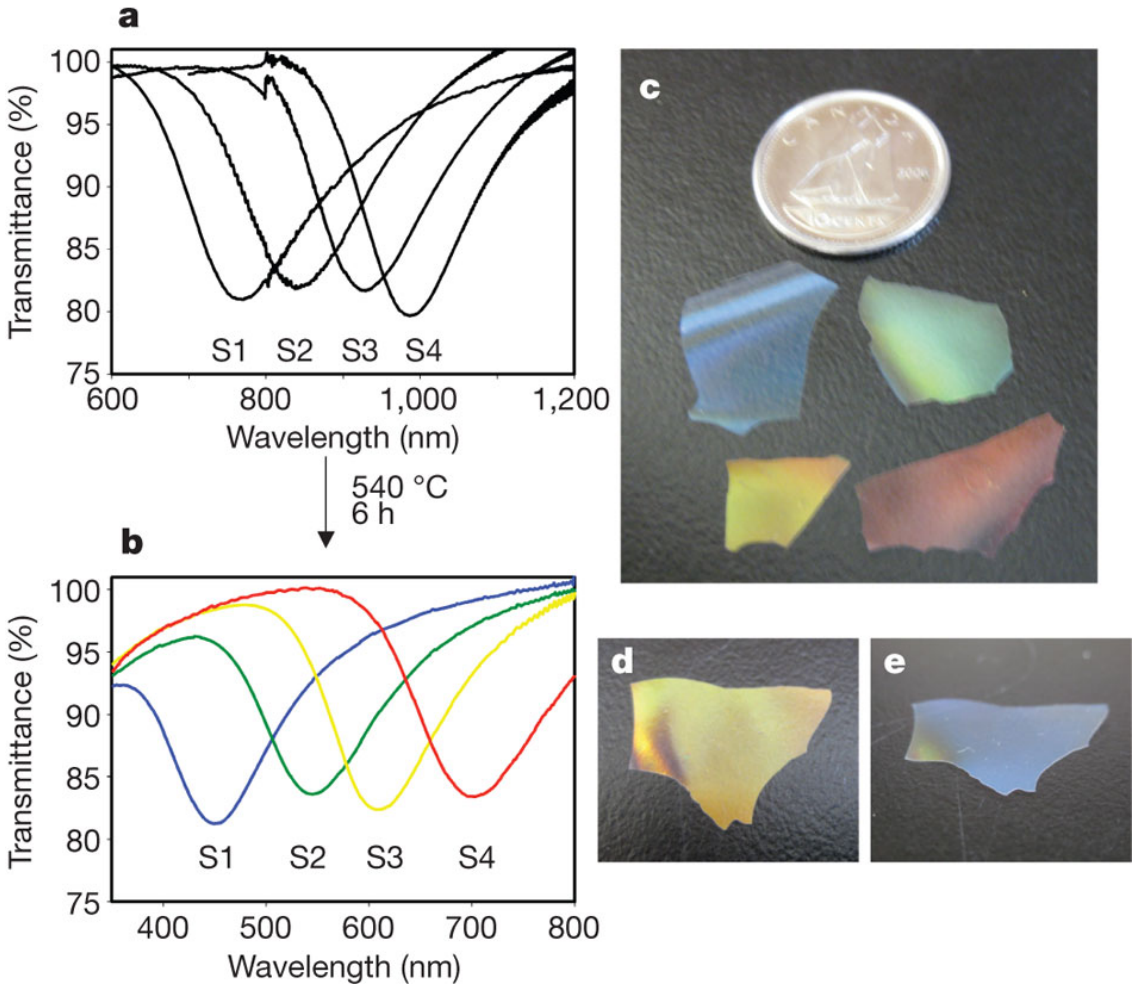

Figure 1-19 **a**, Transmission spectra of four NCC/silica composite films with reflectance peaks in the near-infrared part of the spectrum. The proportion of Tetramethyl orthosilicate: NCC was increased from samples S1 to S4, resulting in a redshift in the reflectance peaks of the films. **b**, Transmission spectra of the mesoporous silica films obtained from the calcination of composite films S1 to S4. The reflectance peaks were all blueshifted by approximately 300 *nm*, resulting in films that reflect light across the entire visible spectrum. **c**, Photograph showing the different colors of mesoporous silica films S1 to S4. The colors in these silica films arise only from the chiral nematic pore structure present in the materials. The dime is included for scale (diameter, 18 *mm*). **d**, Photograph of a yellow mesoporous silica film (S3) taken at normal incidence. **e**, Photograph of the same film taken at oblique incidence appears blue owing to the $sin\theta$ dependence of the reflected wavelength. [124]

1.2.3 Cellulose Liquid Crystalline Networks

Polymer molecules with stiff or semi-rigid backbones are capable of forming lyotropic and thermotropic liquid crystalline phases.[125] For cellulose and cellulose derivatives the backbones are semi-rigid and it is not surprising that many form liquid crystalline phases. The first published report of the formation of a liquid crystalline phase by a cellulose derivative[126] showed that concentrated aqueous solutions of HPC form lyotropic mesophases that display iridescent colors over a specific concentration range. Since this initial report in 1976, many cellulose derivatives have been found to form lyotropic and thermotropic liquid crystalline phases.[125]

The liquid crystalline phases of most cellulose derivatives form chiral nematic structures as a result of the chirality of the cellulose backbone. The semi-flexible nature of cellulose derivatives results in these polymers having a critical concentration for mesophase formation, which is greater than that of rigid rods of the same molecular weight. The critical concentration varies with the nature of the solvent, indicating that the solvent plays a role in determining the stiffness of the cellulose backbone[127].

Cellulosic liquid crystals exhibit optical properties analogous to those observed from chiral nematic mesophases of polypeptides and chiral small molecule mesogens. These optical properties have been found to be also sensitive to several factors, such as the nature of the side-groups, the degree of substitution, the molecular weight of the polymer and temperature. The optical properties of HPC mesophases were among the first to be investigated. HPC forms a liquid crystalline cholesteric phase according to its concentration in water. The critical concentration for mesophase separation, at about 40 *wt %* polymer in water and at slightly higher concentration in methanol and ethanol, depends to some extent on factors such as the nature and degree of substitution, the solvent, the temperature and the molar mass of the polymer. The flexibility of the cellulosic chain appears to be the primary factor governing the concentration of polymer that is required for formation of the liquid crystalline phase.[128]

Gray et al.[129] were the first to report that concentrated aqueous solutions of hydroxypropyl cellulose could generate lyotropic mesophases, which displayed a range of iridescent colors. Evidence from light microscopy, optical rotatory dispersion as well as NMR, and X-ray suggested that the mesophase organise in a helicoidal structure, resembling that of cholesteric liquid crystals.[128]

It is well know that HPC-water solutions exhibit a complex phase diagram including, at room temperature, (Figure 1-20) an isotropic phase at HPC concentrations below 40 *wt %* followed by a biphasic region and a cholesteric phase at higher concentrations[130]. The particular aspects of the phase diagram depend upon the temperature, molecular weight, substitution degree and also solvent type. The characteristic polygonal field texture observed for the cholesteric phase, at room temperature, is shown in Figure 1-21 [126,131,132]. HPC and its ether and ester derivatives generally form right-handed chiral nematic mesophases, with a pitch that increases with increasing temperature and decreasing polymer concentration. The pitch and chiral nematic twist sense of mesophases of cellulose

derivatives are strongly influenced by the nature of the side-group substitution and the solvent. It is not known how or why different achiral substituents on the cellulose chain or changes in the solvent can influence the chirality of these tertiary helicoidal structures[126,133].

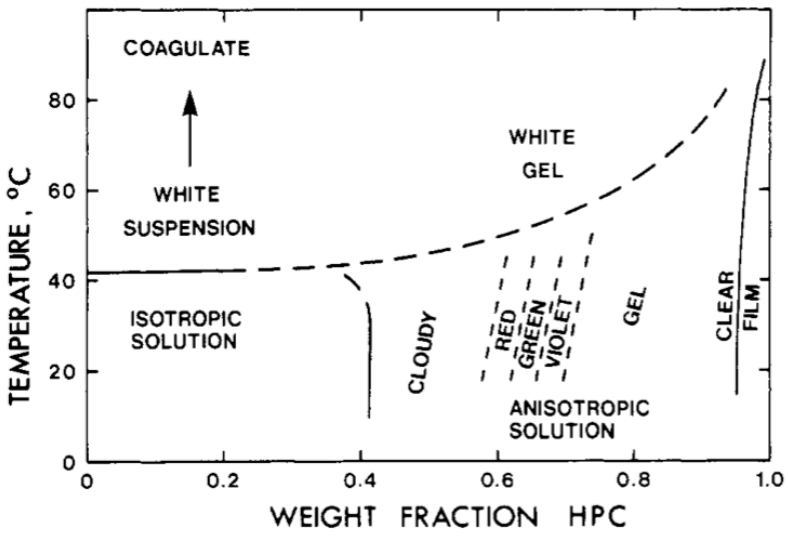

Figure 1-20 Sketch indicating the appearance of the hydroxy-propylcellulose-water system as a function of temperature and concentration. [130]

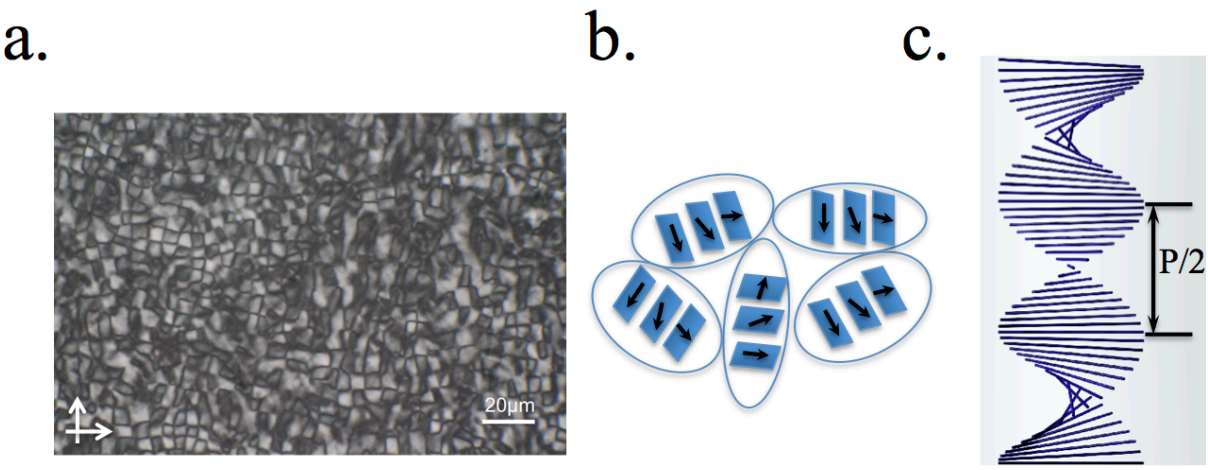

Figure 1-21 **a** POM picture of the cholesteric state solution of HPC in water (50 %w/w). **b**, **c** Director orientation in the cholesteric liquid crystal.

Liquid crystalline polymers (LCPs) exhibited great promise of opening a new era of lightweight, high-strength materials when they were first introduced commercially. Unfortunately, these hopes and predictions have not come to fruition due to difficulties in processing and their complicated physics in solutions and blends. Yet, despite these problems, the demand for LCPs has grown and is predicted to continue growing in the future. In order to optimize the ability of industry to utilize LCPs in

commercial products, a better understanding of the rheology, processing-structure-property relationship, and fundamental physics of LCPs is necessary. All LCPs incorporate an anisotropic element, a mesogen, into their architecture. The alignment of this anisotropic structure results in the unusual ultimate properties and unique physics of LCPs. For commercial products that are manufactured from liquid crystalline polymers, this alignment of the mesogenic structure usually occurs during processing; *i. e.,* shear-induced alignment is responsible for the molecular orientation. Given the importance of this process on the ultimate properties of the final product, there is, surprisingly, a glaring absence in the understanding and theoretical explanation of the interaction of a shear field with a LCP that accounts for the observed responses of a LCP to shear flow. [134] Rheology studies on the HPC-water system have shown that in the liquid crystalline phase three distinct regions of steady shear flow can be observed[135-137] as introduced theoretically by *Onogi* and *Asada*[138] using a domain-based model that accounts for the shear rate dependence of the viscosity by correlating the response of the well-known poly-domain nature of a liquid crystalline polymer in solution to shear flow (as depicted in Figure 1-22, to explain the viscosity dependence of a LCP solution on shear rate.[134,138]). Different domains have significantly different local system configurations resulting from the material response to the imposed shear stress. The viscosity dependence is explained with respect to the response of the domain structure to the shear flow. In regime *I* the domain structure is not altered, but the domains flow over each other, resulting in a shear-thinning regime. Regime *II* describes the system as the domains are starting to break up due to the shear flow. Simultaneously, domains are flowing within an incipient monodomain (regime *III* begins where the domains break up and create a single monodomain).[134]

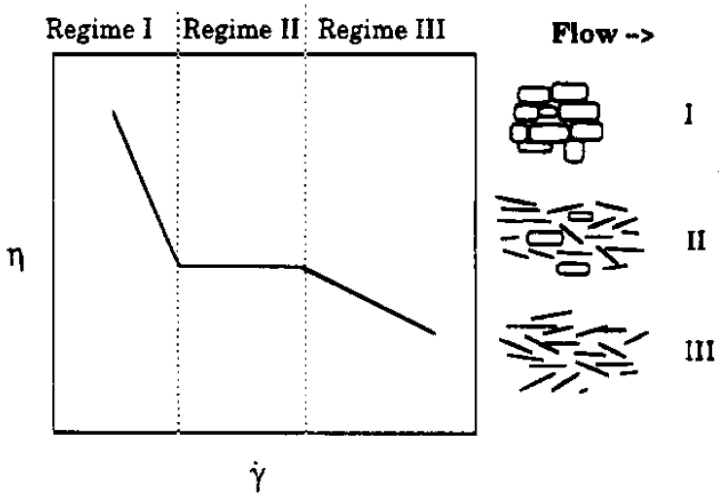

Figure 1-22 Diagram depicting three regimes of a LCP under shear flow as defined by Onogi and Asada. [134,138]

Larson determined the orientational distribution of an LCP in solution under shear flow in three dimensions. By accounting for excluded volume and the flow field, the order of the system can be

determined at varying shear rates. At low shear rates, the shear flow is not flow aligning and the director tumbles under flow. In this regime there is no change in the order of the system with shear rate. As the shear rate increases, the flow dampens the tumbling of the director, but as the director still wants to rotate, a wagging motion ensues. Though the overall order of the system decreases dramatically in this regime, the molecular order of the solution in the flow-vorticity plane is predicted to initially exhibit a barely perceptible decrease and then increase with shear rate in this regime. Finally, at further increased shear rate, the flow becomes shear aligning, with an increase in the order with increased shear rate. [134,139,140]

Charles Han also studied the orientation response of LCPs under shear using neutron scattering.[134] By measuring the scattering patterns of a liquid crystalline polymer solution while subjected to shear flow, the response of the LCP solution to the shear flow, in terms of the orientation of the rodlike molecule, was determined. As the shear rate was increased, the existence of three regimes in the flow of the LCP in solution with respect to its molecular response to shear was found.

Slow regime, In this regime there is an increased average alignment of the LCP in solution with shear rate. This may correlate to an increase in speed of the tumbling of the director with shear rate.

Intermediate regime, In this regime there is a slight change in the average alignment of the LCP with shear rate. This is due to the inhibition of the rotation of the LCP by the shear flow.

Fast regime, The distribution of the alignment of the LCP about the shear direction narrows in this regime. This occurs as the flow field overcomes the local dynamics of the LCP. This manifests itself in the viscosity as shear-thinning behavior.

It was also seen that the response of the LCP to shear flow near the gel threshold exhibits an unusual correlation perpendicular to the shear direction at low shear rates.

HPC is an important mesomorphic polymer model system due to its ready availability and solubility in a wide range of solvents. It was reported[131,141] that changes in temperature and solvent type affect the rheo-optical response of the HPC solutions. Due to the complexity of the HPC aqueous solution structure it is important to study its response to external fields such as shear in order to improve our understanding of the complex bio-system and its behavior in the industry processing.

Hongladarom et al. studied the birefringence and shear stress during and after shear trying to understand the molecular orientation of HPC in LCP.[136] They found that in steady flow, flow birefringence reveals that the molecular orientation increases monotonically with shear rate, but gave two transitions in orientation, one from low to moderate orientation, followed by further increases in orientation at higher rates. The latter increase occur in shear rate ranges characteristic of the transition from tumbling to flow alignment. In flow reversal experiments at low rates, the stress and birefringence transients exhibit damped oscillations that are characteristic of director tumbling, but the transients qualitatively change shape as a function of shear rate. Depending on the shear rate, the

birefringence may exhibit either an initial increase or decrease upon flow reversal. Following flow cessation, molecular orientation decreases to a globally isotropic condition at all rates, accompanied by an increase in dynamic moduli. Although birefringence always shows the final state to be globally isotropic, the final modulus depends strongly on previous shear rate. At high shear rates, the solution relaxes to form a high modulus state, while at low shear rates, a low modulus state results. Linear viscoelastic experiments show only minor differences between the two structures, but when flow is initiated from the high modulus state a pronounced stress overshoot is observed, not present in the case of the low modulus state. They assumed that the decrease in birefringence observed in relaxation of HPC solutions results from a transition from a flow-induced nematic back to a cholesteric. At steady shear rates lower than the inverse of the characteristic relaxation time for molecular orientation, there is little net orientation. This suggests the possibility that region I shear thinning in HPC may be attributed to the persistence of cholestericity at low rates. A necessary condition for formation of the high modulus state following flow cessation appears to be a sufficiently high shear rate to impart some minimum degree of orientation to the solution, or, perhaps, to fully destroy the pre-existing cholesteric phase.

These complex properties in the cellulose and cellulose derivatives liquid crystal state solutions lead to the unique orientational order and properties of the product from these kinds of solutions, such as fibers or films. In the next parts we are going to give a short introduction to the fibers and films from liquid crystalline solutions.

1.2.3.1 Fibers

Firstly, we are going to give a short introduction to nano/micro fibers produced by electrospinning. Their properties, producing methods and application, as well as some aspects related to their production and history will be analyzed.

Ultrathin nano/micro fibers, as one-dimensional nanostructures, have been widely studied due to their unique and properties and interesting applications. The materials dimensions reduction leads to new and somehow unpredictable properties. For example, adsorption property of the surface and also the catalytic activity and selectivity, such as the lotus effect, self-cleaning effect,[142] can be modified due to the large specific surface area, which appears at the nano scale. Nano-scale proteins, viruses and bacterias and their characteristics are particularly relevant for biological systems[150].

Several methods have been developed to produce nano-fibers, such as template [143], self-assembly [144], phase separation[145], melt-blown[146] and electrospinning[147-150]. Electrospinning is the most widely used

technique and also the most simple and versatile way to produce continuous nano-fibers on large scale with a diameter in the nano or micrometer scale.[151]

Several expressions are used to describe the electrospinning technique.[152] Among them, the terms "electrostatic spinning" and "electrospinning" are both frequently used. But usually people use "electrospinning" as the noun and "electrospin" as the verb.[152]

Electrospinning is also known as electrostatic spinning.[152] It´s basic principle has been studied since the seventeenth century when liquid droplets were generated from solutions using high electric potentials.[152] Lord Rayleigh started to investigate the relationship between the surface tension and the charges in 1882. From the beginning of last century the usage of this technique spread. The first electrospray device patent was submitted in 1902.[153] *Hagivaba et al.* generated the artificial silk using the electrospinning method.[152] Although the first patent on electrospinning was published in 1934[153], this technique has not been well established until recent times [154].

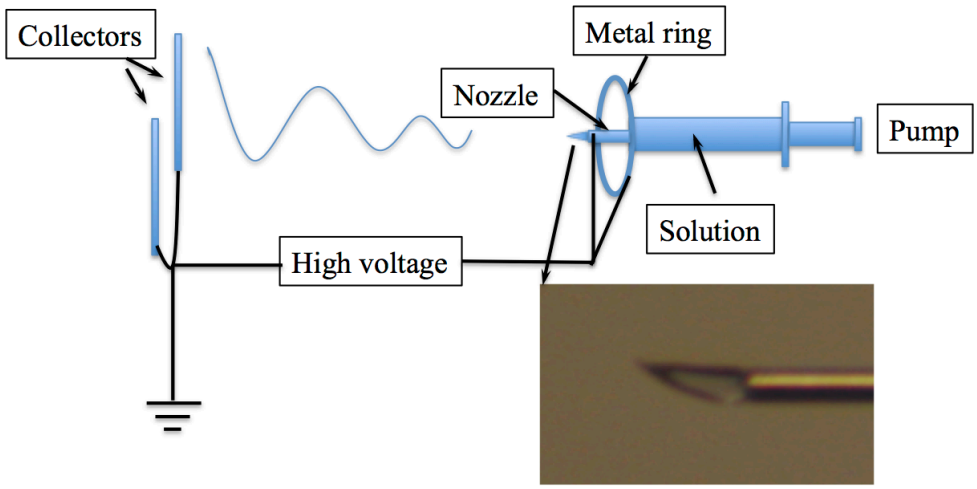

Figure 1-23 Basic structure of the electrospinning apparatus.

Electrospinning technique is unlike the others, in which the formation of the fibers is based on the uniaxial stretching of a viscoelastic jet derived from solution or melt by electric field[151]. The electrospinning apparatus we used is shown in Figure 1-23. The set up consists of a high voltage power supplier, a pump, a solution container, a nozzle, a metal ring and a sample collector. When the solution is charged with high voltage, the electrostatic force draws the fluid into liquid jet and elongates it into fibers. The high voltage power supplier provides the high electric field, which is changeable by the output voltage according to the experimental requirement. It is possible to vary the electric field intensity by modifying, for instance the distance from the nozzle to the target or even the target shape. The pump continuously provides solution to produce fibers. The deposition speed depends on the solution characteristics (solvent, concentration, etc) and also the experimental variable parameters (for instance the electric field intensity). The ring used prevents the fibers to go back to the

pump, because usually the pump is grounded and the distance to the syringe needle is smaller than the distance between the needle and the target.

The diameter and length of the fibers are normally depending on the solution properties, the magnitude of the electric field, environmental factors and the targets used to collect the fibers. In general, fibers get thinner at higher accelerating voltages; however, several other parameters (such as the solution viscosity, needle diameter and the distance to target) also contribute to the fiber shape and dimensions.[155] There are plenty of studies on the control of the electrospun fiber procedures. One of the most important and useful strategies is to use different targets. For example, in order to get aligned fibers two following methods are used widely: collector based on a rotating drum or frame and collector based on a pair of split electrodes.

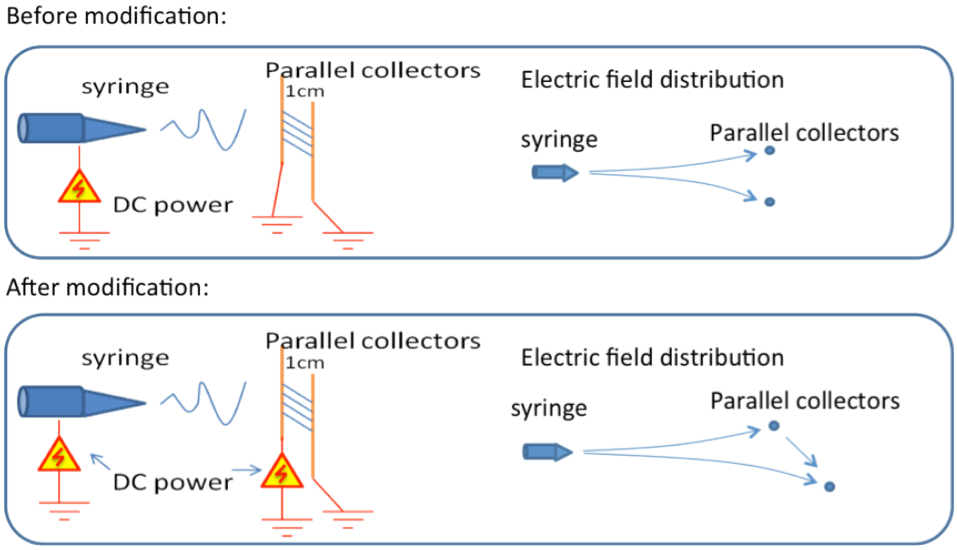

Figure 1-24 Electrospinning apparatus before and after modification.

In our study, we use a modified set up based on the parallel split electrodes by adding a relatively weak electric field applied between the two electrodes, shown in Figure 1-24 and Figure 1-25. Figure 1-24 shows the electrospinning apparatus before and after modification. Normally two parallel grounded metal electrodes are used to collect the fibers. However it was found that the electric field, applied between the electrodes, was not strong enough to align the fibers especially when they were relatively thicker as shown in Figure 1-24 (Before modification). We added another DC high voltage power supplier between the two electrodes with the output voltage of 3 *kV*. In order to easily remove the fibers out of the electrodes, we put a thin but strong enough plastic frame on the two electrodes as shown in Figure 1-25. The dimensional parameters were optimized according to the properties of the fibers and the electrospinning process. As shown in Figure 1-25 *d*, the frame with the dimension of 3 *cm* × 1 *cm* and the inner size of 2 *cm* × 0.8 *cm* were chosen to obtain thick fibers in our study. For

thinner and weaker fibers a strip was left in the middle of the inner hollow of the frame. In Figure 1-25, *b* and *c* represent the frames with deposited fibers.

Electrospun fibers exhibit a range of unique features and properties compared to the fibers produced from other techniques. Electrospun fibers usually have extremely long length. The electrospinning process is a continuous process, and theoretically the fibers can be as long as possible and easily assembled into 3 dimensional nonwoven mats, which can serve, for example, as smart clothes. As referred before, electrospun fibers mats have a high surface-volume ratio. The entanglement of the fibers can also generate a high density of pores. During the electrospinning process, the molecules are highly stretched by the action of the electrical field, achieving a high molecular order, which is locked by solvent evaporation. As a result the conformation, crystalline type and crystalline ability of these fibers are different when compared with fibers obtained by other methods.

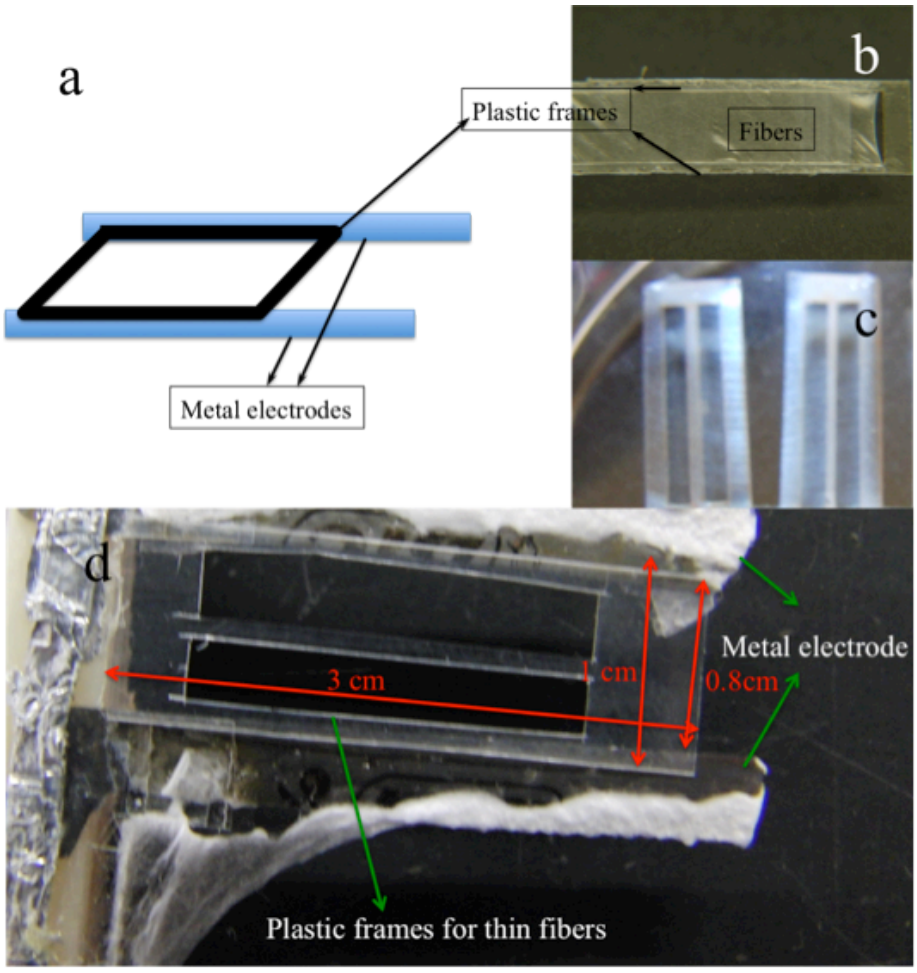

Figure 1-25 Target used to collect fibers. **a**, the scheme of the collectors, a rectangle shape plastic frame was placed on a pair of parallel metal electrode which were connected to a DC high voltage power supply with the output of 3kV, the frame with the dimension of 3 *cm* × 1 *cm* and the inner size of 2 *cm* × 0.8 *cm* as shown in **d**, **b** and **c** are the plastic frames with fibers deposited on them, but *b* is for the thick fibers with a bigger inner space, and *c* for the thin fibers, because thinner fibers are not so strong and easily destroyed so require some kind of support.

Electrospun mats are attractive for a lot of applications. For example, reinforced composites, membranes and smart clothes, biomedical usage, supports for enzymes and catalysts, sensors, electrodes, electronic and optical devices. [151]

Recent studies showed that electrospinning APC fibers can mimic the shapes of plant tendrils on the nano and microscales.[156-158] It is the first observation of a new conformational effect taking place during the electrospinning of cellulose, when spun from solutions in the LC phase: the fibers adopt a characteristic helically twisted form (Figure 1-26). The twisting is on a supramolecular scale, with the pitch measured in micrometers. The helical morphology is similar to what has been seen in amyloid nanofibrils of aggregated peptides and natural cellulose fibrils extracted from algae; however, the length scales and the physical origin of twisting in these systems is completely different. There is also a very interesting and unique report of helical twisting obtained in electrospinning, but the authors achieved it by clever engineering of their electric fields – as opposed to the spontaneous natural twist of the cellulose fibers reported.[158]

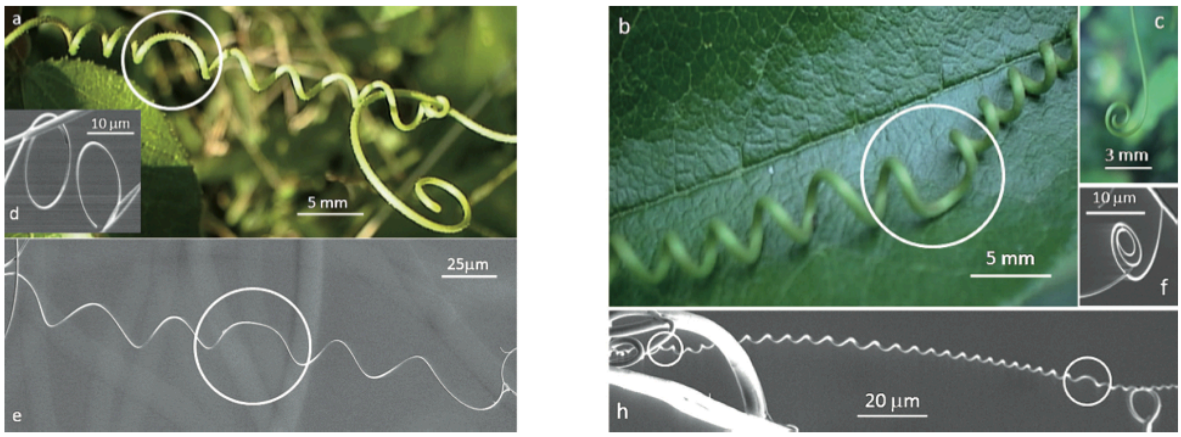

Figure 1-26 Helices and spirals in Passiflora edulis (optical photographs: parts **a**, **b** and **c**) and in our electrospun cellulosic microfibers (SEM images: parts **d**, **e, f** and **h**). Helices form when the tendril or fiber is connected at both ends and tension is released (**a**, **b** e, **h**); spirals when the tendril or fiber is connected at one end only (**c**, **d**, **f**). Helix reversals – "perversions" – are clearly seen in both systems (marked by circles). [158]

The twisting mechanism of these fibers was also studied.[157] Liquid crystalline and isotropic cellulosic precursor solutions of curved and straight fibers were examined using nuclear magnetic resonance imaging (MRI) and polarizing optical microscopy (POM) techniques to determine morphological and structural features contributing to fiber curvature. It was found that the subtle physical mechanisms responsible for the self-winding behavior was the result of the intrinsic curvature of the system. This intrinsic curvature was due to the non-uniform deformation of filaments. The fibers produced from liquid-crystalline solutions showed, a core of disclination forming an off-axis along the filament. It was also highlighted that the helical structures characteristics can be switch by varying the system

temperature, which offers a potential for direct fabrication of biocompatible tunable high-surface area membranes with mechanical adaptability.

1.2.3.2 Films

Hydroxypropylcellulose/water is a cellulose-based system, which is usually referred in literature, due to its biocompatibility, availability and lyotropic liquid crystalline behavior. It was reported that shear casted films can be obtained and used as alignment layers to liquid crystals.[159] Many other studies focused on their topological surface structure and eventual application as photonic materials due to a complex network of "band" defects, which are easily identified by polarizing optical microscopy under cross polarizers.[160] Several studies have been performed in order to correlate the appearance of the bands and the rheological behavior of the solutions, but some fundamental questions have not been answered. X-rays results show that the cholesteric order is destroyed in sheared films and that the polymeric molecules undulate along the shear direction.[161] Atomic force microscopy (AFM) measurements revealed that the topographical features of the sheared films could be turned by modifying the films´ processing conditions.[162] It was demonstrated that samples prepared from liquid crystalline solutions showed two periodic structures, a primary and secondary set of bands. The former consists of bands perpendicular to the shear direction while the latter has the bands slightly tilted from that direction. An out-of-plane angle variation of the sinusoidal molecular orientation was also reported.[162,163] The molecules of the LCPs are easily oriented along the direction of shear. After the cessation of this shear stress beyond some critical value, both thermotropic and lyotropic LCPs develop a characteristic banded texture not found in common flexible polymers. These bands are perpendicular to the shear direction and with a periodic fluctuation of the molecular orientation around the shear direction. An alternating tilt angle of the optic axis of the macromolecule of equal and opposite values, relative to the shear direction, is considered to be the typical character for the reason of the band formation.[164-167]

The periodic oscillation of the orientation of the director has been related to the elastic behavior of liquid crystal systems and attributed to contraction strains of the sheared sample induced by stress relaxation after cessation of flow.[167] The understanding of the mechanism and the factors that are affecting the formation of such textures are unclear and still under study.

A common feature of these mechanisms is that the banded texture is a transient structure in the relaxation of the oriented polymers to release the stored energy as fast as possible. In this sense, the 3D morphology, which can be observed after solvent evaporation, can be attributed to a contraction mechanism. During the shearing process, some elastic energy is stored in the semi-rigid polymer.

After cessation of shear, the oriented polymers begin to relax. However, because the semi-rigid chains are concentrated and highly aligned, their individual thermal relaxation is difficult. In other words they must relax cooperatively and collectively to some degree. As a result the inner stress induces in the whole polymer solution a more or less intense, periodical contraction and the macromolecules are observed to pack in a sinusoidal or zigzag fashion.[168] As evaporation continues, when the concentration is very high, the density of rod-like fragments increases near the free top surface, giving rise to increased orientational order. This in turn causes elongation at the top of the film in the direction parallel to the director, and since the dimensions of the bottom surface in contact with the glass substrate are fixed, the top surface also generates buckles.

Stretching sheared LCPs films along or perpendicular to the shear direction show different material responses associated to the development of different textures. The films were found to be brittle along the shear direction and ductile in the transverse direction. Stretch along the shear direction does not significantly affect the molecular orientation. However, in the transverse direction, profound molecular reorientation occurs on stretching the film, resulting in a fibrillar structure. By stretching along the transverse direction, after the disappearance of the original bands, new bands appear with a much smaller wavelength. [169]

Other type of structural solid colored films can be prepared from cellulose derivatives lyotropic solutions. As mentioned before, the cholesteric phase (chiral nematic phase) of liquid crystals can show selective reflection of light if the pitch of the cholesteric helix coincides with the wavelength of light within the material. Since the reflection conditions vary with the angle between the cholesteric helix and the incident light, different reflection colors can be seen depending on the observation angle. *Zentel et al.* described lyotropic mesophases based on aryl urethanes of cellulose in commercially available mono- or bi-functional derivatives of acrylic and methacrylic acids. To obtain solid films and to conserve the selective reflection the solvents were polymerized photochemically, thus yielding a semi-interpenetrating network of cellulose urethanes in polyacrylates. [170] In these systems many parameters have been changed to control the color of reflection. These parameters are the urethane side groups of the cellulose, the degree of polymerization of the cellulose urethanes, the solvent, the concentration of the solvent, and the temperature. Large solid opalescent films of all colors were prepared that was patterned by crosslinking at different temperatures.

1.2.4 Cellulose Dispersed Liquid Crystals Networks

Polymer-dispersed liquid crystals (PDLC) are widely used for electro-optic applications such as flexible displays, privacy windows or projection displays. Besides these applications, the confinement

of a liquid crystal to small cavities is of fundamental interest. These PDLCs can be switched between a translucent "off" state and a transparent "on" state due to mismatching or matching of the ordinary refractive indices of the polymer and the liquid crystal. In the field-off state, surface anchoring causes a non-uniform director field within the droplets, the film scatters light due to mismatching between the effective refractive index n_{eff} of the liquid crystal and the refractive index n_p of the polymer. In the field-on state, the director is aligned along the field direction, if the dielectric anisotropy of the liquid crystal is positive, and for normal light incidence, the film becomes transparent if the ordinary refractive index n_o of the liquid crystal is equal to n_p.

In comparison with conventional liquid crystal displays, these films are flexible and very easy to prepare, since no polars or surface treatment are required. Because no polarizers are needed the shutters show a high transmittance (may achieve above 80 %). Owing to these advantages, PDLC films are used for large areas, for example, privacy windows and also for display applications. [171] The PDLC film composed of micron size liquid crystal droplets dispersed in a transparent polymer matrix and prepared by one of several techniques including encapsulation, phase separation, either thermally or solvent or polymerization induced, achieves high transparencies in the external field induced ON-state and high opacity in the field absent, light scattering, OFF state.

Godinho et al. studied the electro-optical behavior of a liquid crystal constrained in an elastomer of a cellulose derivative for the first time.[172] The elastomeric film is obtained from an isotropic solution of HPC in acetone, in which a low level of networking is introduced by chemical cross-linking with di-isocyanates. These new composite materials have similar performances to standard PDLCs with the advantages of an improved substrate and a high transmission coefficient in the on state. The mechanical properties of this kind of system as well as the liquid crystal deformation during stretch were also studied.[173]

The search for efficient, scalable and low cost light shutters is an active area of research in the field of Liquid Crystals (LC) in view of, for example, architectural applications. While Liquid Crystals have been so successful in the field of high tech displays for computer and TV screens, the penetration in the field of architecture for large area windows is still under development. PDLCs were discovered by Fergason[174] and Doane[175] and since then many efforts have been done to apply these systems to develop new smart windows,[176] but lately several other applications have been proposed including, displays,[177] microlenses,[178] lasers,[179] and data storage[180].

Recently another polarizer free type of LC optical shutter based on cellulose derivatives with equivalent electro-optical performance and production advantages was proposed.[181] In this device the cellulose derivatives are deposited as nonwoven nano and microfiber mats onto the conductive substrates by electrospinning and the cell is filled up by capillarity with a nematic liquid crystal. In these optical shutters the liquid crystal is embedded with the fibers as a continuous phase, maximizing the liquid crystal/polymer surface contact and thus promoting improved electro-optical properties

Chapter 2 Rheo-NMR Study of Water Based Cellulose Liquid Crystal System

This chapter's work description and discussion was based on the following paper:

Yong Geng, Pedro L. Almeida, João L. Figueirinhas, António G. Feio and Maria H. Godinho. Water Based Cellulose Liquid Crystal System Investigated by Rheo-NMR, *Macromolecules* **2013**, 46 (11), 4296–4302.

2.1 Introduction

NMR (Nuclear Magnetic Resonance) is a powerful technique to access molecular orientational order and local configuration and was used in this study to characterize the rheological behavior of the HPC-water system at a 50 *wt %* concentration. For the used HPC molecular weight, this concentration gives rise, at room temperature, to the cholesteric phase[182] as stated in chapter 1 (1.1.3 and1.2.3). A rheo-NMR study of HPC in aqueous solution has been performed before[183]. It showed that the "equilibrium" state, with low modulus reached after the cessation of a slow shear, is ordered and evolved out of a state with no macroscopic order obtained immediately after cessation of the shear. The high elastic modulus "equilibrium" state, attained after the cessation of a high shear, is much less ordered, although it evolves from a rather well flow-aligned state immediately after cessation of the shear.

In this chapter we make an explicit connection between the DNMR (deuterium NMR) spectra, recorded under and after shear, and the corresponding HPC-water system molecular configurations by modeling the DNMR spectra. Deuterium NMR was used to monitor the shear induced molecular order in the HPC-deuterated water liquid crystalline solution. The liquid crystalline solution was analyzed while submitted to shear in a Taylor–Couette flow cell and during the subsequent relaxation process after shear cessation.

2.2 Experimental

Hydroxypropylcellulose (Aldrich, $\bar{M}_W$=100.000 $gmol^{-1}$, degree of substitution equal to 3.5 determined by ^{1}HNMR) was dried under vacuum for two days before preparing an aqueous solution of 50 *wt* % with deuterium oxide (Euriso-top, 99.97 *%*D). The flasks containing the solution were sealed, kept in the dark to avoid light damage, and stirred every two days. Complete dissolution took place in about two to three weeks. In the NMR experiments, the standard Bruker high power, wide line probe was used at 46.07 *MHz* with a Couette-flow fixture and a saddle coil. The symmetry axis of the Couette cell is parallel to the magnetic field. The mechanical motion in the special insert is derived from a pulse-programmer-controlled stepper motor on top of the magnet. Unless stated otherwise, all NMR data have been taken at a controlled temperature of 303 *K*. The Couette cell consists of an out cylinder with an inner diameter of 9 *mm* and a rotating inner cylinder with a diameter of 8 *mm* (Figure 2-1) both made of PEEK. By previous experience of velocity profile determination in our system, at similar rates, there are no observable wall slip effects. The useful sample height is 20 *mm*. Five different shear rates are used in this study 0.1 s^{-1}, 0.2 s^{-1}, 0.3 s^{-1}, 1 s^{-1} and 3.75 s^{-1}, in which 3.75 s^{-1} is used for pre-shearing (the reason will be stated later). The shearing and measurement process was as follows: first the solution was subjected to a preparation process, it was pre-sheared with the shear rate of

3.75 s^{-1} for 1 *min* to give rise to a stabilized NMR spectra composed of two peaks after which the shear is halted. After a one hour delay a relatively stabilized one peak NMR spectra is obtained. This procedure allows a reproducibly initial state to be attained in every run. Then the measurement processes took place, the shear was restarted with different shear rates, spectra were acquired at regular time intervals and the shear was stopped when the spectra stabilizes. The relaxation process after the cessation of the shear was also monitored. On basis of the established knowledge about the system[184] it is expected that the preparation process gives rise to a polydomain liquid crystalline solution composed of randomly oriented cholesteric domains which were formed when the aligned nematic created by the high shear of 3.75 s^{-1} is left to relax back to the cholesteric equilibrium state.

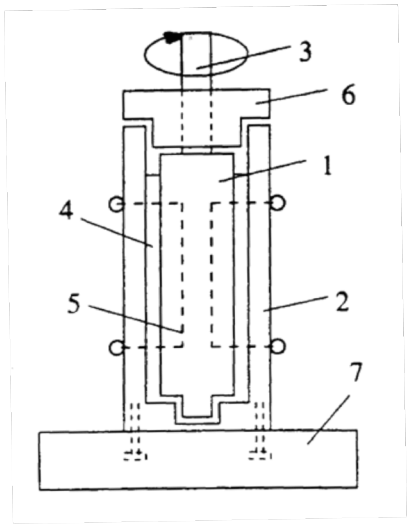

1. Inner cylinder
2. Outer cylinder
3. Motor driven axis
4. Sample
5. rf coil
6. Cover
7. Insert base

Figure 2-1 The Rheo-NMR shearing system.

2.3 Results and discussion

Narrow deuterium spectra were always obtained showing the probe D_2O molecules to be experiencing a high degree of motion leading to a substantial motional averaging of the DO quadrupolar interaction. The spectra also point for a single population of water molecules. Two main types of spectra were obtained, spectra composed of one central peak where no quadrupolar splitting can be resolved indicating a disordered deuterated water environment and spectra compose of two peaks where a quadrupolar splitting is readily observed indicating, by a fast exchange mechanism, the presence of some degree of order in the water environment. We first qualitatively analyze the shear and relaxation processes for each shear rate and later on, we introduce a spectra simulation model to quantify the results.

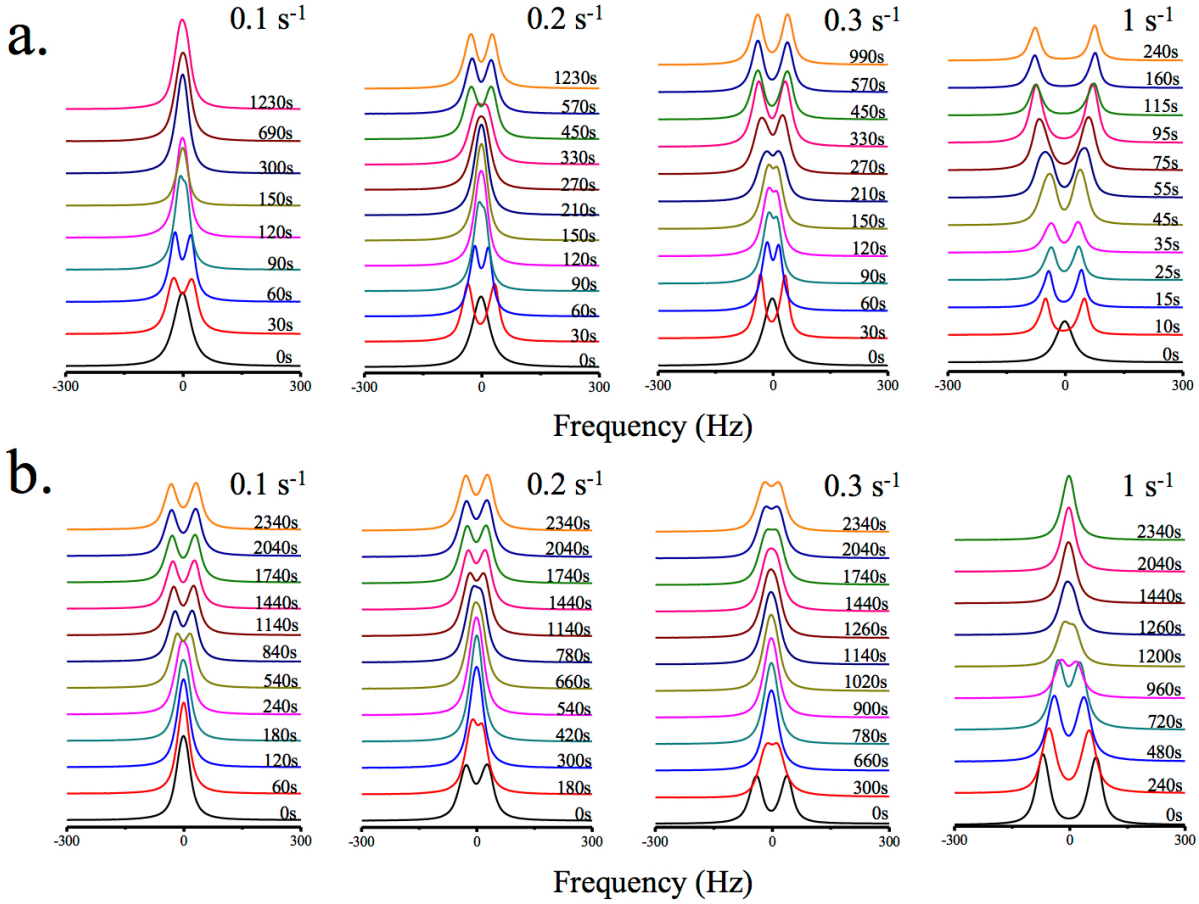

Figure 2-2 NMR spectra evolution of HPC in D_2O. **a** During shearing process with the shear rate of 0.1, 0.2, 0.3 and 1 s^{-1}. **b** After the cessation of shear.

Figure 2-2 gives the NMR spectra at different times at different shear rates during shear (Figure 2-2 *a*) and after shear cessation (Figure 2-2 *b*) For all shear rates analysed the first spectra recorded (at t = 30 *s*) after shear was restarted following the preparation procedure show a line splitting indicating an initial shear-induced increase in order. For the shear rate of 0.1 s^{-1} the peak splitting decreases as time proceeds during shear and vanishes at t = 90 *s* and above. This fact is better seen in Figure 2-3 *a* which shows the peak splitting evolution during shear. This decrease in the system order to a low order state was also described by *K. Hongladarom et al.*[136]. They have checked the birefringence and stress during the shear process (at low shear rates) and also found some order decrease at the beginning period. As proposed before[136] we assigned this low order state to the tumbling regime of LCP dynamics. As already found in previous work[136] and according to our relaxation data, for this shear rate, the cholesteric order inside the domains is not destroyed. The tumbling regime will probably correspond to a periodic reorientation of the cholesteric domains themselves.

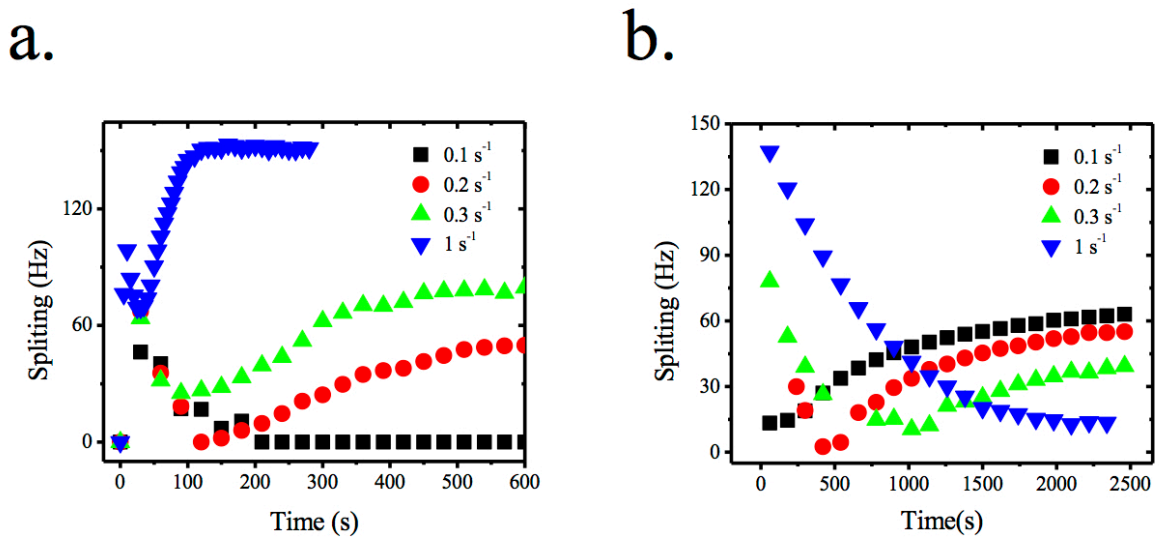

Figure 2-3 Peak splitting evolution with different shear rate: **a.** During shear **b.** After the cessation of shear.

The cholesteric domains present in the liquid crystalline solution after the preparation process are randomly dispersed, (Figure 1-21 *b, c*). In between these domains, water rich regions (WRR) are also disordered giving rise to a one peak spectra. When a weak shear flow is imposed, the domains start to align due to the flow, producing birefringence and imprinting also alignment to the neighboring WRR which gives rise to two peaks in NMR spectra. *Charles C. Han et al.* also stated this phenomenon by neutron scattering studies at low shear rates[134], in which two scattering points along the shear flow were found in the scattering plots. This order increase was also theoretically studied by *Larson et al.*[140] With the persistence of shear, the tumbling regime sets in and the order is again decreased, leading also to less ordered neighboring WRR and promoting the change from the two peaks into one peak in the NMR spectra.

The relaxation process following the shear with 0.1 s^{-1} shear rate (Figure 2-2 *b*) gives rise to spectra that initially show one peak that start to evolve into two peaks at around 500 *s* (0.1 s^{-1}). This recovery of order happens faster and reaches higher values than the order recovery detected in the relaxation associated with higher shear rates. For the higher shear rates that are associated with molecular flow alignment and the suppression of the cholesteric order, the order recovery during relaxation is either absent or happens significantly later. The fast order recovery is then a significant indication that the cholesteric order present before shear within the cholesteric domains persists through the tumbling regime and upon shear cessation starts to build up and to influence the neighboring WRR giving rise to a two peaks spectra. When the shear rate is increased to 0.2 s^{-1}, a behavior similar to the 0.1 s^{-1} shear rate case is found up to t = 200 *s*, then a two peaks spectra starts to develop. This observation points to a scenario where the tumbling regime is accompanied after some time by a flow aligning regime

showing up for t > 200 *s*. The partial flow alignment of the cholesteric domains breaks the average spherical symmetry of the neighboring WRR, giving rise to the observed two peaks spectra. The relaxation process arising after shear cessation shows spectra with a initially decreasing peak splitting (Figure 2-2 *b* and Figure 2-3 *b* with shear rate 0.2 s^{-1}) that vanishes for times in between 180 *s* and 1140 *s* and grows again later on. This behavior can be understood considering that within the first period up to 180 *s* the partially flow aligned cholesteric domains relax to a disordered state that precedes the reorganization and the build up of cholesteric order.

For the shear rate of 0.3 s^{-1}, the behavior observed is similar to the one found for the shear rate of 0.2 s^{-1}, with a different time scale, an increased order during the shearing process and a decreased order at the end of the relaxation period. These correspond respectively to an increased flow alignment and helix distortion of the cholesteric domains during shear and a delayed recovery of the cholesteric order caused by its more intense partial suppression during shear.

The shearing with shear rate of 1 s^{-1}, gives rise to spectra with two peaks at all times during shear. The subsequent relaxation process shows spectra with a decreasing order that does not show any recovery within the time of the measurement. At this shear rate the cholesteric order is suppressed during shear and the LC molecules are aligned by the shear inducing the alignment of the neighbouring WRR. The relaxation process after shear cessation comprehends the destruction of the nematic order, generating spectra with decreasing peak splitting, and later on (outside of our measurement time window) the reformation of the cholesteric domains.

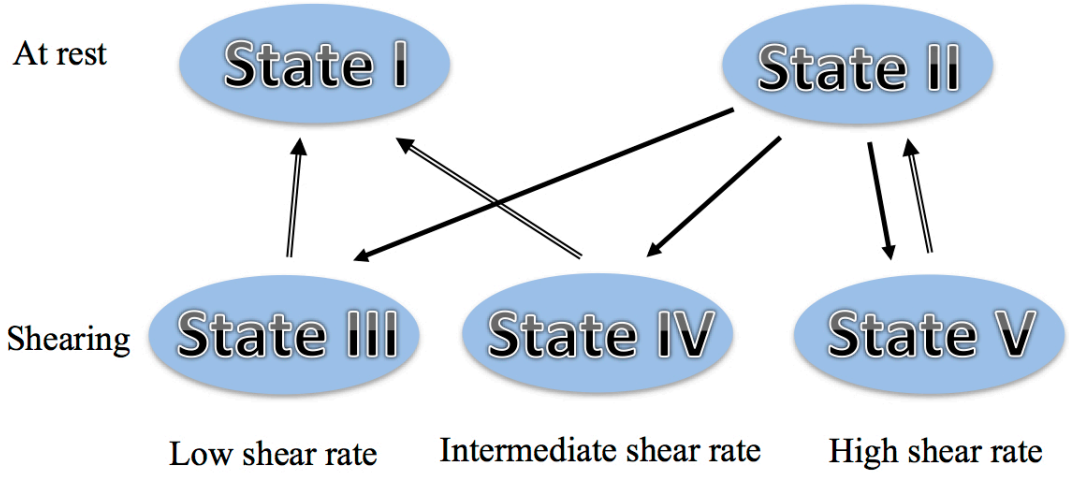

Figure 2-4 Different mesoscopic states reached by the HPC/Water system during shear and relaxation processes.

Figure 2-4 schematically represents the mesoscopic structure of the different states reached by the system during shear and relaxation. This scheme is built around the interpretation of our own DNMR measurements and the established knowledge on the HPC/water system[136]. State *I* corresponds to the partially aligned cholesteric polydomain state reached after relaxation from shearing with low shear

rates. State *II* corresponds to the cholesteric polydomain state reached after relaxation from shearing with high shear rates. State *III* corresponds to the tumbling regime observable for low shear rates, state *IV* corresponds to the partial flow alignment associated with the intermediate shear rates and state V to the flow aligned nematic obtained at high shear rates. The up arrows indicate the relaxation path while the down arrows indicate the path under shear starting from the polydomain cholesteric reached in the preparation state. This picture is in direct correspondence with the three regions of steady shear flow introduced by *Onogi and Asada*[138], at low shear rates state *III* sets in, the intermediate region corresponds to state *IV* and the high shear region corresponds to state *V*.

To gain a deeper insight on the system details leading to the spectra reported we have carried out a simulation of the data obtained with shear rate of 0.3 s^{-1} as it corresponds to the intermediate regime that shares features with the other shearing regimes. The simulation will allow us to follow the system evolution while moving in between states *II* and *IV* during shear and *IV* and *I* during relaxation. A first analysis of the spectra shown in Figure 2-2 *a* and Figure 2-3 *b* shows that they are quite narrow deuterium spectra implying a very significant motional averaging of the DO quadrupolar interaction in each water molecule, to account for this fact we can conceive that WRR present in the frontier of the cholesteric domains possess a disordered core and a polymer induced ordered layer at the surface, with the water molecules sampling the full region volume within the NMR measurement time. More spherical WRR give rise to single line spectra as observed in the least ordered cases while more ellipsoidal WRR with some degree of alignment in between the symmetry axis of different ellipsoids are required to simulate the two line spectra observed experimentally in the most ordered cases. Water rich ellipsoidal regions with small order in between the symmetry axis of different ellipsoids give rise to intermediate spectra with two peaks but a very significant intensity at the central frequency as is observed experimentally in several recorded spectra. Thus the simple model developed to simulate the spectra considers the WRR with an ellipsoidal shape that can change during shear and relaxation.

2.4 Theoretical model

The spectra recorded result from the contributions of all D_2O rich regions present in the sample and is given by:

$$G(\omega) = \int_0^{2\pi}\int_0^{\pi} g(\omega,\theta,\phi)P(\theta,\phi)\sin\theta d\theta d\phi$$

Where $g(\omega, \theta, \phi)$ is the spectra from a WRR with its orientation relative to the external magnetic induction field given by angles θ and ϕ that are defined in Figure 2-5. $P(\theta, \phi)$ is the fraction of WRR with orientations within the solid angle $sin(\theta)d\theta d\phi$ around the orientation defined by (θ, ϕ). $P(\theta, \phi)$ was parameterized as follows:

$$P(\theta,\phi) = C\, e^{-(\theta/\theta_0)^2}$$

Where C is a normalizing constant and θ_0 is a measure of the width of the symmetry axis orientation distribution in θ. An order parameter can be associated with this distribution and it is given by:

$$S \equiv \int_0^{2\pi}\int_0^{\pi} \left(\frac{3}{2}\cos^2\theta - \frac{1}{2}\right) P(\theta,\phi)\sin\theta d\theta d\phi$$

and as θ_0, it gives a measure of how ordered are the symmetry axis of the WRR around the velocity direction at every point. Next we determine $g(\omega,\theta,\phi)$, In this model, the fast motional averaging of DO bonds inside a WRR gives rise to an averaged electric field gradient tensor whose associated DNMR spectra is composed of two lines with a frequency splitting $v(\theta,\phi) = \frac{3}{2}\frac{eQ}{h}\bar{V}_{zz}(\theta,\phi)$ and consequently,

$$g(\omega,\theta,\phi) = \frac{T_2^*}{1+(\omega-\pi v(\theta,\phi))^2 T_2^*} + \frac{T_2^*}{1+(\omega+\pi v(\theta,\phi))^2 T_2^*}$$

Where we have considered a Lorentzian line shape for each of the two lines spectra. The time T_2^* is the decay time of the transverse magnetization related to the frequency width at half-height $\Delta\omega$ of the Lorentzian line by $\Delta\omega = 2/T_2^*$. Considering now the quadrupolar coupling constant for the DO bond $v_Q^{DO} = \frac{eQ}{h}V_{Z'Z'}^{DO}$ which has a value of 250 kHz[185] the splitting $v(\theta, \phi)$ can be written as $v(\theta,\phi) = \frac{3}{2}v_Q^{DO}\bar{V}_{zz}(\theta,\phi)/V_{Z'Z'}^{DO}$.

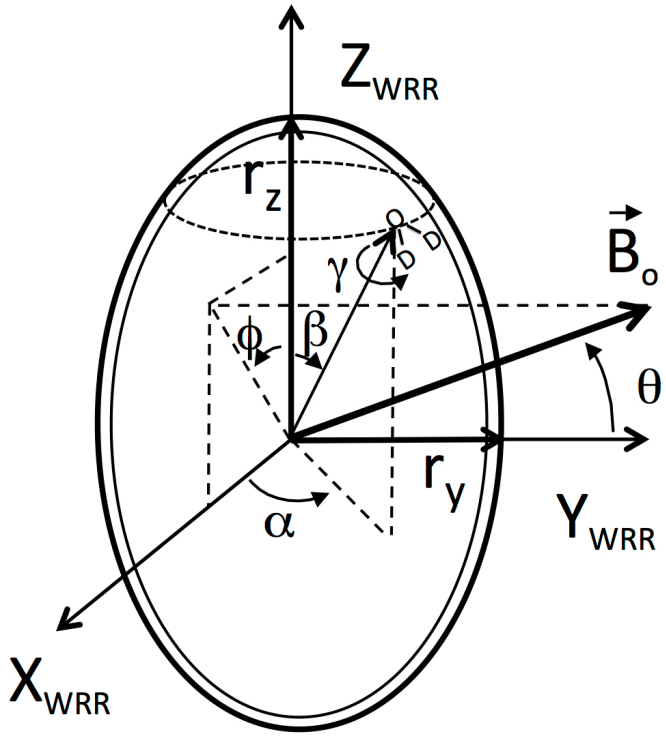

Figure 2-5 Representation of the ellipsoidal water rich regions considered in the simulations with major and minor axis r_z and r_y. The angles θ, ϕ, α, β and γ used in the simulation are also shown. $\overrightarrow{B_0}$ is the external magnetic induction. At the surface of the ellipsoidal region the water molecules interaction with the HPC chains gives rise to an ordered water layer which is also schematically represented.

The averaged electric field gradient tensor *zz* component $\bar{V}_{zz}(\theta,\phi)$ depends upon three model fitting parameters, $\bar{V}_{zz}(\theta,\phi) = \bar{V}_{zz}\left(\theta,\phi; r_y/r_z, S_{D_2O}, l_{D_2O}/r_z\right)$, where r_y/r_z is the ratio between the smallest and largest ellipsoidal radius, S_{D_2O} is the local order imposed on the D_2O molecules at the interface ordered layer by the polymer chains, and l_{D_2O}/r_z is the ratio between the interface ordered layer thickness and the ellipsoidal largest radius.

The determination of the ratio $\bar{V}_{zz}(\theta,\phi)/V_{Z'Z'}^{DO}$ was conducted as follows:

To evaluate the *zz* component of the averaged electric field gradient (EFG) tensor $\bar{V}_{zz}(\theta,\phi)$ of the DO bonds in the magnetic induction z aligned fixed frame we start by determining the averaged EFG tensor in the WRR fixed frame ($X_{WRR}, Y_{WRR}, Z_{WRR}$). For this task we use the Wigner rotation matrices along with the EFG components in the irreducible representation of the rotation group. The irreducible components of the EFG tensor, $\bar{V}_i^{WRR}$ are given by:

$$\bar{V}_i^{WRR} = \frac{1}{V}\int_V \left[\frac{1}{2\pi}\int_0^{2\pi}\sum_{j=-2}^{2} D_{ij}^{2*}(\alpha,\beta_0,\gamma)S(\vec{r})V_j^{D_2O}d\gamma\right]dV$$

or more explicitly,

$$\bar{V}_i^{WRR} = \frac{1}{V}\int_{\alpha=0}^{2\pi}\int_{\beta=0}^{\pi}\int_{r=0}^{r_1}\left[\frac{1}{2\pi}\int_{0}^{2\pi}\sum_{j=-2}^{2} D_{ij}^{2*}(\alpha,\beta_0,\gamma)S(\vec{r})V_j^{D_2O}d\gamma\right]r^2 dr\ \sin(\beta)d\beta\ d\alpha$$

and consequently the averaged EFG tensor component $\bar{V}_{zz}(\theta,\phi)$ is determined as;

$$\bar{V}_{zz}(\theta,\phi) = \frac{2}{\sqrt{6}}\sum_{j=-2}^{2} D_{0j}^{2*}(0,\theta_0,\psi)\ \bar{V}_j^{WRR}$$

We now define the different variables appearing in the last three expressions V is the WRR volume, $V = \frac{4\pi}{3}r_y^2 r_z$. r_1 is the radial distance to the WRR surface, $r_1 = \frac{r_y r_z}{\sqrt{r_y^2\cos(\beta)^2 + r_z^2\sin(\beta)^2}}$. $S(\vec{r})$ is the local water molecules' order and is modelled as:

$S(\vec{r}) = \begin{cases} S_{D_2O} & r \geq r_1 - l_{D_2O} \\ 0 & r < r_1 - l_{D_2O} \end{cases}$ where l_{D2O} is the thickness of the water ordered layer at the WRR surface. β_0 is the angle between Z_{WRR} and the normal to the WRR surface. $V_j^{D_2O}$ are the irreducible components of the DO bonds EFG tensor in a molecular fixed frame depicted below and are given by:

$$V_j^{D_20} = \frac{3}{4}V_{z'z'}^{D_2O}\begin{cases} e^{\mp I\xi} & j=-2 \\ 0 & j=-1 \\ -\frac{\sqrt{6}}{3} & j=0 \\ 0 & j=1 \\ e^{\pm I\xi} & j=2 \end{cases},$$

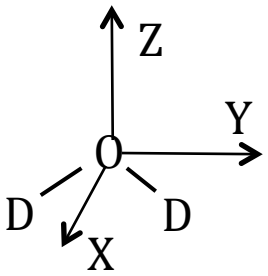

ξ is the bond angle in the D_2O molecule and the +- signs refer to each one of the two DO bonds. The angles θ_0 and ψ appearing in expressions are related to the angles ϕ and θ by the relations, $\cos(\theta) = \sin(\theta_0)\sin(\psi),\ \sin(\theta)\sin(\phi) = -\sin(\theta_0)\cos(\psi),\ \sin(\theta)\cos(\phi) = \cos(\theta_0)$.

In the simulations, estimated fixed values were considered for S_{D_2O} and l_{D_2O}, $S_{D_2O} = 0.7$ and $l_{D_2O} = 1.2\times10^{-3} r_z$.

2.5 Model fits and results

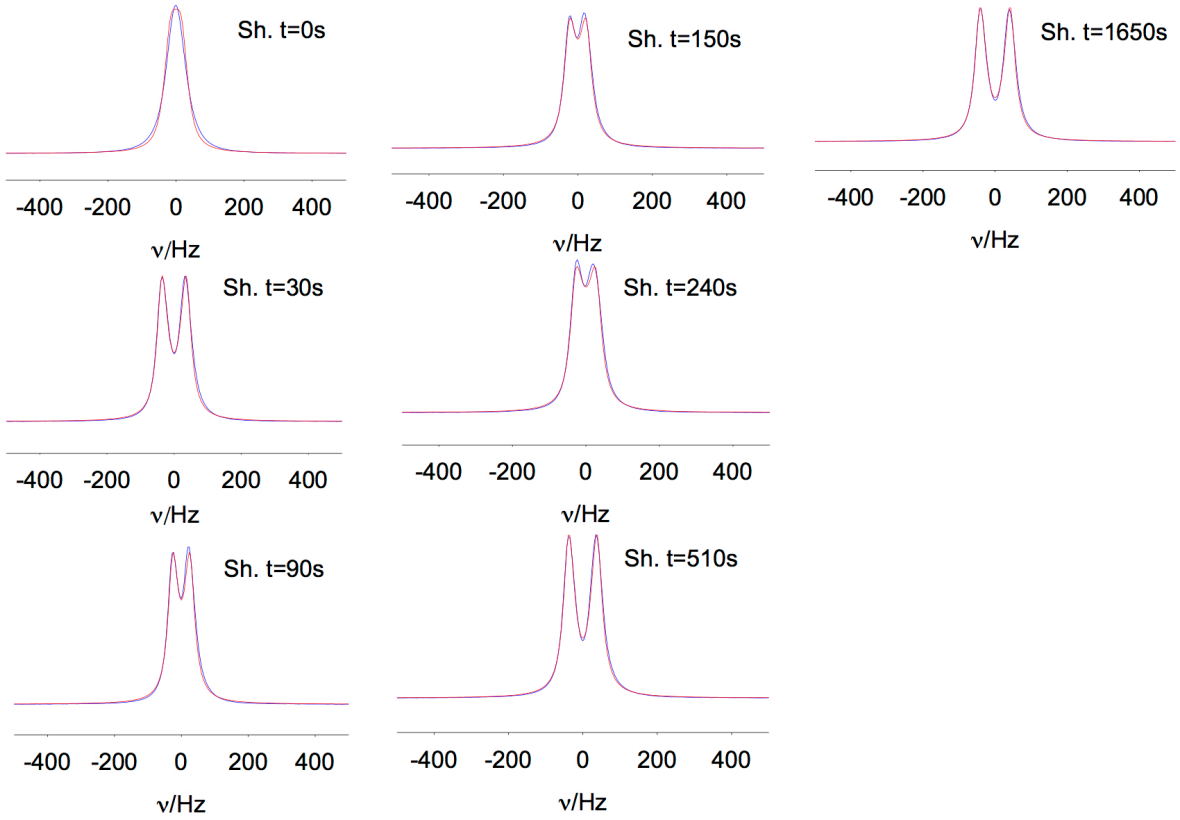

Figure 2-6 Spectra (blue line) and fits (red line) from the model at different times during shear.

Figure 2-6 and Figure 2-7 show the spectra recorded with a shear rate of 0.3 s^{-1} and subsequent relaxation process after shear cessation along with the fits from the model. High quality fits are obtained in both regimes strengthening the model applicability in both cases. *a* and *b* report the r_y/r_z ratio and the symmetry axis order parameter *S* as a function of time during shear and subsequent relaxation process respectively.

Considering the systems evolution in between states *II* and *IV* during shear as described by r_y/r_z and *S* reported in Figure 2-8 *a*, we see that at $t = 0$ *s*, just before shear starts, the WRR are less deformed and highly disordered, immediately after the beginning of shear the deformation increases significantly along with the symmetry axis order, this can be interpreted as a shear induced fast realignment of the cholesteric domains, followed by a slower process of internal structure change. During this slower process the WRR initially become more spherical and less ordered but later on as the internal structure of the cholesteric domain approach state *IV*, they become more asymmetric and more ordered.

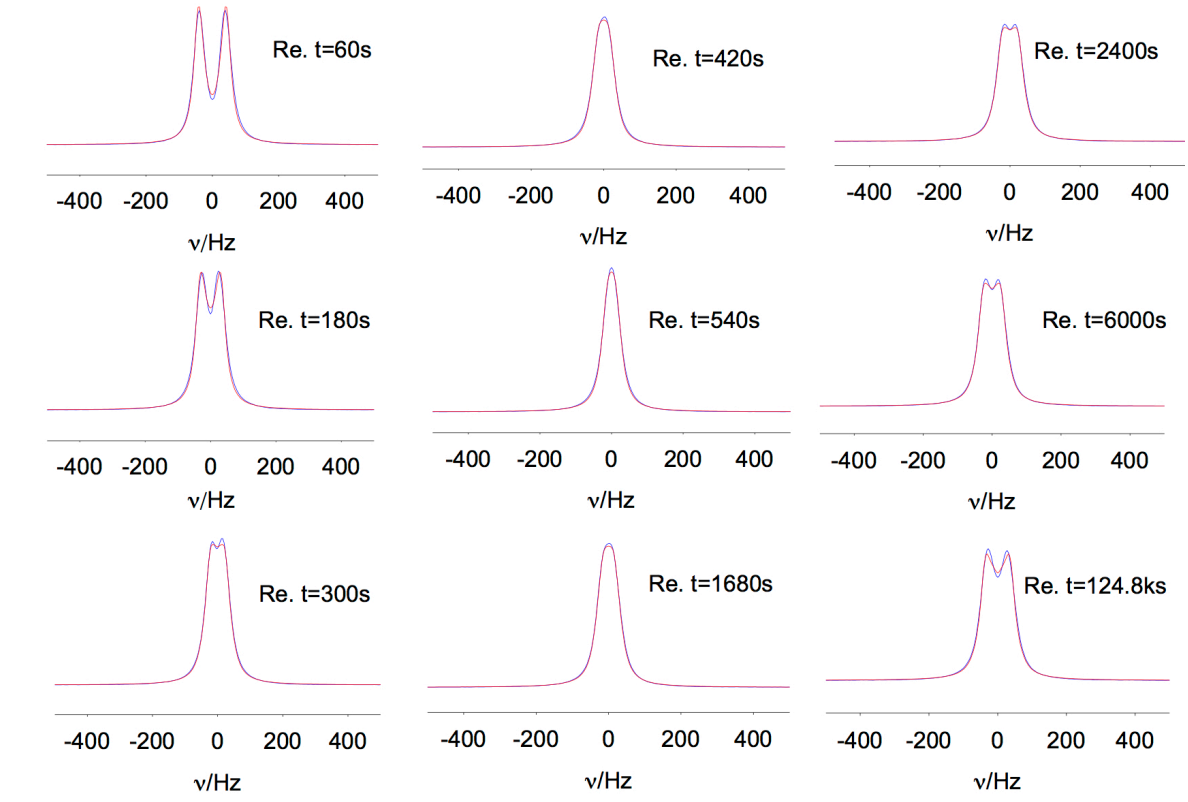

Figure 2-7 Spectra (blue line) and fits (red line) from the model at different times during relaxation.

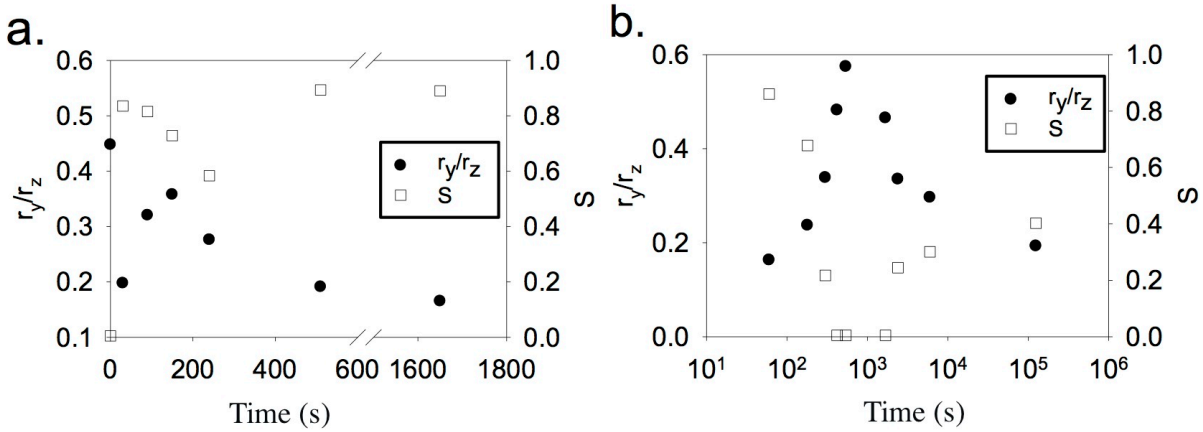

Figure 2-8 **a.** $r_y/r_z$and S obtained from the model fits during shear at different times. **b.** r_y/r_z and S obtained from the model fits during relaxation at different times.

During relaxation after shear cessation reported in Figure 2-8 *b* the WRR start from an asymmetric average form (low r_y/r_z) with high order then pass through a low order state with higher symmetry and finally approach an asymmetric state with intermediate order. This behavior of the WRR as the system evolves from state *IV* to state *I* shows that the cholesteric domains should be undergoing significant internal changes associated with the reposition of the cholesteric order and involving most

probably external dimensions readjustments also, that strongly influence the neighboring WRR. The value for S and r_y/r_z reported in Figure 2-8 are dependent upon the fixed values considered for the two model parameters S_{D_2o} and $l_{D_2o'}$ and should thus be considered as relative values.

2.6 Conclusion

The Rheo-NMR study presented in this chapter, analyses the HPC-water system under shear in the ranges 0.1 s^{-1} to 1.0 s^{-1} and relaxation and correlates it with a mesoscopic picture of the systems' structure in the different ordering states. This picture accounts well for the DNMR results recorded under shear and relaxation, is based on the accumulated knowledge on this system by other techniques[184] and considers the three distinct regions of steady shear flow observed for some liquid crystalline polymers[138].

This work gives added insights into the behavior of cellulosic materials under shear and relaxation revealing new features of the dynamics of appearance and disappearance of the cholesteric phase, which recently was found to be responsible for structural color of some plants [186].

Chapter 3 Structure and mechanical properties of sheared HPC film

This chapter's work description and discussion was based on the following papers:

S.N. Fernandes, Y. Geng, S. Vignolini, B.J. Glover, A.C. Trindade, J.P. Canejo, P.L. Almeida, P. Brogueira, M.H. Godinho "Structural color and iridescence in transparent sheared cellulosic films", *Macromolecular Chemistry & Physics*, **214**, 25−32 (2013).

Y. Geng, P.L. Almeida, S.N. Fernandes, C. Cheng, P. Palffy-Muhoray, M.H. Godinho, "A cellulose liquid crystal motor: a steam engine of the second kind", *Scientific Reports*, **3**, 1028, Doi:10.1038/srep01028 (2013).

3.1 Introduction

Recent work showed that certain plant species use micro- and nanostructures to create particular optical effects.[187,188,189] The floral iridescence exhibited by *Hibiscus trionum* and *Tulipa kaufmanniana* petals is due to surface diffracting gratings.[187] It has also been suggested that structural color generated through diffraction gratings might be widespread among flowering plants.[190]

In this chapter we describe, for the first time, a study on sheared iridescent solid cellulosic films, with tunable mechanical and structural color properties, which mimic the structures found in plants, namely in *Tulipa* petal gratings.

We also studied the mechanical properties of the shear casted thin HPC film both with moisture and without moisture. The capability of controlling the bending with the moisture exposure allowed us to make an application as a soft motor.

3.2 Experimental

(Hydroxypropyl)cellulose (HPC) was purchased from Sigma-Aldrich (M_W =100.000; $\overline{MS}$ = 3.5) and used as received. Nanocrystalline cellulose rods, that where introduced in chapter 1 (1.1.2), were kindly supplied by Professor Doctor D.G. Gray and used without further treatment. 0.1 *%*, 1 *%* and 5 *wt %* (calculated taking into account the solid content in solution HPC + NCC) nanocrystalline cellulose rods were added to distilled water and the NCC rods dispersed with a UP400S ultrasonic probe from *Hielsher* (until no NCC clusters could not be detected by eye), these were then used to prepare HPC aqueous solutions. Solutions of HPC in distilled water with concentrations that range from 57 to 65 *wt %* were prepared at room temperature. After the first week they were stirred every other day and kept away from light for at least 4 weeks until used.

Films were prepared from LC solutions, casted and sheared simultaneously by moving a calibrated Gardner knife from *Braive Instruments* at 1.25 $mm\ s^{-1}$ (Figure 3-1). The films were allowed to dry at room temperature and kept in a controlled relative humidity (20 *%*) chamber until further use. The thickness of the dried films was estimated from the average of 10 measurements by using a *Mitutoyo* digital micrometre.

The photos of the films were taken with a *Casio EX-F1 Exilim Pro* photographic camera. The bandwidth in polarizing optical microscope (POM) pictures were determined using *ImageJ* (*version*

1.45s, http://imagej.nih.gov/ij/). *Blender*, version 2.57b, was used to obtain the 3D draw of the shear-casting knife.

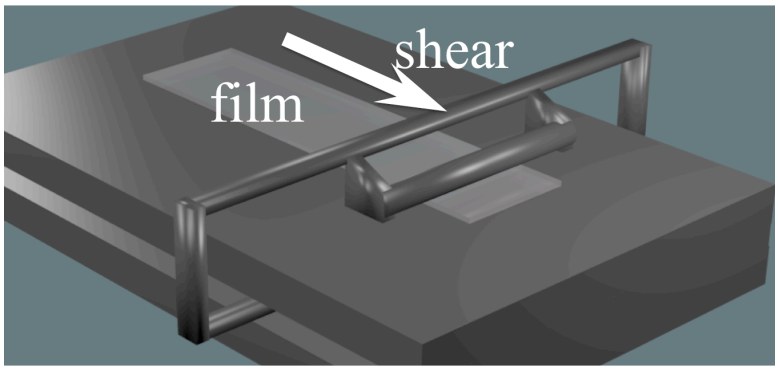

Figure 3-1 shear-casting knife was used to produce the films, as shown schematically

The wavelengths (λ_0) of the maximum selective reflection peaks were recorded with a *Jobin Yvon* monochromator *H10 Vis* mounted on the microscope stage, equipped with a photomultiplier and a chart recorder. Six measurements were obtained for each sample. The film's textures were observed using a POM *Olympus BH2* in transmission and reflection mode coupled to a *Canon EOS 550D* camera.

Small Angle Light Scattering (SALS) measurements were performed by illuminating the films with a laser beam (632 *nm*) at an incident angle - θ_i - of 30 º. The diffraction pattern of each film was projected on a white screen and recorded with a *Canon EOS 550D* camera. The diffraction was described quantitatively by the grating equation $N\lambda = \Delta l_1(\sin\theta_d - \sin\theta_i)$ where λ is the wavelength, N is the diffraction order and Δl_1 is the periodicity of the grating.

The mechanical properties of the samples were registered with a mini tensile testing machine from *Rheometric Scientific (Minimat Firmware Version 3.1)*. Small rectangular pieces of the cast films, with the dimensions of 5 *cm* x 2 *cm*, were cut in two distinct directions orthogonal to each other (*i. e.* with the longest dimension of the sample parallel to the direction of the casting shear and perpendicular to it). In addition, the film was stretched uniaxially at a rate of 5 $mm.min^{-1}$, along the longest sample dimension. The values of the mechanical properties of a given sample were taken to be the average of the results of six successful measurements.

The shear stress associated with bend to humid air has been measured, as function of time, in a 20 *mm* x 20 *mm* x 32 *μm* planar sample at 24 *ºC* with free surface exposed to humidity. Measurements were taken with *Mettler Toledo AG204* load sensor.

For the topographical characterization of the films surface, atomic force microscopy (AFM) data was acquired using a *dimension 3100 spm* with a *Nanoscope IIIa* controller from *Digital Instruments (DI)*.

All measurements were performed in tapping mode *TM* under ambient conditions. A commercial tapping mode etched silicon probe from *DI* and a 90 $\mu m \times 90\ \mu m$ scanner was used.

Scanning electronic microscopy (SEM) was used to imaging the topographical features of the films with a *SEM DSM962* model from *Zeiss*. Gold was deposited on the films by sputtering in an Ar atmosphere, using a 20 *mA* current, for 30 *s* at a deposition rate of 3 $\AA\ s^{-1}$. Images were captured for an acceleration voltage of 5 *kV*.

To construct the motor, the cellulosic film was produced in the form of a circular loop, 8.0 *cm* long, 1.0 *cm* wide, which passes over two 14 *mm* diameter wheels.

The water vapor was generated by an *AirProject* ultrasonic humidifier (*Italy ARTSANA Group*).

3.3 Result and discussion

3.3.1 Morphology and structural color and iridescence in transparent sheared cellulosic films

In our work, the material used to prepare replicas of the plant petal surface is a very well known cellulose derivative, HPC already introduced in chapter 1 (1.1.3 and 1.2.3), which can be easily dissolved in water generating liquid crystalline helicoidal phases with the pitch in the visible range depending on water content.[129] We chose this simple water lyotropic system because it is well studied[129,191,159,160] and has appropriate characteristics to incorporate hydrophilic nanocrystalline cellulose (NCC) rods. Several lyotropic aqueous solutions ranging from 58 to 65 *wt %* were prepared and in the same range of concentrations 0.1, 1.0 and 5.0 *wt %* of NCC rods were added.

All the solutions prepared showed iridescent colors. The maximum peak wavelength (λ_o) reflected by the samples for incident light normal to the surface may be expressed as, $\lambda_o = n_e P cos\theta$, where n_e is the refractive index, P the helical pitch and θ the angle between the light propagation direction and the helix axis.[192] The values of λ_o may therefore be tuned by altering the helical pitch or the average refractive index of the chiral nematic material.

We were able to vary λ_o of the solutions in the visible range by increasing the proportion of solvent relative to HPC and NCC rods (Figure 3-2 *a* and *b*), λ_o was found to depend on polymer concentration and very slightly on nanowhiskers content. The average refractive indices of the different mixture materials are essentially constant because the two components, crystalline cellulose and cellulose derivative matrix, have similar refractive indices (n_e = 1.54 and 1.33, respectively). The plot of the

reciprocal pitch against $\phi(1-\phi/3)/(1-\phi)^2$ gives a reasonable linear plot, for solutions with and without nanorods, that pass at the origin. Thus, the concentration dependence of the cholesteric pitch is in fairly good agreement with the theory of *Kimura et al.* [193] for different molecular weight samples and different degrees of substituents, per anhydroglucose unit.

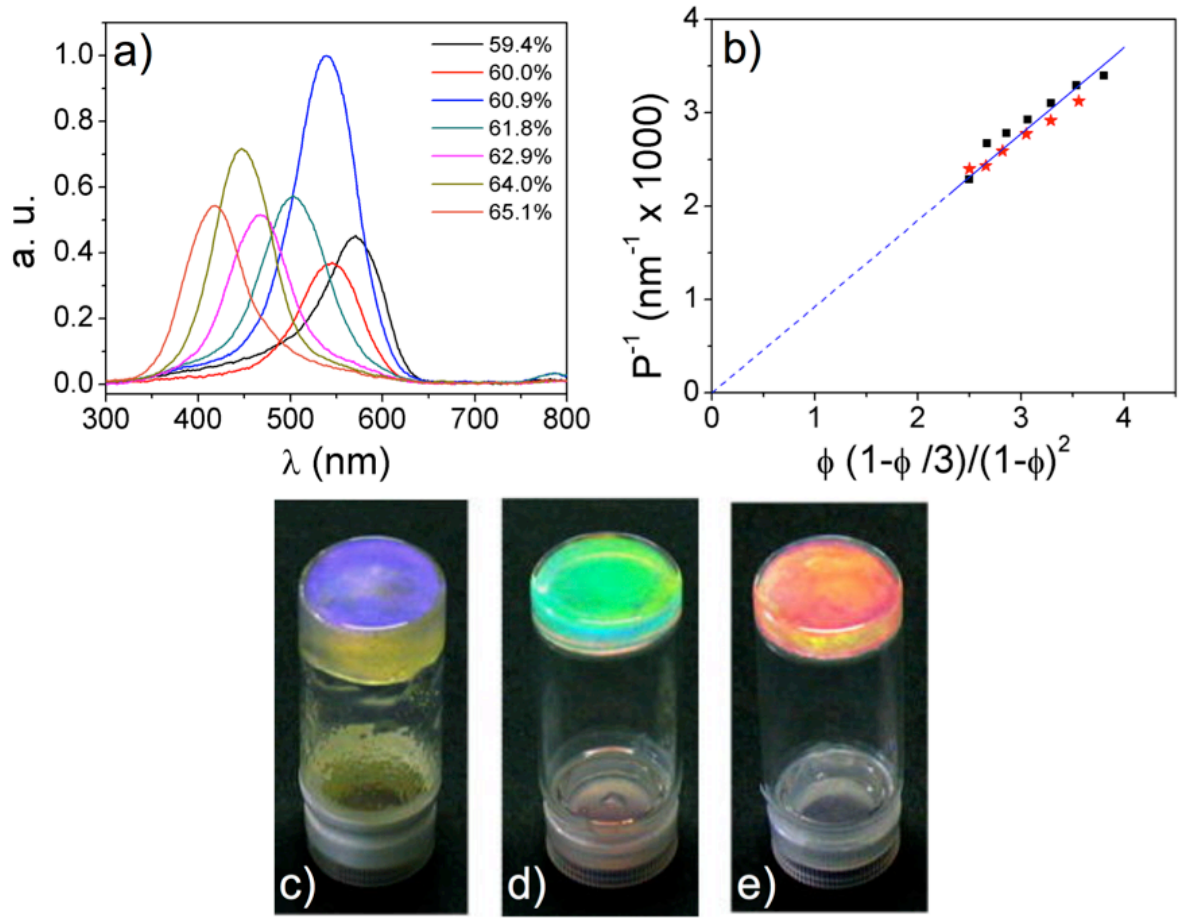

Figure 3-2 Concentrated liquid crystalline cellulosic solutions; **a.** and **b.** Visible spectra of anisotropic HPC solutions with nanocrystalline cellulose (NCC) are given along with the reciprocal pitch (P) against $\phi(1-\phi/3)/(1-\phi)^2$, where ϕ is the weight fraction of polymer in **b.** HPC/water solutions (■) and HPC/NCC/water solutions (★). **c.** to **e.** Liquid crystalline solutions obtained from HPC/NCC/water solutions, same NCC concentration (0.1 *wt %*) with 62 %, 60 % and 58 *wt %* of HPC in water, respectively.

The increase of the pitch with water content was reported long ago for the HPC/water system.[128,194] The solvent was found to stabilize the cholesteric liquid crystalline phase above a certain critical concentration.[128] The liquid crystalline phase arrangement can be attributed to the relatively stiff cellulose backbone. In fact the persistence length of HPC in aqueous solution varies from 13 to 21 *nm* [128], which makes HPC a semirigid polymer forcing a parallel orientation of the chains. The chirality of the cellulose chain imparts a twist to the parallel arrangement, and the flexible side chains and the solvent allow the polymer molecules to migrate and form an equilibrium helical configuration.

The fact that the helical pitch varies slightly by adding 0.1 *wt %* NCC rods is an indication that the

liquid crystalline characteristics of these solutions is not much affected by the presence of the NCC rods (Figure 3-2 *c* to *e*). NCC rods, with a diameter of 5 to 70 *nm* and a length of 100 to 250 *nm* [23] seem to pack along the oriented liquid crystalline segments with the rods' main axis parallel to the cellulosic backbone, which forms the polymeric matrix. In order to incorporate the NCC rods into the anisotropic HPC matrix first they were dispersed in water, which was possible due to the NCC rods´ hydrophilic nature. The liquid crystalline solutions were then prepared using the water NCC doped system (Figure 3-2 *c* to *e*).

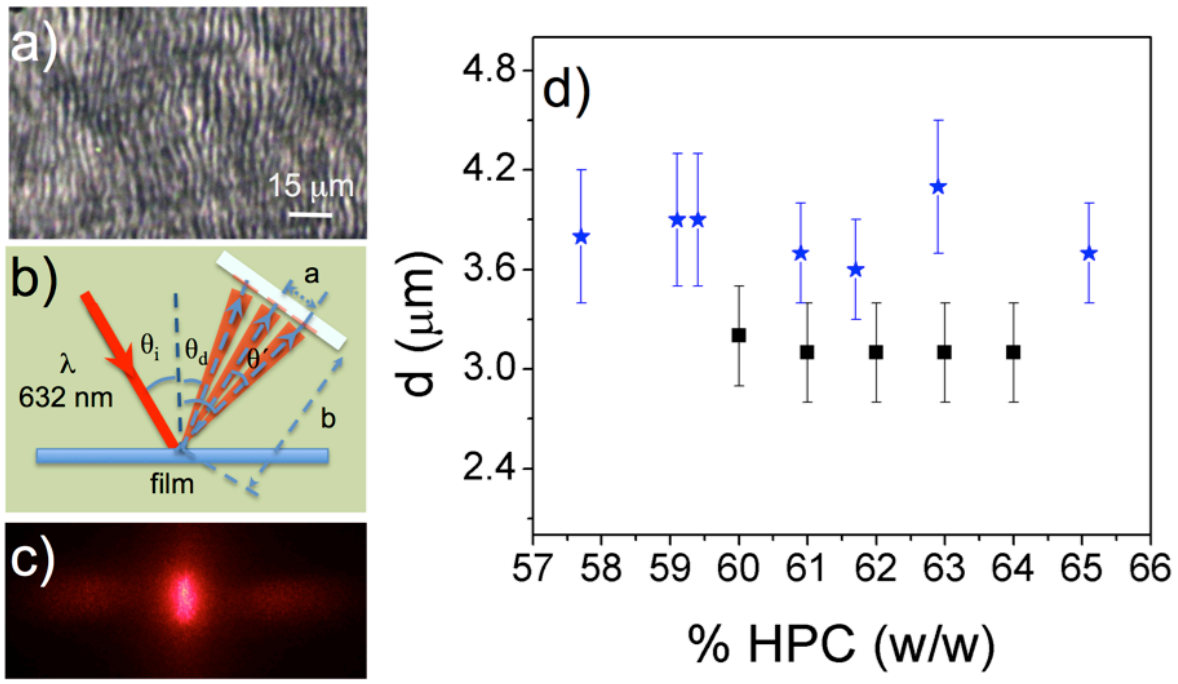

Figure 3-3 Characterization of large grating periodicities running perpendicular to shear direction detected by POM and SALS; **a.** transmission polarizing optical microscopy image, taken between cross polarizers, show bands which occur after the end of shear applied to the preparation and locked in the films after solvent evaporation. **b.** Scheme representation of the SALS measurement geometry and detector set-up. The laser light (λ= 632 nm) incidence angle is, θ_i, equal to 30 º. The light is reflected by the surface of the films at an angle $\theta_d=\theta_i\pm\theta'$. **c.** Diffraction pattern of one of the gratings (4.0±2 μm) in reflection observed for a solid film cast from a cellulosic solution with NCC (0.1 *wt %*). **d**. Influence of solution concentration and NCC particles on large gratings periodicity d for shear casted solid films prepared from different HPC/water by weight concentration (HPC *wt %*), (★) films with HPC/NCC and (■) HPC films.

In order to investigate the textures of the freestanding HPC and HPC/NCC films we analyzed them by POM and a similar banded structure was observed (Figure 3-3 *a*). This band structure consists of bright bands and dark lines alternate and perpendicular to the shear when viewed between cross polarizers, the textures observed are not compatible with a cholesteric lamellar structure. These patterns are usually described as a relaxation process, which occur immediately after the end of a shear applied to polymer liquid crystalline solutions.[195] They are described in detail in the literature and also introduced in the introduction part.[196] Band structures were associated with a long-range undulation of the director orientation[197] and can be frozen in the solid films after solvent evaporation.[169]

The air surface structure of the freestanding films was also investigated by SALS (see scheme in Figure 3-3 *b* and also in Figure 3-4) From Figure 3-4 we can see that:

$$N\lambda = d(sin\theta_d - sin\theta_i)$$

$$\theta_d = \theta_i + \theta' \ (\theta = 30°C)$$

$$sin\theta' = a/\sqrt{a^2 + b^2}$$

$$sin\theta_d = sin\theta_i cos\theta' + sin\theta' cos\theta_i$$

The diffraction pattern, caused by the interaction of the laser ($\lambda = 632\ nm$) light with the transparent and uniform material showed a periodicity *d* along the direction perpendicular to shear. This indicates that the material surface develops a periodical grating perpendicular to shear direction. In average the surface periodicities of the HPC and HPC+NCC films are of the order of 3.1 ± 0.3 μm and 3.8 ± 0.4 μm, respectively, and are not much affected by polymer content. Increasing the material strength and endurance, due to the presence of the NCC rods, could lead to more pronounced effects in bands spacing if the periodic oscillation of the orientation of the director is only attributed to contraction strains of the sheared sample induced by stress relaxation after cessation of flow. Nevertheless the periodicity for HPC/NCC films is slightly higher, which is a consequence of the anisotropic properties of the films and the brittle behavior promoted by adding the NCC rods.

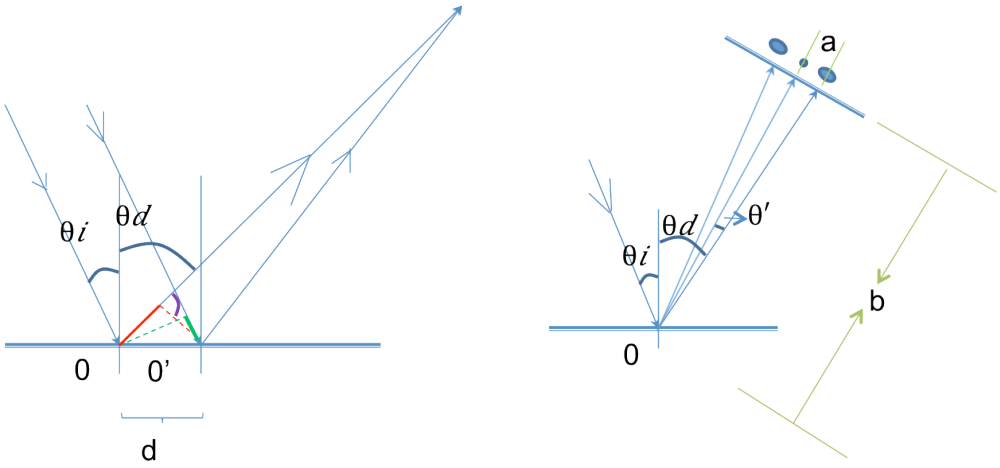

Figure 3-4 The principle of the SALS.

To further investigate the bands structure the HPC/NCC films surfaces were investigated by AFM (Figure 3-5) and two different scale periodical gratings were observed: the primary set of bands, already characterized by SALS, perpendicular to the shear direction, and a smoother texture characterized by a secondary periodic structure containing "small" bands. The analysis of the height profile at the two cross sections, *AA´* and *BB´*, is shown in Figure 3-5 *b*. Cross section *AA´* was taken along the shear direction. The periodicity of the larger bands, $\Delta\ell_1$, and the average peak-to-valley

height for these bands, h_1, were determined from *AA'* height profile plot, as indicated. Cross section *BB'* was taken along the direction of the secondary periodic "small" bands. The periodicity of the "small" bands, $\Delta\ell_2$, and their peak-to-valley height, h_2, were measured from the *BB'* height profile plot, as indicated in Figure 3-5 *a* and *b*. The arrows on the top of the image along the *AA'* and *BB'* lines mark the points used for the measurements performed in the height profile plots. In accordance with the SALS results, for the primary set of bands, the parameters $\Delta\ell_1$ and h_1 are higher for films prepared with NCC rods and do not depend strongly on polymer content (Figure 3-3 *d* and Table 3-1). Unlike primary bands the secondary bands $\Delta\ell_2$ and h_2 values, for all the HPC and HPC/NCC cellulosic films prepared and reported in the literature, [162] show a net tendency to decrease with polymer content. Figure 3-5 *c* shows a top view image of the height scan of the surface shown in Figure 3-5 *a*. The out-of-plane angle of the sinusoidal variation in the molecular orientation, $\theta_p = \tan^{-1}\left(\frac{h_1}{\Delta\ell_{OP}}\right)$, is obtained from the projection of the peak of one secondary band on the horizontal plane ($\Delta\ell_{OP}$).

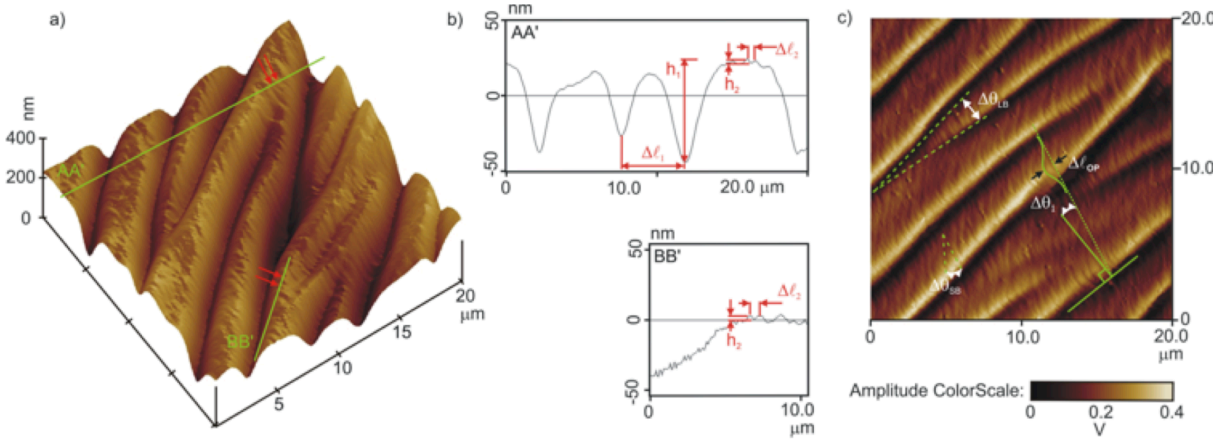

Figure 3-5 AFM images. **a**. 3D topography image (20 x 20 μm^2 scan) of the free surface of a sheared film prepared from 60 *wt %* HPC + 0.1 *wt %* NCC solution at a shear rate v = 1.25 *mm* s^{-1}. **b**. Height profile analysis at the two cross sections: *AA'* and *BB'*. The arrows on the top of a view image along *AA'* and *BB'* lines mark the points used for the measurements of the height profile. *AA'* highlights characteristic properties of the primary bands (h_1 and $\Delta\ell_1$) and BB' those of the secondary bands (h_2 and $\Delta\ell_2$). **c**. Top view image of the amplitude scan of the surface shown in **a**. The secondary set of bands is at the angle $\Delta\theta_l$ to the shear direction. The horizontal distance between the line that joins both valley coordinates of a secondary band and the point obtained from the projection of the peak of the same secondary band on the horizontal plane, $\Delta\ell_{OP}$, is used to calculate the out-of-plane angle of the sinusoidal variation in the molecular orientation, θp. Defects occurring in the film surface give branched extra layers inserted at an angle $\Delta\theta_{LB}$. $\Delta\theta_{SB}$ is the angle that the small bands make with the shear direction.

The results obtained indicate that the optical and mechanical properties of the HPC and HPC/NCC films can be tuned as a function of the initial characteristics of the liquid crystalline solutions and quantity of NCC rods.

Table 3-1 The parameters vary with the concentration in Figure 3-5.

HPC [*wt %*]	*NCC* [*wt %*]	$\Delta\ell_1$ [μm]	h_1 [nm]	$\Delta\ell_2$ [μm]	h_2 [nm]	$\Delta\theta_l$ [deg]	θ_p [deg]
50		4.3-5.2	84-89	1.42-1.80	4.5-9.5	≈8	
55		3.1-4.3	87-96	0.72-1.80	3.5-9.0	< 14	
60		2.9-3.2	71-98	0.55-0.67	4.4-5.0	30	9-12
65		2.9-3.3	80-100	0.44-0.59	4.8	26	15
65	0.1	2.4-3.0	80-90	0.4-0.7	1.7-2.5	42-46	9-14
65	1	2.8-4.4	80-160	0.5	5	20-26	
65	5	2.4-4.0	80-160	0.4-0.5	2-5	29-45	11-15

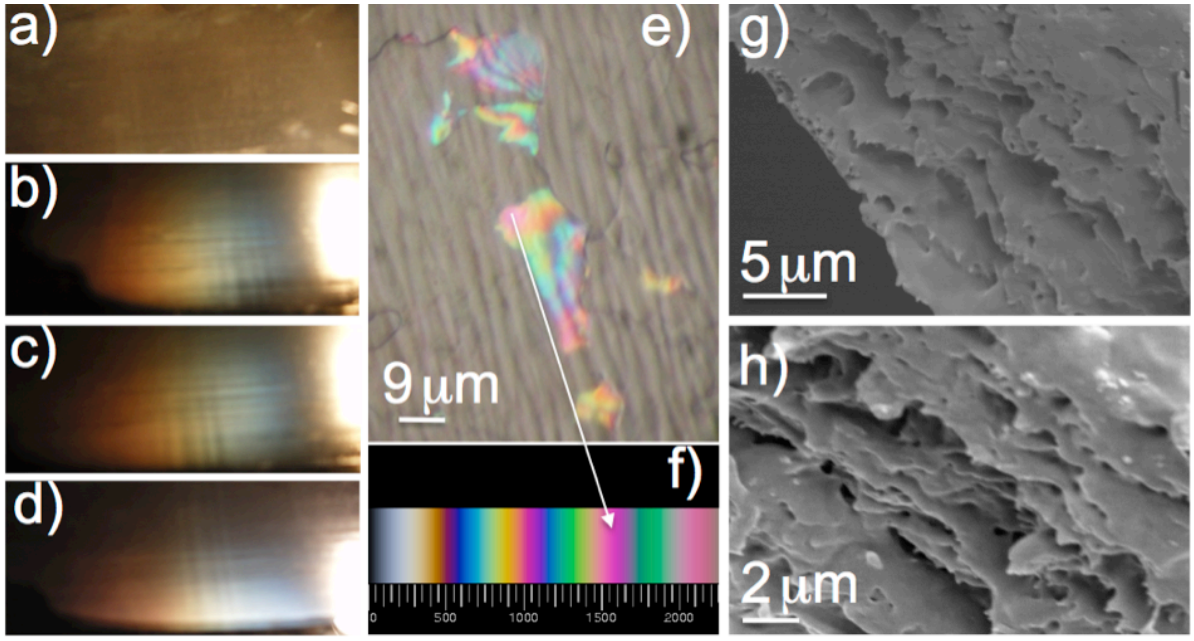

Figure 3-6 **a**. to **d**. correspond to reflection photos taken at different incident angles of white light films illumination. The variation of the film colors depends on the light incidence angle and for normal incidence the films look macroscopically transparent **a. b.** to **d.** shifting patterns of color as the view angle changes. The different colors when viewed from different angles, iridescence, are due to the periodic structure of the material. **e.** POM photo in reflection mode, parallel polarizers, showing some interference colors at the border of black line defects. These colors are an indication that at small regions the distance between the layers, that can be observed in the film cross-section by SEM, are of the order of 120 to 250 *nm* calculated by taking into account the color transition blue-magenta as observed and in the Newton scale **f** and the refractive index of HPC (1.33). **g.** and **h**. represent SEM pictures of the cross section of the sheared HPC films. A layered structure parallel to the films surface can be observed and also a periodic reminiscent "pins" from a structure, which exists in between the layers. The periodic structure that exists in between the layers seems responsible for the angle color dependence of the films.

In fact NCC rods are very interesting materials that can originate chiral nematic organization and like other cholesteric materials, which can be duplicated in polymer networks[198], they can be replicated in pure silica films.[124] Stacked layers that result from the helical pitch of the chiral nematic phase were obtained. Such periodic structures, with a repeating distance of the order of P/2, can also be found in

thin sections of biological materials. A twisted plywood model was proposed by *Bouligand* [199] in order to account for such architecture.

In the case of our sheared films, X-rays [162] and POM (Figure 3-3 *a*) measurements indicate that the cholesteric organization of the initial solution is destroyed and that a bundle of wrapped helicoidal fiber-like structures developed with the fibers residually oriented along the shear direction. The sheared banded cellulosic films are typically described as transparent with no mention of structural or iridescent colors (see photo Figure 3-8). We found that these transparent films have the potential to generate shifting patterns of color as the viewer moves, they possess the ability of reflect one particular peak wavelength of light at one angle, and another peak wavelength at a second angle. This iridescence covers some different colors in the region of the visible spectrum (Figure 3-6 *a* - *d*). We also found that if the bottom surface of the freestanding films is observed under a microscope, in the reflection mode, different interference colors can be seen at the border of some line defects (Figure 3-6 *e*). Iridescence and the majority of structural color can be produced by coherent light scattering, which occurs when the distribution of light-scattering elements, and the resulting phase relationship of reflected light waves, is precisely ordered. The simplest type of coherent light scattering is that of thin film interference, which gives color to soap bubbles and oil-slicked puddles. Diffraction gratings consisting of a reflective surface over which runs a series of ordered and precisely spaced parallel grooves, and can also produce iridescence. [200] The colors observed for the cellulosic films described in this work can be attributed to the 3D periodical bands surface gratings observed by AFM (Figure 3-5 *a*) at the micro and nano-scale. Nevertheless, SEM pictures taken perpendicular to the film surface show a layered structure connected by a network of "holes" (Figure 3-6 *h* and *g*). The border of the cross section layers is adorned with "pins", which seems reminiscent of a structure that exists in the layers. The bottom film surface was observed by SEM and is essentially flat. By POM in the reflection mode black lines can be observed and must correspond to the border of the layers observed by SEM in the film cross section.

The spacing between the layers observed by SEM is of the order of microns and at small confined regions on the film surface some interference colors can be observed (Figure 3-6 *e*). The sequence of colors in those minor domains of the films is similar to the Newton series reflected from a thin film of oil on water.[201] The Newton series is a very characteristic sequence of repeated color bands grouped into orders. Taking into account the refraction index of the films (1.33) and the Newton series, displayed in Figure 3-6 *f*, the thickness between those layers, restricted to small sample domains, varies from 1.5 to 2 μm, which for normal incidence is out of the visible range.

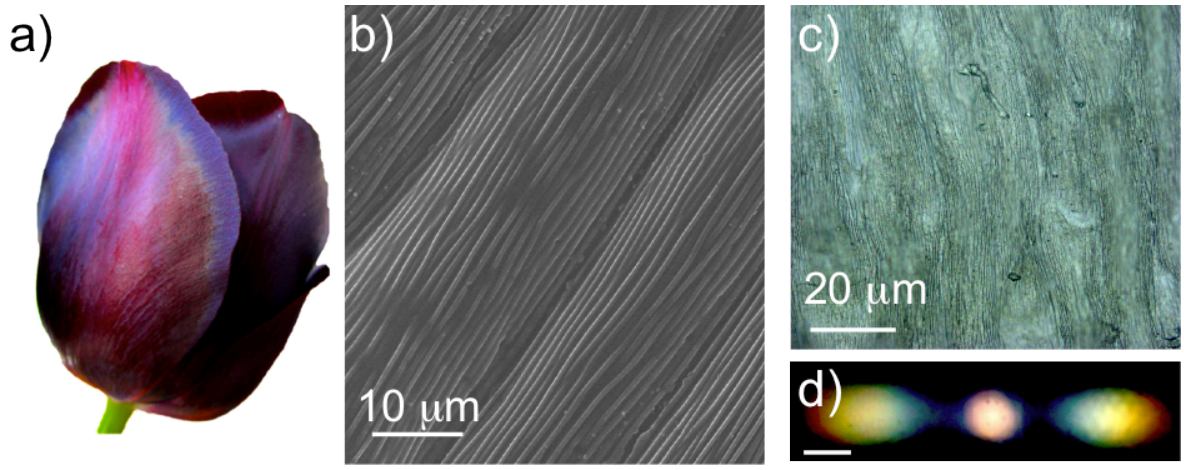

Figure 3-7 *Tulip* Queen of the Night petals gratings **a.** Picture of the *Tulip* Queen of the Night flower. **b**. The SEM image shows the striated epidermis of the flower; the periodicity is in the order of 2 μm comparable to the one of the films. **c.** Optical microscope reflection image of the peeled epidermal layer of the petal. The transparent epidermal layer maintains the regularity of the striation also after the peeling process. **d.** K-space imaging of the peeled epidermal layer showing iridescence. Please note that the scale bar in d correspond to 20 *degree*.

The surface characteristic patterns found by AFM, as well as the lamellar structure observed by SEM in our cellulosic films, can also be seen in plants. [196] In fact we observed the surface of Tulip "Queen of the Night" petals (Figure 3-7 *a*). The SEM image in Figure 3-7 *b* shows the periodical striation, of about 1.5 μm spaced, responsible of the iridescence of the petal. The single epidermal layer, once is peeled from the petal, is transparent and the contribution from the ordered grating can be separated from the underneath layer contacting pigment and the iridescence can be measure using a K-space imaging system (*Bertrand Lens*), (Figure 3-7 *d*).

3.3.2 Mechanical properties of transparent sheared cellulosic films

In this chapter, we secondly describe the study of the mechanical properties of the thin film with NCC. NCC filler as a probe also have been incorporated into composite materials, to enhancing their mechanical properties [204], which can influence the mechanical properties of the films but does not destroy the liquid crystalline characteristics of the composite material.

Anisotropic HPC films are formed by the evaporation of water from liquid crystalline aqueous HPC solutions (60 *wt %*). In preparing samples, solutions are initially on a glass substrate, with a free surface exposed to air as shown in Figure 3-1 and Figure 3-10. When the cellulose concentration is sufficiently high for the formation of the liquid crystal phase, the mesogenic fragments can be uniformly aligned in the sample by shear as discussed before. Shear is applied via a calibrated Gardner knife moving at a controlled speed of 1.25 $mm\ s^{-1}$ on the free surface, as shown in Figure 3-1 the

process produces a monodomain nematic sample. As indicated by X-ray studies [202], the director aligns along the shear direction. This can also be seen in Figure 3-5. The final film thickness is ≈ 40 μm. The grooves, whose wave vector is along the shear direction, are ≈ 3 μm apart, with amplitude ≈ 45 nm. The structure of the film near the glass surface is less well understood. Here, the solvent remains during shear, so less alignment is expected. The films, removed from the substrate, are large area, free-standing flexible macroscopic samples. So the mechanical properties of this thin film vary with different surfaces and also different directions. As we can see in Figure 3-8, the bending of the freestanding thin film is very different depending on which surface is upwards and also the shear alignment direction compare to the pencil axis. One can clearly see that the film bends more when the shear direction is perpendicular to the pencil than parallel. This fact is due to the existence of grooves. Also, the film bends more when the free surface (the surface that contacts with air during preparation) is downward, because the upper surface is more rigid.

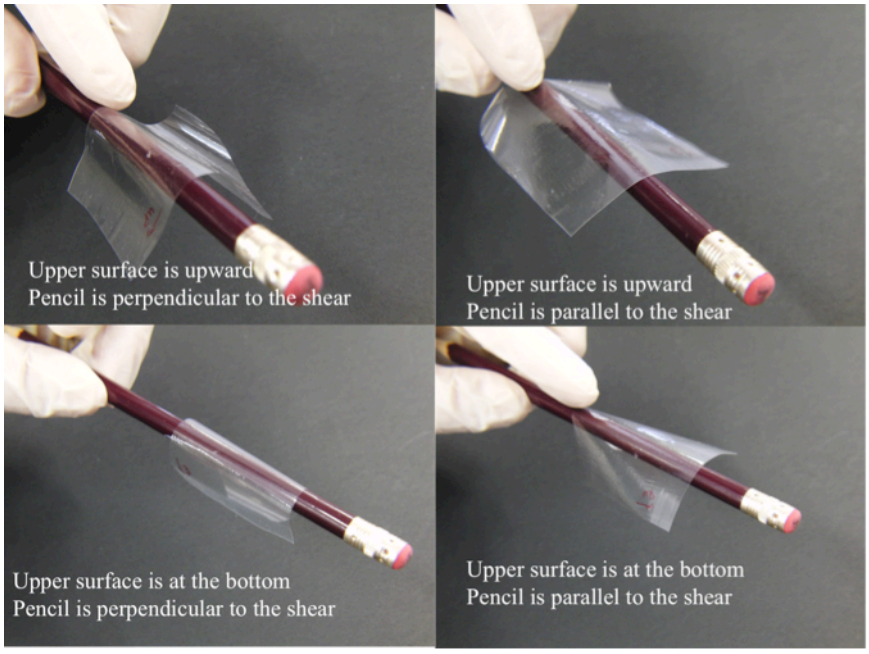

Figure 3-8 A freestanding sheared film prepared from HPC/NCC water 60 *wt %* solution

The modulus of the cellulose network has been measured for strain along the director, as well as perpendicular to it. Results are shown in Figure 3-9; for small strains, Young's modulus is 263 ± 39 *MPa* for shear parallel and is 140 ± 9 *MPa* perpendicular to the director. Above a threshold of 4 *MPa*, the stress in the perpendicular direction is nearly independent of the strain. This "semi-soft" elastic response is characteristic of liquid crystal elastomers [203].

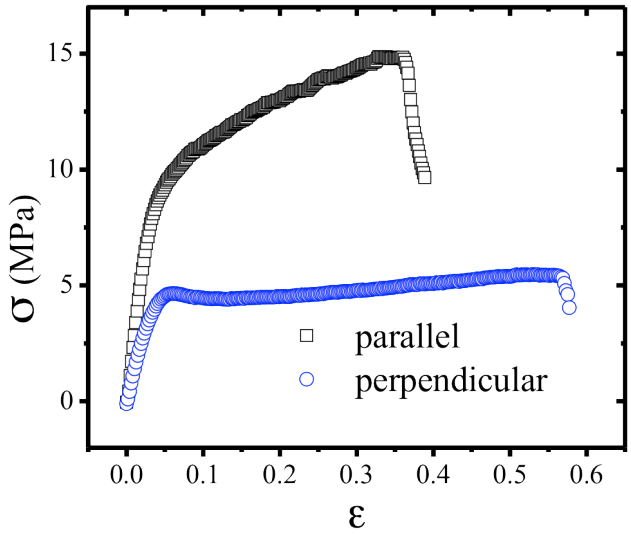

Figure 3-9 Stress-strain relations. Squares correspond to strain parallel to the shear direction and the nematic director. Circles correspond to strain perpendicular to the shear direction and the nematic director. For this geometry, above a threshold, the stress is nearly independent of strain. This indicates 'semi-soft' elasticity, characteristic of nematic elastomers. The negative slope at higher strains corresponds to failure due to tearing of the films.

In fact adding 0.1 % of NCC rods implies that the Young's modulus of the films, as well as the tensile strength, measured in perpendicular (*Per*) and parallel (*Par*) directions to the casting, increased by a factor of 2.5 and 3.2 for *Par* and 3.0 and 2.2 for *Per*, respectively, compared with films prepared from HPC anisotropic solutions, as can be seen in Table 3-2. Because of the high degree of molecular orientation, the HPC and the HPC/NCC films exhibit high modulus and strength along the shear direction and the mechanical strength in the transverse direction is low (Table 3-2). These anisotropic mechanical properties are consistent with the molecular orientation, which results from the flow of the liquid crystalline solution under shear stress. The fact that the Young's modulus and strength is much higher for HPC/NCC compared with HPC films, along the shear direction, is an indication that NCC rods align along this direction when the films are prepared. The significant improvement in the matrix modulus was also observed for other NCC composite materials, namely poly(styrene-*co*-n-butyl acrylate) (PBA) latex/NCC, and the enhanced mechanical properties have been attributed to a hydrogen bond network,[204] which can not be ruled out in our system. NCC rods and HPC have available hydroxyl groups, which could generate a hydrogen bond network between the filler and the cellulose based matrix. The most important fact is that a very small amount of NCC rods added to the liquid crystalline solutions implies a large improvement in the mechanical properties of the anisotropic films and did not disrupt the liquid crystalline order of the solutions.

Table 3-2 The bands perpendicular to the shear direction width, Young's modulus (*E*), the tensile stress (σ), strain deformation (ε) and the thickness of the films prepared from a HPC and HPC/NCC 62 *wt %* water liquid crystalline solution. *Par* and *Per* means that the mechanical stress strain measurements were performed along the parallel and the transverse directions to the shear casting direction, respectively.

NCC	Bandwidth	E (*MPa*)		σ (*MPa*)		ε (%)		Thickness
[*wt %*]	[*mm*]	*Par.*	*Per.*	*Par.*	*Per.*	*Par.*	*Per.*	[*μm*]
0	3.1 ± 0.3	263 ± 39	140 ± 9	17 ± 3	6 ± 2	38 ± 3	60 ± 11	21 ± 4
0.1	3.6 ± 0.3	650 ± 54	450 ± 63	51 ± 2	13 ± 3	21 ± 6	56 ± 2	14 ± 4

3.3.3 Bending of sheared HPC thin film to moisture

When exposed to water vapor, free standing films prepared from a 60 *wt %* solution bend, as shown in Figure 3-10. and Figure 3-11 When water vapor penetrates the free surface of the film, the sample bends around an axis parallel to the shear direction, with the free surface on the outside (Figure 3-11 *a*). This is consistent with expansion of the free surface of the film in the direction perpendicular to the director. Such an expansion is expected, since the order parameter is reduced by the presence of the solvent water, and furthermore the presence of water molecules between the cellulose chains in the rigid segments is expected to increase the thickness of the rod-like fragments. The scheme in Figure 3-12 shows the mechanism of a dimensional contraction induced by the loss of the director´s orientation.

When the film is allowed to dry, either by heating or by being placed in a low-humidity environment, the film unbends, reversibly assuming its original shape.

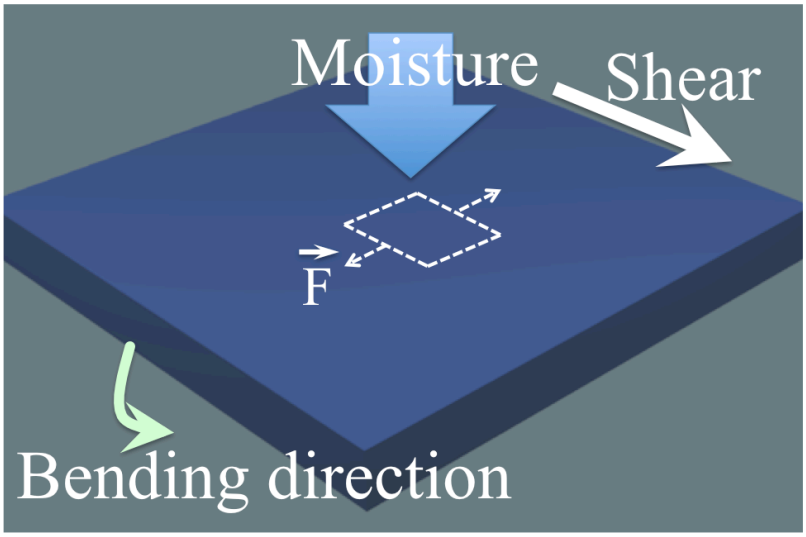

Figure 3-10 The schema of the bending of film to moisture.

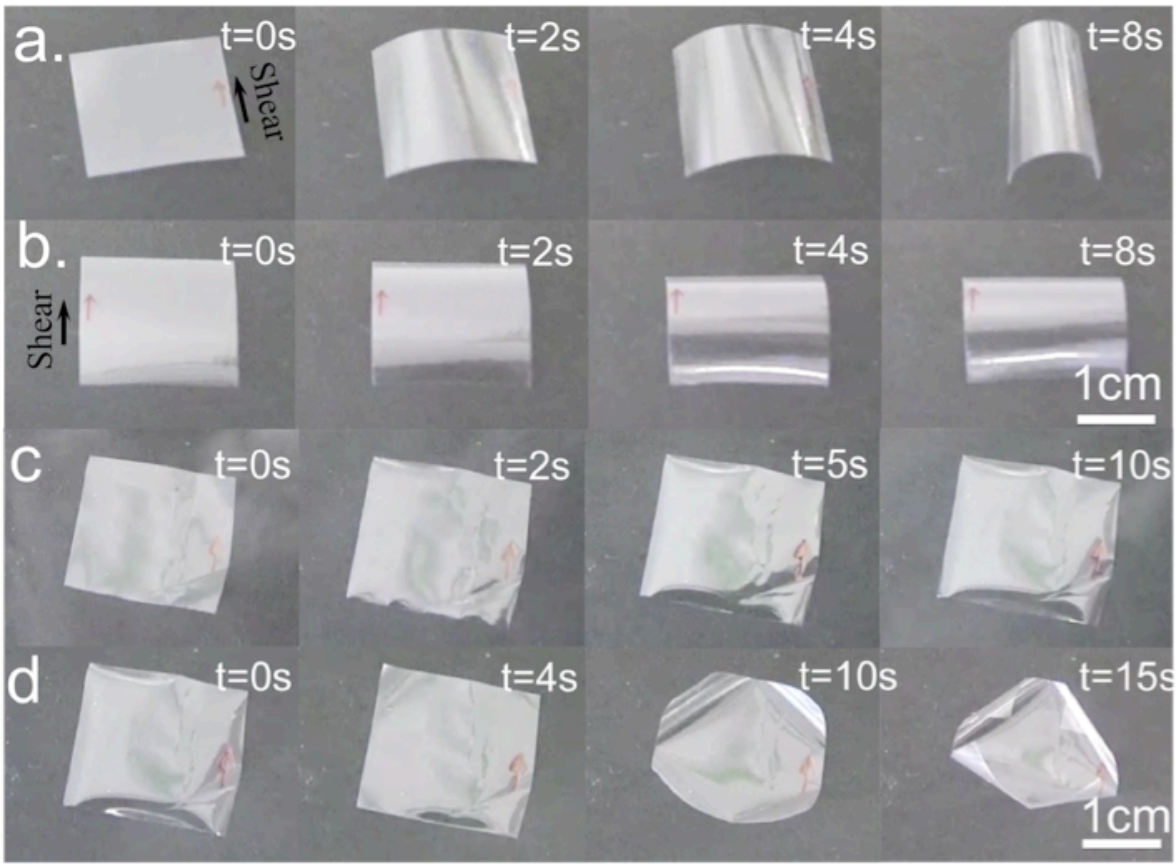

Figure 3-11 Bending of free standing films. **a.** The film free top surface and **b.** the film glass bottom surface exposed to water vapor. Sheared films were prepared from liquid crystalline HPC/water solution, the arrows indicate shear direction, **c.** and **d.** for the bending and recovering process of the thin film prepared under the same process with the film from a and b but from isotropic solution with low concentration.

Interestingly, when the glass side of the film is exposed to water vapor, it bends around an axis perpendicular to the shear direction, with the glass side being convex(Figure 3-11 *b*.). This is consistent with a nearly isotropic expansion of the glass side surface due to the presence of moisture. Since corrugations on the free surface give rise to a smaller effective modulus for bend in this direction, as has been confirmed by independent measurements, bend occurs around an axis perpendicular to the shear direction. The bend produced by exposing the glass side to water vapor is considerably smaller than that of the free surface. When the film made of isotropic solution exposed to moisture as shown in Figure 3-11 *c*, the bending is very different as *a* and *b.* Because in isotropic solution there is no order as in cholesteric phase and the molecules are not so cross-linked by hydrogen bond with the good alignment. When the solution under the shear condition, the molecules are also aligned by the shear but they are more free to relax and lose the alignment. So the film from the isotropic solution is isotropic. When the film is exposed to the moisture, the water molecules go into the film and increase the distance of the HPC molecules, which induces the expansion to every direction of the surface exposed to moisture. The water molecules also give the freedom to the HPC molecules, which likes annealing process, and HPC molecules start to pack and reduce the dimension

in every direction. When stop to give the moisture, the water molecules start to come out of the film and the film start bending like it is shown in Figure 3-11 *c d* and Figure 3-13 *c*.

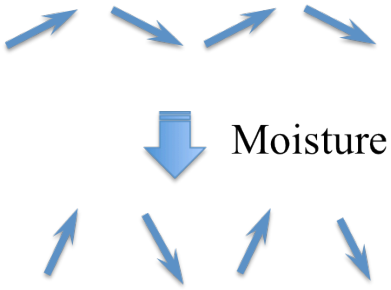

Figure 3-12 Director changing when the sheared film exposed to moisture.

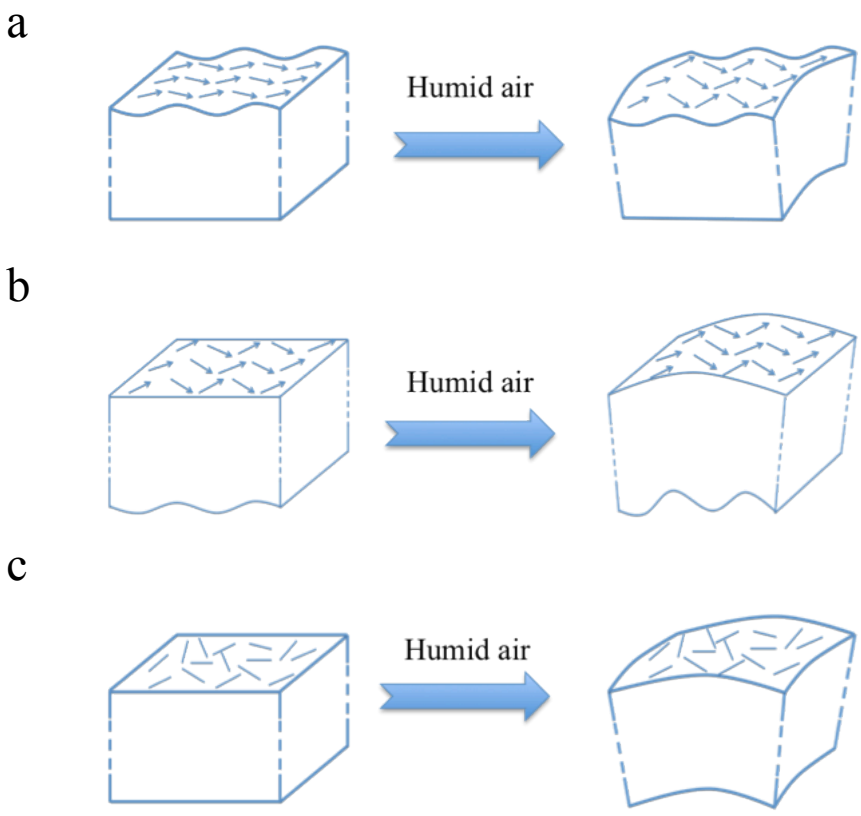

Figure 3-13 Schema of the different surfaces bending and the director changing when exposed to moisture, **a.** with the free surface (contact with air), **b.** bottom surface (contact with glass) respectively and **c.** the film is from isotropic solution.

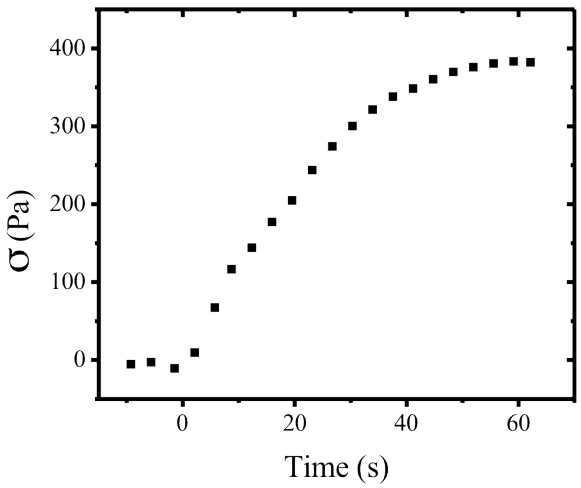

Figure 3-14 Dynamics of stress evolution. Shear stress in a 20 $mm \times 20\ mm \times 32\ \mu m$ planar sample at 24 ^{o}C with free surface exposed to humidity as function of time, measured with a *Mettler Toledo AG204* load sensor. The maximum stress measured was 383 *Pa*.

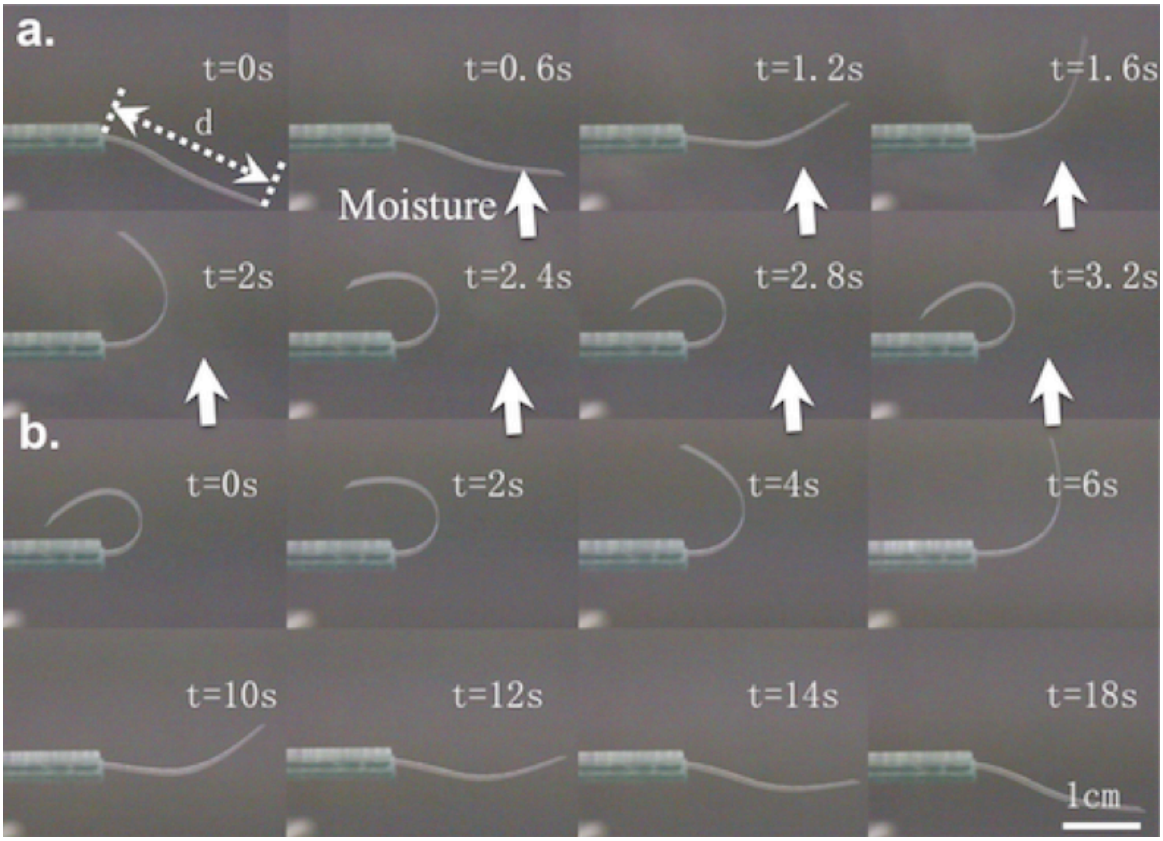

Figure 3-15 The moisture mechanical response of cellulosic network samples. **a.** Frames from a video clip recording the bending dynamics of a sample (sample dimensions around 0.5 *cm* x 2.5 *cm* x 30 μm) anchored at one end and exposed to moisture from below for 4 *s*. **b.** Graphs of the dynamics of force produced by a 70 μm sample for different times (graph on the left) and for t = 30 *s* moisture exposure for samples with different thicknesses (graph on the right). The free end of the samples were held in place and prevented from bending by the arm of a mini tensile test machine (*minimat*) load sensor measuring the force. The insets show the existence of a critical exposure time and sample thickness.

The shear stress associated with such bend has been measured, as function of time (Figure 3-14), in a 20 *mm* x 20 *mm* x 32 *μm* planar sample at 24 *ºC* with free surface exposed to humidity. Measurements were taken with *Mettler Toledo AG204* load sensor. The maximum stress measured was 383 *Pa*.

In order to check the response time, we exposed, for different times of sizes around 1 *cm* x 2 *cm* x 32 *μm* supported at one end (Figure 3-15 *a*) to ultrasonic moisture excitation. The axis of the cylindrical bend is perpendicular to the "bands" and parallel to the average alignment of the director, whose direction in the sample is known. The size of deformation and its timescales are dependent on time moisture exposition and films thicknesses.

The observed bending is reversible and should result from a rapid material expansion perpendicular to the shear direction at moisture-exposed surface. We also checked the response time when exposed to the moisture and also the recovering process as show in Figure 3-16 by checking the distance *d* of the two ends of the sample as shown in Figure 3-15 and the bending is relatively fast, on the scale of around 1 *s*.

Water vapor induced bend has been demonstrated in DNA covered Si cantilevers[205], as well as in a different LCN system with a different geometry by *Broer et al.*[206]. In this work we have exploited such a bending phenomenon and also have tried to find some application by producing a humidity driven rotary motor.

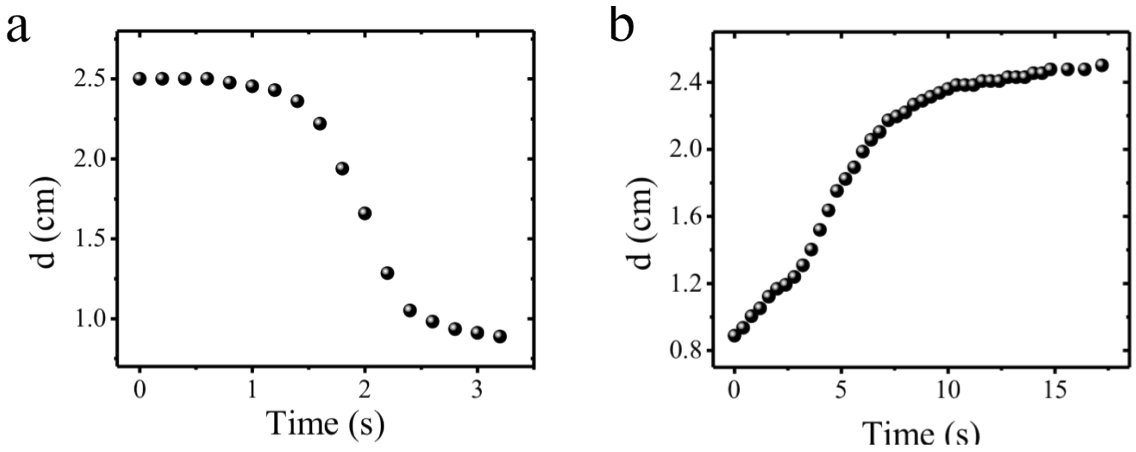

Figure 3-16 The evolution of distance *d* in Figure 3-15, **a.** the bending process and **b.** the recovering process.

3.3.4 An application of the bending to moisture -- A cellulose liquid crystal motor: a steam engine of the second kind

There are a wide variety of definitions of motors in the literature. We choose here to define a motor as a device, which uses energy, but not momentum, to produce motion. Engines may be defined as motors, which obtain energy from a fuel. We used belts of anisotropic HPC films (prepared from solutions in water 60 *wt %*) to produce our humidity driven motor, as shown below.

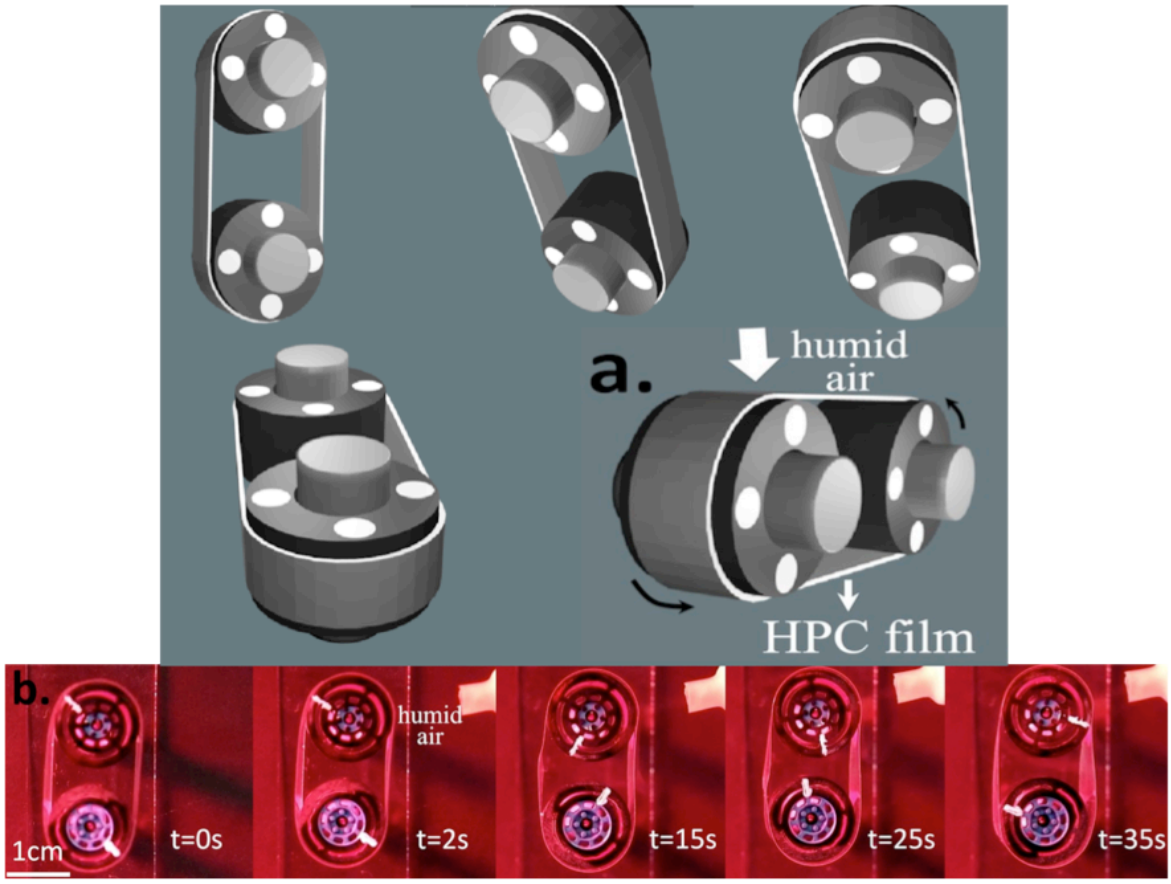

Figure 3-17 Moisture-driven liquid crystal cellulose engine. **a.** Schematic of the motor, showing location of moist air and rotation direction. The alignment direction is parallel to the axes of the wheels. The free surface of the film is on the outer side. **b.** Series of video frames showing rotation. The motor is housed in a dry environment. Momentum transfer from the moist air is small, and opposes the observed motion. Belt dimensions are: 1.0 *cm* x 8.0 *cm* x 30 μm; wheel diameter is 14 *mm*. The direction of rotation is indicated by a black arrow, and of moist air flow by a white arrow a.

A monodomain nematic HPC film was produced in the form of a circular loop, 8.0 *cm* long, and 1.0 *cm* wide (Figure 3-17). The alignment direction is in the plane of the film, perpendicular to the long edges. The loop was passed over two 14 *mm* diameter wheels with horizontal axes. When humid air was applied to the outer side of the film near one of the wheels, as shown in Figure 3-17, the wheels began to rotate, and continued so long as humid air was present. The motion is caused by

humidity-induced bend of the liquid crystalline HPC film. A heuristic explanation for the motion is as follows. If the tension in the film is assumed to be nearly uniform, the humidity induced bend shortens the lever arm on the side where the moist air is applied, resulting on a net torque on the wheel and causing rotation of the wheel as illustrated schematically in Figure 3-18. We have estimated the tensile stress from the shape of the circular film loop to be 357 *Pa*, which is close to the shear stress produced by humidity. We conjecture that these two quantities need to be comparable for the engine to operate efficiently.

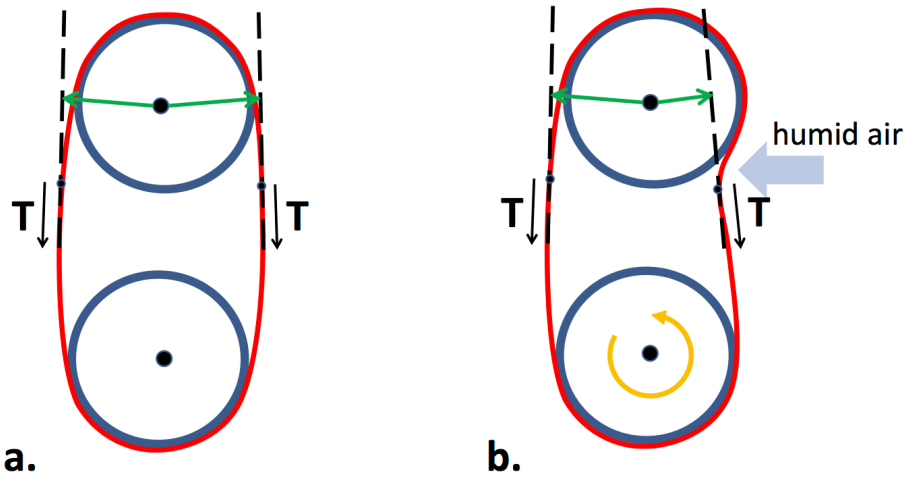

Figure 3-18 Schematic of the humidity induced bending mechanism. **a.** The configuration is symmetric about a vertical axis. The lever arms (green) are of equal length, and the net torque on the top wheel due to tension in the film is zero. **b.** Due to the humidity-induced bend, the configuration is no longer symmetric. Lever arm on the right in top wheel is shorter; net torque on top wheel due to tension in the film gives rise to CW rotation. (The humidity induced bend has been exaggerated to aid the illustration.)

As the motor rotates, the humid film dries. Key to the process is the spontaneous curvature of the film in the region near the wheel where the humidity is applied. The motor can be made to rotate faster if the ambient temperature is increased, or, equivalently, if the ambient humidity is reduced.

The energy to drive the motor comes from water vapor – from "steam". In conventional steam engines, fuel is burned to heat the water, raising the chemical potential of the water vapor due to temperature increase. Free energy is converted into work by the engine. Our steam engine exploits the difference in chemical potential of water molecules in humid and in dry air; the liquid crystal networks (LCN) belt transports the water from regions of high chemical potential to low, gaining energy in the process. The difference in chemical potential μ is given by [207]

$$\mu_2 - \mu_1 = kT \ln(\frac{\chi_2}{\chi_1})$$

Equation 3-1

Where k is Boltzmann's constant, T is the absolute temperature, and χ is the relative humidity. If the relative humidities are 30 *%* and 70 *%*, as in our experiments, the amount of energy available for work at room temperature is 2.1 *KJ/mole* of water, or approximately 100 *J/g*. The underlying mechanism is similar to that of the collagen engine of *Katchalsky* [208], which is driven by the chemical potential difference of NaCl in saline solutions and pure water. Whereas his collagen fibers contracted in the presence of salt, our LCN bends in the presence of humidity. Since our steam engine runs isothermally, it differs fundamentally from conventional steam engines in that it is not a heat engine. We call it therefore a steam engine of the second kind, and note that, consequently, its efficiency is not limited by that of Carnot cycles. It appears, from Equation 3-1, that considerable energy is available for work from reservoirs of high and low humidity; our engine provides a new method of obtaining work from a humidity difference.

3.4 Conclusion

In this chapter we show that shear transparent cellulosic freestanding films (≈ 22 μm thickness) can develop iridescence similar to that found in the petals of the tulip variety "Queen of the Night". The film's iridescence arises from the modulation of the surface into bands that periodically spread perpendicular to the shear direction. The incorporation of small quantities of nanocrystalline cellulose (NCC) rods in the precursor liquid crystalline solutions does not disturb much the optical properties of the solutions but enhance the mechanical characteristics of the films and affects their iridescence. Small bands periodicity, not affected by the presence of NCC rods, in the order of hundreds of nanometers, slightly deviated from the shear direction is also observed. The presence of NCC rods is crucial to tune and understand the film´s surface features formation. Our findings could lead to the improvement of new materials for application in soft reflective screens and devices. We report for the first time that those banded films can show iridescence, which is very similar to those found in Tulip "Queen of the Night" petals. This simple and low cost cellulosic material seems ideal to mimic the structures that can be found in plants, namely the type of gratings observed in the petals of many plant species.

The salient feature of liquid crystal elastomers and networks is the strong coupling between orientational order and mechanical strain. Orientational order can be changed by a wide variety of stimuli, including the presence of moisture. Changes in the orientation of constituents give rise to stresses and strains, which result in changes in sample shape. We have demonstrated a new type of soft motor, using a cellulose liquid crystal film, driven by a difference in humidity. The motor is simple; it relies on the moisture-induced bend of the HPC, which arises from the coupling between the

orientation order of the rigid rod-like fragments of the network and mechanical strain. Changes in orientational order are caused by the absorption of water molecules. As the engine rotates, the moist film dries in a dry air environment, and returns to its original shape, ready to perform work again when exposed to moist humidity. Since the transport of water is via directed diffusion along concentration gradients, it is expected that smaller motors will run faster. Micromotors operating on this principle, using the chemical potential of liquid water or moist air may be useful in reducing humidity or producing mechanical or electrical energy. Further studies are needed to determine the efficiency of the energy conversion process in such a steam engine of the second kind.

Chapter 4 Liquid crystal beads constrained on thin cellulosic fibers

This chapter's work description and discussion was based on the following papers:

Y. Geng, P.L. Almeida, J.L. Figueirinhas, E.M. Terentjev, M.H. Godinho, "Liquid crystal beads constrained on thin cellulosic fibers: electric field induced microrotors and N-I transition" *Soft Matter*, **8**, 3634-3640 (2012).

Y. Geng, D. Seč, P.L. Almeida, O.D. Lavrentovich, S. Žumer, M.H. Godinho "Liquid Crystal Necklaces: Cholesteric Drops Threaded by Thin Cellulose Fibers", *Soft Matter*, **9**, 7928-7933 (2013). (Cover of that issue) (Hot paper of June 2013)

4.1 Introduction

In this chapter we will describe the liquid crystal structure obtained inside of droplets threaded by a cellulose derivative micro-fibers. We will present nematic and chiral nematic liquid crystal droplets and we will characterize the evolution of these structures with temperature and applied electric field. Liquid crystal drops or droplets are defined as spherical or ellipsoidal shape volumes of liquid crystal. Liquid crystal drops are usually dispersed in polymer matrix or other liquid, but they can also be free suspended in the air. Liquid crystal drops can present many interesting structures because of the confinement, namely the confinement shape and surface anchoring conditions.

The two basic features of liquid crystal drops are (1) the ordered inner structure of the dispersed particles and (2) the small scale of confinement in which bulk and surface interactions are in direct competition, make liquid crystalline dispersions distinctive and more complex than their isotropic counterparts or continuous liquid crystalline media.[209] The droplets contain lots of stable and unstable topological defects with rather unusual structures, which decide the properties of the droplets, such as electric-optical properties. So the studying of liquid droplets with different liquid crystal types, different confinements, and also different anchoring conditions are very important.

Because of the scientific and the application interests, liquid crystal drops have been studied since the birth of liquid crystal. Lehmann started to study the liquid drops dispersed in an isotropic fluid since 1890s even before introduction of the term of "Liquid Crystal".[209] From the 1970s attentions started to focus on liquid crystal drops, for example *Candau et al.* studied the magnetic field effects in nematic and cholesteric liquid crystal droplets suspended in isotropic liquid.[210] It was not until 1980s that there came a true revival of interest in liquid crystalline droplets. The invention of polymer dispersed liquid crystal (PDLC) opened the new window for the studying of liquid crystal droplets.[175,209,211]

In this chapter's introduction, a brief overview will be given about liquid crystal drops and some review of the state of the art concerning liquid crystal drops, focusing on the defects and the structure transitions under different boundary conditions. The confinement of liquid crystals to spherical volumes can lead to a variety of complicated director fields configuration,[112,212] which depend on the liquid crystal properties such as the elastic properties, anchoring of the director at the drop surface, the size of the droplet, the external fields, and also the temperature. Among all the factors, the anchoring condition of the molecules at the surface is the first aspect to classify the droplet type,[213,214] because it fixed the topological constrains on the liquid crystal and basically decides the structure of the droplets. As in other studies,[213] we consider strong anchoring conditions in this part, where the tilt angle is fixed to some value and also the droplet is large enough for the surface constrain to fulfill. The tilt angles, *0*

and $\pi/2$ are the most common, corresponding to parallel or tangential and homeotropic anchoring conditions respectively. For the parallel or tangential anchoring conditions, the director is parallel to the surface, and for the homeotropic anchoring the director is perpendicular to the surface.

For the droplet dispersed in other matrix, the free energy is defined by:

$$F = F_v + F_{vs}$$

Equation 4-1

Where F_v is the free energy form the bulk liquid crystal and F_{vs} is from the surface confinement. This equation can also be applied to a normal fluid.

The elastic free energy density of liquid crystal is given by *Frank-Oseen* equation[213] as shown in Equation 1-3.

From Equation 1-3 we can easily get that the changing of the elastic constants leads to different free energy and thus different structures.[215,112]

There are two kinds of point defects in a droplet. One is called boojum, which in fact is a two-dimensional defect located on the surface of the droplet despite the distortion in the bulk, [215] and the other is hedgehog, which is a 3-dimensional defect usually located in the center of the drops. The point defect transforms into other defects usually under the changing of the anchoring condition or under external field, for example to disclination line defects, which will be discussed as an example in nematic liquid crystal in the later part.[175,216-220,221-224]

As shown in Figure 4-1, for nematic liquid crystal with tangential boundary conditions, when $K_1 < K_3$, the bipolar condition is typically observed. This drop has two $s = 1$ point defect on the surface. In order to maximize their separation, they are located on the two poles as shown in Figure 4-1 a. In this configuration the splay distortion plays the main role comparing to bending. When twist is introduce into the configuration of a, the twisted bipolar boojum configuration is still formed with two boojums located at the different poles (Figure 4-1 *b*). When the bending distortion plays the main role structure in Figure 4-1 *c* can be for formed. In this structure, director field is organized in concentric circles with a $s = +1$ disclination line that passes through the center of the drop.

For nematic liquid crystals, when the anchoring condition is homeotropic, the configuration is normally observed in Figure 4-1 *d* - *f*. It is a pure splay structure with a radial hedgehog with a topological charge $Q = +1$ located at the center of the droplet, as schematically shown in Figure 4-1 *d*. A variant of this structure results from incorporating twist distortions to form a twisted radial drop, as schematically shown in Figure 4-1 *e*. In this structure, the resultant configuration can be seen as a

combination of a hyperbolic hedgehog at the center of the drop. For nematics favouring bend over splay distortions, the director can organize around a defect ring located on the surface of a drop along one of its great circles, as schematically shown in Figure 4-1 *f*.

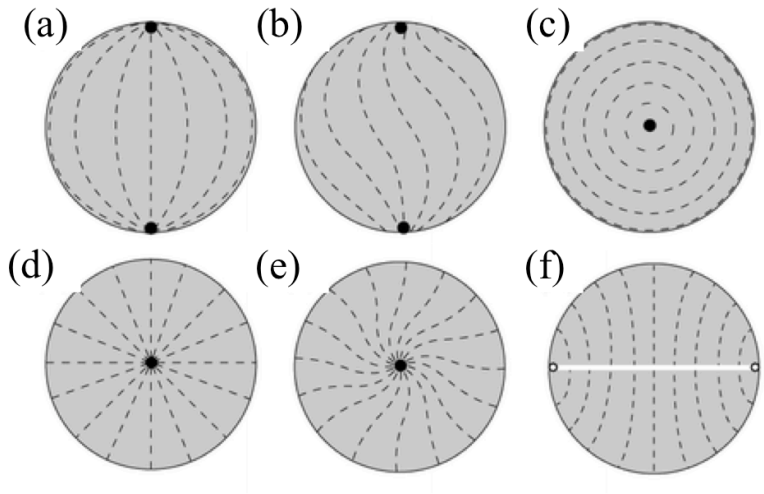

Figure 4-1 Examples of the nematic drops with different structures. (**a-c**) with tangential anchoring condition and (**d-f**) with homeotropic boundary condition. **a.** The bipolar drops with two s=1 splay-type boojums located on the surface. **b.** With a in plane rotation of the director from the axis of the two boojums from a, the twisted bipolar drops can be formed. **c.** When the bending distortion plays the main role the concentric drop can form. In this situation, director field is organized in concentric circles with an s = +1 disclination line that passes through the center of the drop. **d.** The radial drop, with one radial hedgehog at the center of the sphere, is the structure usually observed when the anchoring is perpendicular. **e.** The twisted version of the radial drop has also been observed. **f.** The axial drop, which appears when bend distortions are energetically favoured, is characterized by a Q = +1 equatorial disclination ring on the surface of the drop. [213]

More recently, confined chiral nematic liquid crystal systems also have become interesting because of their very unusual structures and defects.

Understanding chiral nematic structures is also of practical importance. Cholesteric liquid crystals favour twisting of their average orientation (the nematic director) in planes. But if they are frustrated such as being enclosed in the droplet, the more complex disclinations can be formed. There are three kinds of disclinations in cholesteric liquid droplets as shown in Figure 4-2. Two main parameters control the director configuration in a cholesteric drop: (a) the boundary conditions and (b) the twisting power, qR, with R the radius of the drop and $q=1/P$.

Three structures are found in cholesteric droplets with planar degenerate anchoring:[225] (i) radial spherical structure (RSS), (ii) diametrical spherical structure (DSS), and (iii) planar bipolar structure (PBS). Zumer *et al.* systematically studied the structures as shown in Figure 4-3, Figure 4-4 and Figure 4-5, using a continuum mean field landau-de Genns free energy approach. In their study they use the tensorial order parameter Q_{ij} to construct the total free energy and minimized the total energy to get the order distribution.[226] They got the fantastic structures.[227]

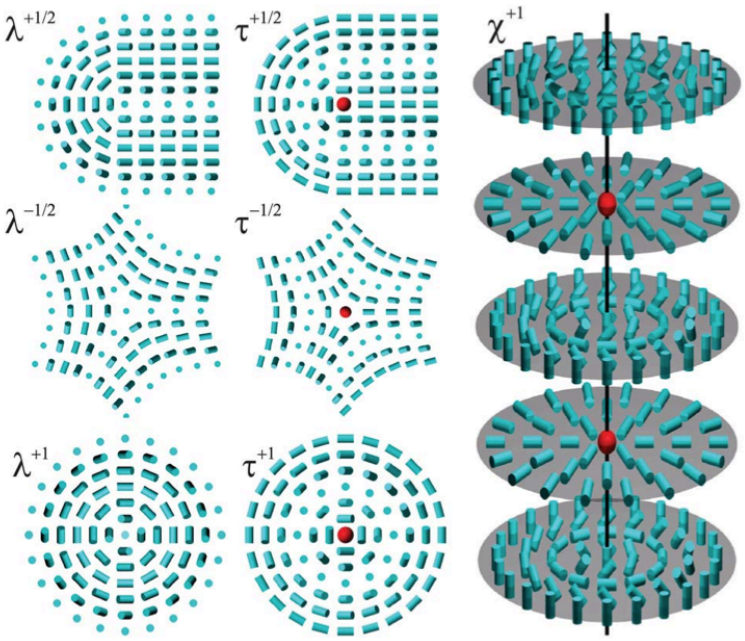

Figure 4-2 Schemes of the cholesteric disclination line λ^m, τ^m and χ^m with various winding number of m. The director is shown with blue cylinders while red spheres are the lower ordering regions. The core of the χ disclination is draw as black line. [227]

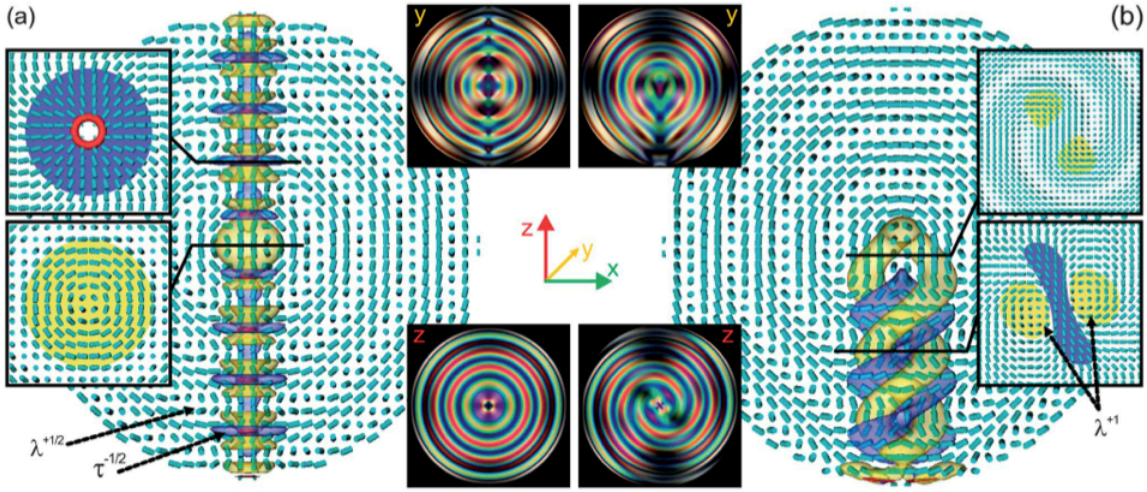

Figure 4-3 **a**. Numerically calculated diametric spherical structure (DSS), and **b.** radial spherical structure (RSS) in chiral nematic droplets. [227]

The diametric spherical structure (DSS) is the most symmetric structure in cholesteric droplet degenerate planar surface anchoring as shown in Figure 4-3 *a*. It exhibits the cylindrical symmetry with its symmetric axis along the axis of the cylinder *z* direction. The director field forms curved structure normal to the radius. The radial spherical structure (RSS) is most commonly observed structure (Figure 4-3 *b*), with a monopole point defect connected with a distorted double twist line defect. The bipolar structure (BS,), shown in Figure 4-4 *a*, is also cylindrically symmetric and

characterized by only two surface boojum defects diametrically located at the surface. The planar bipolar structure (PBS, *b*) is similar to BS but deformed by the strong planar anchoring condition. The *Lyre* and *Yeti* structures are highly meta-stable state as shown in Figure 4-5. Those structures mentioned above can transform with each other when the anchoring condition is changed as well as the twisting power of the droplets.

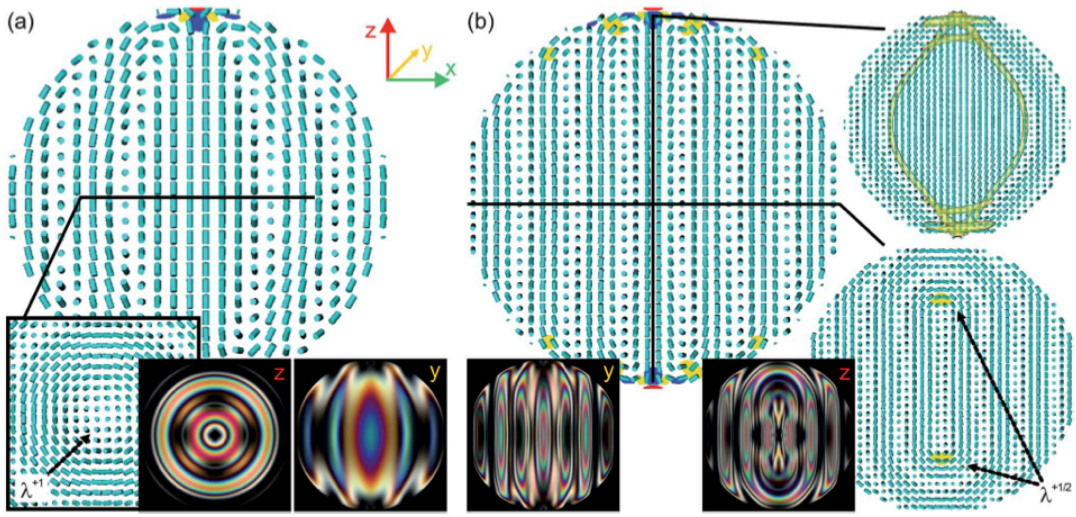

Figure 4-4 **a.** Bipolar structure. **b.** Planar bipolar structure (PBS). The director field in xz plane is mostly in layers as can be also seen in polarization micrographs. This structure has three twofold symmetry axes (x, y, and z). Note blue and yellow regions of the splay-bend parameter and the differences between the two structures in polarization micrographs (lost symmetry in the z plane). [227]

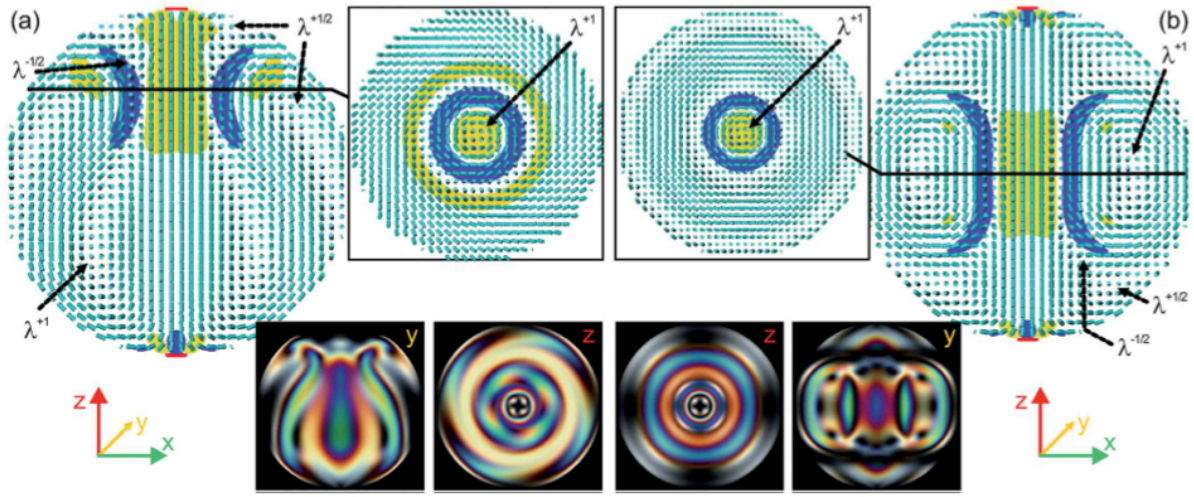

Figure 4-5 **a**. Lyre structure (LS, N=4). Diametrical line with $\lambda^{-\frac{1}{2}}$, $\lambda^{+\frac{1}{2}}$ and λ^{1}, cholesteric disclination rings. The structure is only rotational symmetric around the z axis. **b**. Yeti structure (YS, N=5). Note also here $\lambda^{-\frac{1}{2}}$, $\lambda^{+\frac{1}{2}}$ and λ^{1} cholesteric disclination rings. Apart from the cylindrical rotational symmetry (z axis), this structure has also two-fold symmetry axes in the xy plane. Blue and yellow regions show the splay-bend parameter. [227]

For cholesteric liquid crystal drops, different anchoring conditions also lead to different structures in the nematic case, but different twisting power also can changes the structures. For tangential anchoring and low twisting power, $qR < 1$, the resultant drop configuration is twisted bipolar in Figure 4-6 *a*. Study from *Xu et al*. show that the twist angle linearly decays to zero from the surface. For $qR > 1$, the most widely observed configuration is the Frank-Pryce structure, which consists of a hedgehog with an attached $s = +2$ defect line of length R as shown in Figure 4-6 *e*. The line can be understood by considering the simplified view of a cholesteric liquid crystal as a stacking of nematic layers that are twisted one with respect to the other. The line results from the concentric stacking of these spherical nematic layers inside the drop, with each layer being progressively twisted one with respect to the other. Since, by the Poincare-Hopf theorem, the total topological charge must be $+2$ in each of these layers, the defect line can be thought of as a linear stacking of $s = +2$ point defects in each cholesteric layer.[213] Changing the anchoring condition and the twisting power, more interesting structure can be observed, for example in Figure 4-6.

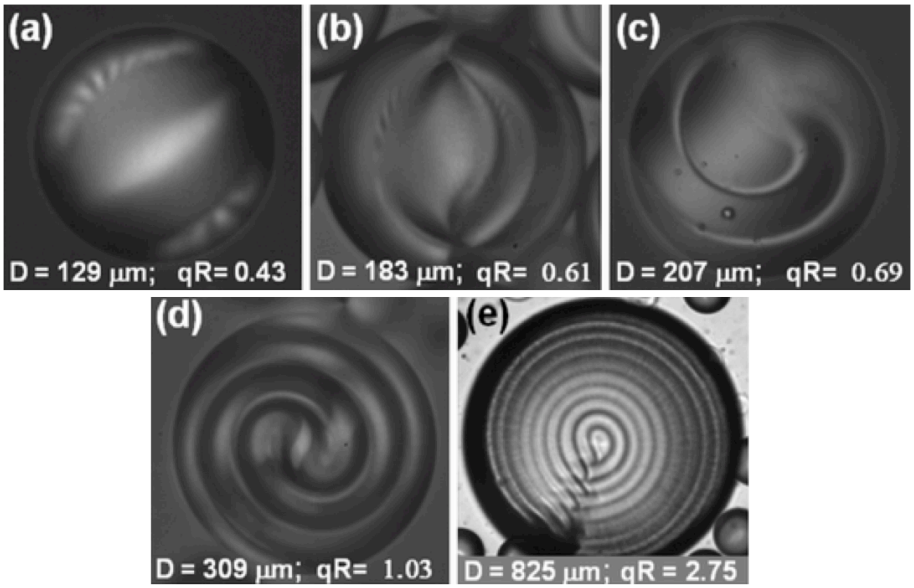

Figure 4-6 Cholesteric droplets, (**a-d**) with different twist power qR, with R as the radius of the droplet and q the inverse of the pitch, under homeotropic anchoring conditions, **e** droplet with planar boundary conditions. **a**. lower twisting power bipolar structure can be formed. **b-d**. when the twisting power increase the structures changes from bipolar to the structure of **d**.[213]

From above discussion, different anchoring conditions and also different twisting powering lead to different defects and droplets structures. So it is easy to understand that by changing the boundary condition or the twisting power of the droplets it is possible to induce the topological structure change dramatically but continually even in the same droplet and the process can be easily followed dynamically. For example in nematic liquid crystal droplets, in Figure 4-7, change the anchoring condition from tangential to homeotropic the two characteristic boojums of the bipolar drop disappear, while a defect ring of charge $Q = +1$ concomitantly forms. The ring appears in a plane perpendicular

to the original boojums axis to form a transient axial drop, as shown in *b*. By doing so, the director in the bulk does not distort appreciably; it remains very much oriented along the original boojums axis. The defect ring subsequently shrinks into a half radial hedgehog, as shown in *c* and *d*, which eventually migrates to the center of the drop to form a radial drop as shown in *e*.

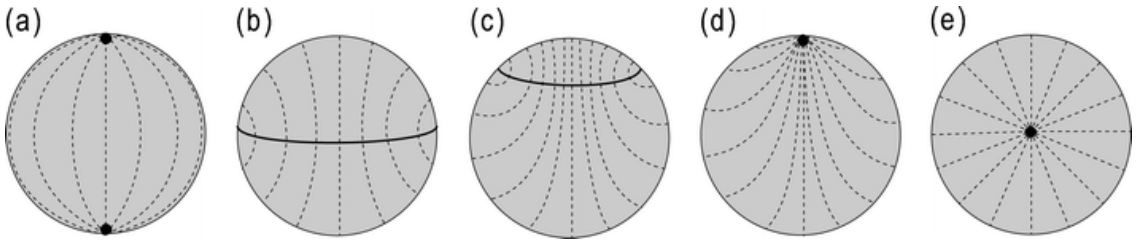

Figure 4-7 Topological transition with the boundary condition changing from tangential or planar to homeotropic. The schematics show a cross-section of the drop along the plane containing the two initial boojums and center of the sphere. The solid line refers to the defect line and the dotted line refers to the director field inside the droplet. From **a**. to **e.** the anchoring condition is changing from planar to homeotropic. [213]

When the anchoring condition is changing from homeotropic to planar the transformation is different, firstly there are two points defects - boojums - are generated locating at the poles and then the hedgehog moves to near one of the boojums and changes to the ring disclination line and moves to the center and then finished left two boojums located at the poles.[215]

Transformations between different defect structures can also be induced by electric and magnetic fields, as in their presence the free energy density of the system changes by: [213]

$$f_{field} = -\frac{1}{2}\varepsilon_0 \Delta\varepsilon(\vec{E}\cdot\hat{n})^2 - \frac{1}{2}\frac{\Delta\chi}{\mu_0}(\vec{B}\cdot\hat{n})^2$$

Equation 4-2

Where ε_0 is the dielectric constant of free space, $\Delta\varepsilon$ the dielectric anisotropy, $\boldsymbol{E}$ the electric field, $\Delta\chi$ the anisotropy in the magnetic susceptibility, and B the magnetic field. The application of external electric and magnetic fields thus induces changes in the nematic orientation, which in many cases leads to changes in the type of structure. We note that there are other forms of liquid crystal-electric field coupling if the molecules have a permanent dipole moment. In addition, shape polarity can give rise to flexoelectricity: development of an electric polarization as a result of director field distortions.

For example for the radial droplet shown in Figure 4-8, formed by a nematic with $\Delta\varepsilon > 0$, and if we apply an electric field with increasing electric field intensity, the radial configuration slightly bends to progressively align n with E, as shown in Figure 4-8 *b*, until a π wall eventually forms in the plane perpendicular to the applied field, as shown in Figure 4-8 *c*. This wall divides the drop into two hemispheres, with a π rotation of n as the wall is crossed from one hemisphere to the other. In each

hemisphere, the director is essentially aligned with E and the drop still contains the original hedgehog of the initial radial drop. With increasing E, the width of the π wall decreases until it eventually becomes unstable. This happens at a critical electric field E_c, where both the hedgehog and the π wall are replaced by the equatorial defect ring, characteristic of the axial drop, shown in Figure 4-8 *d*. The application of an external field to a radial drop thus results in the formation of an axial structure. With different frequency of electric field, the processes are totally different. With high frequency of the electric field, the ring formed in the center and then moved to the surface, but the order is the reverse with low frequency. The point moves to the surface first and then changes to the ring defect with lower frequency. And the radius also found to be an important effect factor for the critical value of the transition.[228]

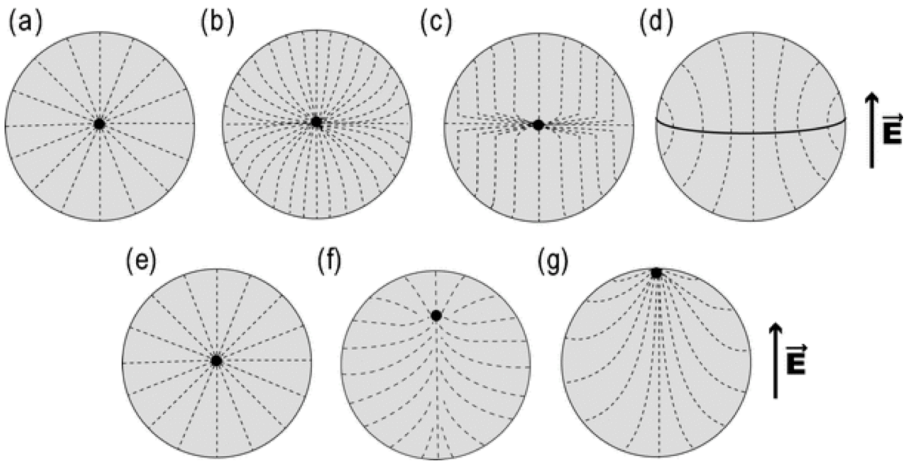

Figure 4-8 Topological transformation induced by the electric field (at low frequency) in a radial drop. For positive dielectric anisotropy the nematic, the transition normally follows the **a**. to **d.** For negative dielectric nematic liquid crystals shown in **e - g.** [213 228]

In this chapter, a characterization of the defects structure observed in a droplet threaded on a micro-fiber during the application of an electric field will be presented. We will visualize the appearance of a soliton-like particle. In mathematics and physics, a soliton is a self-reinforcing solitary wave (a wave packet or pulse) that maintains its shape while it travels at constant speed. Soliton-like particles are caused by a cancellation of nonlinear and dispersive effects in the medium. It was also shown that in uniaxial nematic, a soliton-like particle can be formed if a distorted director configuration exists in a region of finite size and outside of which the director field is uniform. Solitons can appear in liquid crystals by the action of an external field which provides the nonlinear term in the equation of motion needed to describe the molecular orientation, because of its nonlinearity and nonlocal in time and space.[229,230,231-240] For our nematic liquid crystal system, the soliton-like particle amounts to an inhomogeneous of distribution of the field of the director localized in a region of finite dimensions.[241,242]

Skyrme et al. studied the source of the soliton-like particles using classical theory in super fluid^3 He-B[243], and the spinning soliton-like particles are theoretically confirmed and the properties are studied by *Williams at al.*[244] They found that the free energy is proportional to the size of the soliton-like particle and the particles are unstable. Studying also show that when the particle-like soliton decrease its dimension and subsequently disappear on scales smaller than the coherence length.[244] In fact the decrease in dimension of the soliton entail an increase in the elastic energy density but decrease the total energy.[242]

Spherical liquid crystal (LC) droplets, suspended in a supporting polymer matrix, are now used in a number of electro-optical applications such as privacy windows and optical switches. These systems can reversibly transform between the transparent and the opaque scattering states in response to an external electric field. The performance depends on the internal director ordering within the nematic drops, and different nematic configurations would result in clearly diverse responses to the externally applied fields.[245]

Therefore, characteristic parameters of droplets such as shape, surface anchoring and nature of the topological defects play a significant role in the electro-optic response of the device, and it has been widely experimental and theoretically studied by *Zumer*[246,175] and *Lavrentovich et al*[247]. In flexible plastic displays based on encapsulated nematic liquid crystals, these constraints can similarly play a role in the performance of the device.[248]

For example, more recently, drops of liquid crystals were used as tunable optical microresonators.[249] Fluorescently labelled nematic liquid crystal droplet with the diameter of 10 μm dispersed in a polymer matrix with the homeotropic bounder condition. The hedgehog point defect located at the center of the droplet. When the light is introduced into the resonator, because of the total internal reflection the beam circles in the droplet and comes out from the original point with the shifted frequency that depends on the optical path and also the dope molecules. When the director configuration is changed by the external electric field, the optical path decreased and the frequency decreased. Three-dimensional tunable lasing in dye-doped, cholesteric liquid-crystal (CLC) microdroplets embedded in an isotropic carrier fluid also has been reported. These droplets were spontaneously self-assembled and, due to the chirality of the CLC, a strong modulation of the refractive index was obtained in the radial direction, thus forming a radial Bragg (onion) resonator, by changing the temperature to change the pitch in order to change the laser frequency.[250] These findings open new paths in the development of optical and photonic microdevices, surface-sensitive sensors, tunable microcavities and soft photonic circuits.[251] Polymer dispersions of spherical (or ellipsoidal) nematic liquid crystal droplets are widely used and studied.[245] Light scattering devices can also be realized from liquid crystals supported by the mats of nano and micro-fibers. The LC material is inserted by capillarity in this type of cells after the fiber mat assembling.[252] As a consequence of the

improved interaction of the nematic liquid crystal with the microfibers, enhanced optical characteristics (*i. e.,* increase transparency in the ON state and a marked decrease in the operating voltage) were found for this kind of sensors.

All the interesting behavior observed in the droplets and shells of liquid crystals, results from the curvature of the closed spherical surfaces.[253] However, even more complicated defect configurations are expected when the liquid crystal is encapsulated into regions with more complex topologies, *e. g.,* toroidal drops,[254] which remain largely unexplored from the experimental point of view. In fact, generating fluid objects with non-minimal surface shapes, such as a torus, is complicated and still remains a challenge. Despite the difficulty, this can be achieved by using external forces. However, the majority of the toroidal shapes generated by using external forces is unstable and always converts into a topologically spherical fluid volume once the external force disappears.[255]

The majority of the studies about these matters focus on the studying of droplets dispersed in matrices such as polymers or liquids, but studies focused on liquid crystal droplet free suspended in air do not exist to our knowledge. Free suspended droplet in air has very particular anchoring conditions and is very sensitive to the surround environmental changing. Another confinement is imposed by inserting an electrospun micro-fiber through one axis of the droplet. By doing this we were able to observe and characterize very interesting structures and phenomena.

In this chapter we present the response and dynamics of liquid crystal droplets with stable toroidal topology to temperature and to an applied AC electric field. The hybrid drop shells were obtained by dispersing the nematic and cholesteric liquid crystal on air suspended thin fibers, and show that the response mechanism of the drops is outside of the current understanding of liquid crystal drops.[256]

4.2 Experimental

Concentrated cholesteric solution (60 *wt %*) of hydroxypropylcellulose (HPC) as introduced in chapter 1 (1.1.3 and 1.2.3). (*Aldrich*, $\overline{M}_w$ 100.000 *g mol*$^{-1}$) in dimethylacetamide (DMac) (*Riedel-de Haen*, *99 %*) was made and was waited for 3 weeks before using. The viscous iridescent solution in the nematic chiral phase was poured into a 1 *ml* syringe (diameter 4.5 *mm*) fitted with a 27-gauge needle (diameter 0.2 *mm*) which was then placed on the infusion syringe pump (*KDS100*) to control the polymer solution feed rate. A conducting ring, 15 *cm* in diameter, was held coaxially with the needle tip at its center, and electrically connected to it. The needle plus ring were directly connected to the positive output of a high voltage supply (*Glassman EL 30 kV*). After applying the electric potential

between the metallic syringe-tip and the plate, the polymeric solution was continuously fed to the syringe-tip at a constant flow rate of 0.04 $ml\ h^{-1}$, and accelerated by the ensuing electric field towards a collector. The optimized operating conditions for the continuous drawing of cellulose derivative fibers were a voltage of 15 kV for a distance between the nozzle and the collector, l = 15 cm. In general, fibers get thinner at higher accelerating voltages; however, several other parameters (such as the solution viscosity, needle diameter and the distance to target) also contribute to the fiber shape and dimensions.[155] In order to obtain uniaxially aligned fiber arrays, a specially designed fiber collector made of two parallel aluminium strips, between which another high voltage power supplier was added with the output of 3 kV, stuck together by two conductive aluminium wires was used. Each aluminium strip had a length of 2 cm and a width of 0.2 cm. The distance between the metallic stripes was 1 cm (Figure 1-24 and Figure 1-25) After electrospinning, the HPC fiber arrays, deposited across the aluminium strips form suspended networks. The fibers were then carefully dried in a vacuum, at room temperature, for 72 h before further characterization.

To align the fibers during the electrospinning, normally there are two methods. One is to use the rotating drum or frame, which was demonstrated to be a good way to produce fibers with good alignment. Usually high rotation speed was necessary to get good aligned fibers especially when the solution flow is high. At the same time the high rotation speed of the collectors always generates strong airflow that disrupts the deposition process of the fiber and decrease the alignment.
The other way is to use parallel metal electrodes as the fiber collectors. When one end of the charged fiber formed by the stretching of the electric field touches one of the electrodes, the charge moves to the electrodes collector. Before the charge goes to the ground, the other end of the fiber is propelled to the other electrode and the aligned fibers mat is deposited on the parallel electrodes collectors with time. Usually the charge is very tiny and disappears (the electrodes are grounded) very fast when one end of the fiber touches the electrode. Even though this way is efficient for thin, light and relatively short fibers, for relatively long, thick and heavy fibers, the effect is not so significant anymore and the alignment deteriorates.

In our study, we used a modified apparatus to produce the electrospun fibers. As we can see from Figure 1-24, before modification (left part), the two electrodes are in the same electrical potential line because the distance from them to the nozzle is the same. So one way is to unground one of the electrodes and move it a little bit near to the nozzle. Then the force gets much bigger and will not be zero all the time. According to our experience, usually the second way is still not efficient enough to align the fibers very well. So another high voltage power supplier was added between the electrodes to increase the force to align the fibers. The output was chosen to be 3 kV according to our experimental requirements.

To perform electrospinning, another issue that had to be solved is how to remove the aligned fibers from the electrodes without destroying the fibers as well as the alignment. To solve this problem, we used a homemade thin plastic frames attached to the electrodes (Figure 1-24). The plastic thin frame should be un-conductive and as thin as possible but strong enough to protect the fibers during the removal of the electrodes after deposition.

The nematic liquid crystal 4-n-pentyl-4-cyanobiphenyl (5CB) (*Merck K15*) used exhibits a nematic phase in the temperature range of 18 *ºC* to 33.6 *ºC*.

To produce cholesteric droplets, we used the nematic liquid crystal *4'-n-pentyl-4-cyanobiphenyl* (5CB), the chiral nematic compound *(S)-4'-(3-methylpentyl)-4-cyanobiphenyl* (5CB*), which presents a chemical structure very similar to 5CB, and a 10 *wt %* mixture of 5CB* in 5CB (5CB*Mix). The 10 *wt %* concentration was chosen to produce a helical pitch *P* detectable by POM. 5CB* presents a N* phase between -14 ^{o}C and -22 ^{o}C and a helical pitch of about 0.3 μm, and a smectic A phase is reported for temperatures below -22 ^{o}C[257]. The LC chiral mixture, 5CB* Mix, presents a I-N* phase transition at 28.3 ^{o}C and a pitch value of 7.1 μm measured by optical microscopy, at room temperature (~19 ^{o}C). The 5CB* compound was synthesized according to the procedure described in detail in reference[258].

Nematic micro-liquid crystal droplets were generated by an *Air Project* ultrasonic humidifier (*Italy ARTSANA Group*) and deposited on the electrospun fibers at room temperature (23 ºC).

To generate stable planar anchoring at the cholesteric droplet surface we mixed 5CB* Mix with glycerol and used ultrasound excitation in order to emulsify the system into small droplets. In order to obtain well-dispersed and symmetrical droplets confined on the fibers, the samples were heated to 80 ^{o}C for 5 minutes. The droplets are then carefully collected by a metallic wire (0.1 *mm*) at room temperature (~19 °*C*) to suspended fibers assembled by electrospinning. The ratio of the liquid crystal to glycerol is around 20 *wt %,* so the droplets were still surrounded by the glycerol to keep the planar anchoring condition at the liquid-oil interface when they were moved onto the fibers.

Optical microphotographs were taken using a transmission mode microscope, Olympus BH, equipped with polarisers, a camera and a heating/cooling stage (Mettler, FP90). The fibers were characterized by Scanning Electronic Microscopy (SEM) using a SEM DSM962 model from Zeiss. Gold was deposited on the samples by sputtering in an Ar atmosphere, using a 20 *mA* current, for 30 seconds at a deposition rate of 3 $Å s^{-1}$. Images were obtained for an acceleration voltage of 5 *kV*. Fiber diameters and lengths were determined using *Image J* image processing software (version 1.*40e*). Blender, version 2.*57b*, was used to obtain 3D drawings. Photographs and movies were taken with a Canon EOS 550D coupled to the microscope through a LM-Scope adapter. The obtained images do not have

a very high quality due to the complexity of the assembly on the microscope that allowed us to maintain free suspended droplets on a heating plate to perform the studies with different temperatures.

4.3 Results and discussion

4.3.1 Free nematic liquid crystal droplets confined on fibers

4.3.1.1 Toroidal topology in nematic liquid crystal droplets

As we can see from Figure 4-9, well aligned fibers were produced. Figure 4-10 shows the electrospinning fibers from different scale, which were used to perform the next studies.

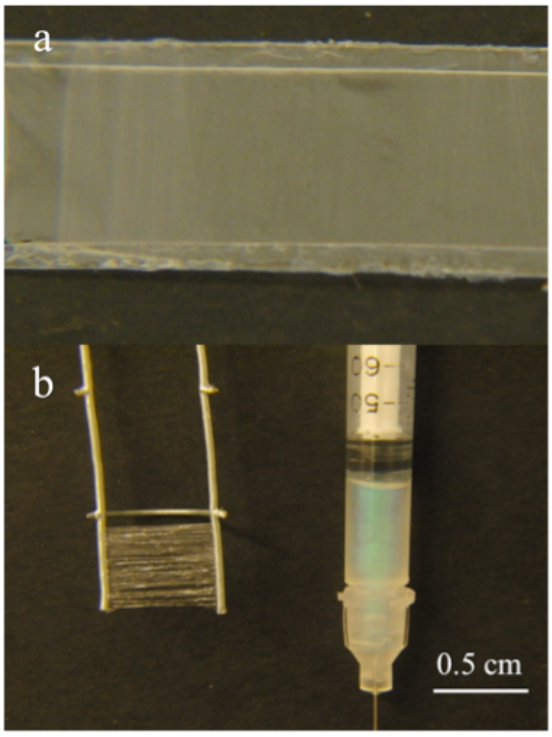

Figure 4-9 Photographs of **a**. aligned fibers collected on parallel electrodes and **b**. another set of fibers collected between parallel electrods and also the anisotropic solution used to produce them.

To generate the toroidal topology of liquid crystal droplets we used ultrasound excitation in order to emulsify the 5CB liquid crystal into small droplets, which are then collected on suspended fibers assembled by electrospinning (Figure 4-11 *a*).

The electrospun fibers (Figure 4-11 *b*), characterized by SEM (Figure 4-11 *c*), have diameters that vary between 1 and 2 μm and are obtained from cellulosic solutions which enforce tangential boundary conditions for the nematic liquid crystal aligning along the fiber axis in our case. The resulting system of liquid crystal droplets, with diameters less than 50 μm, suspended around fibers stretched in air was placed between two transparent glass plates coated with conducting ITO layers as electrodes, separated by 1 mm distance, as shown schematically in Figure 4-11. The assembly containing air, the fibers and the threaded droplets were observed under a polarizing microscope by using: crossed polarizers, a 530 *nm* quarter retardation plate inserted between cross-polarizers at a 45 º orientation and a bright field optical microscope (three micro-suspended droplets are shown, as an example, in a 1 μm diameter fiber between cross-polarizers in Figure 4-11). To study the electric switching of the constrained drops we applied an electrical potential difference (AC 50 Hz) across the cell.

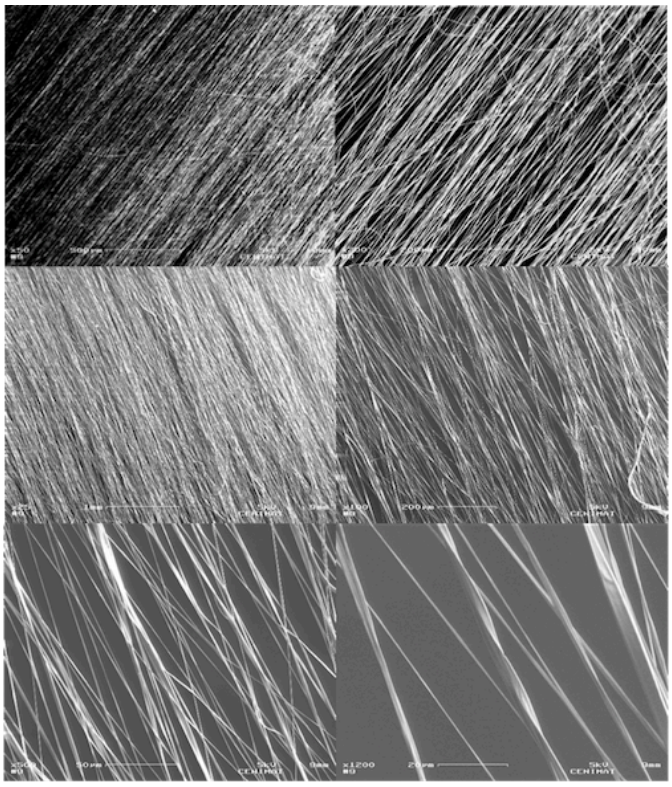

Figure 4-10 SEM images of aligned fibers with different magnifications.

Note that the characteristic ratio *WR/K*, for the planar anchoring energy *W* and Frank elastic constant *K* of 5CB, usually exceeds 1 for droplet sizes *R* of a few microns, and so the regime of *WR/K* > 1 is

that of topological defects. A typical example of two, 30 μm and 10 μm diameter, liquid crystal droplets suspended on a 1 μm diameter fiber is given in Figure 4-11 *d*. This picture was taken between crossed polarizers in order to visualize the textures inside the droplets supported around the fiber (indicated by arrows in Figure 4-11 *d*). The image shows a ring defect at the center of both air-supported drops.

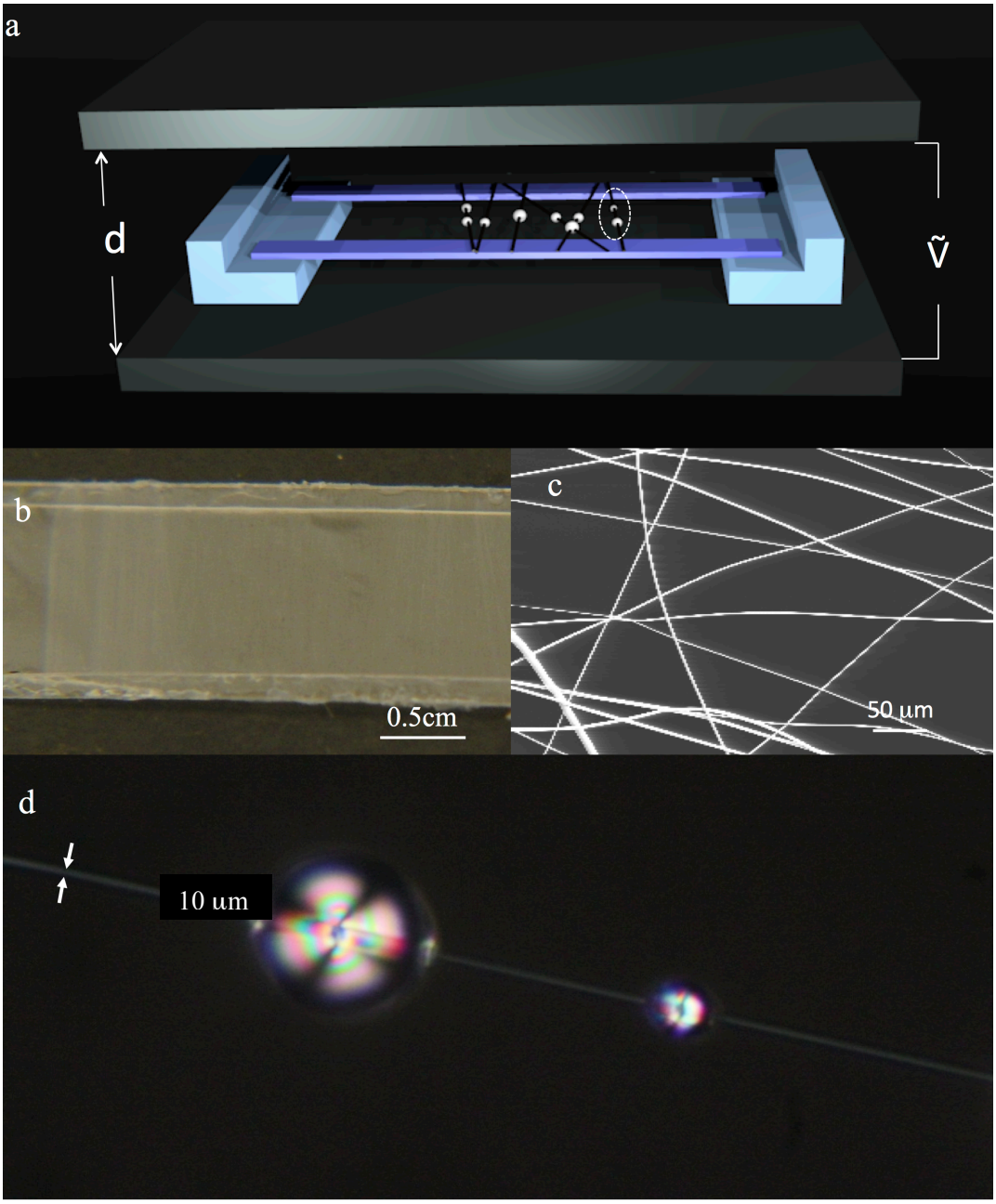

Figure 4-11 **a.** Schematics of the experimental setup. The electrospinning target used to produce air suspended fibers with numerous tiny (diameter less than 100 μm) 5CB liquid crystal droplets generated by ultrasounds was sandwiched between two transparent ITO electrodes separated by a distance, d=1 *mm*, by wire spacers. Insets (**b** and **c**) represent suspended fibers in different scales; **c** a SEM picture. **d** Cross-polarized image corresponds to nematic droplets constrained on a thin fiber (1.0 μm diameter), suspended in the air, as schematically represented in *a*.

To investigate the origin of this ring defect, droplets supported in different fiber geometries were observed using the method described above. The air-suspended droplet (diameter 40 *μm*) straddling between three fibers is shown in Figure 4-11 and Figure 4-12 *a* – *c* along with the schematics of the 3D (Figure 4-12 *d*) and top-view director field configuration (Figure 4-12 *e*).[259,260] The molecular anchoring at the 5CB/air interface of the droplet is known to be homeotropic. [160] In fact, we see that the birefringence is smaller in the direction perpendicular to the plate optic axis, which implies the formation of a radial hedgehog at the center of the sphere as shown in the 3D representation.

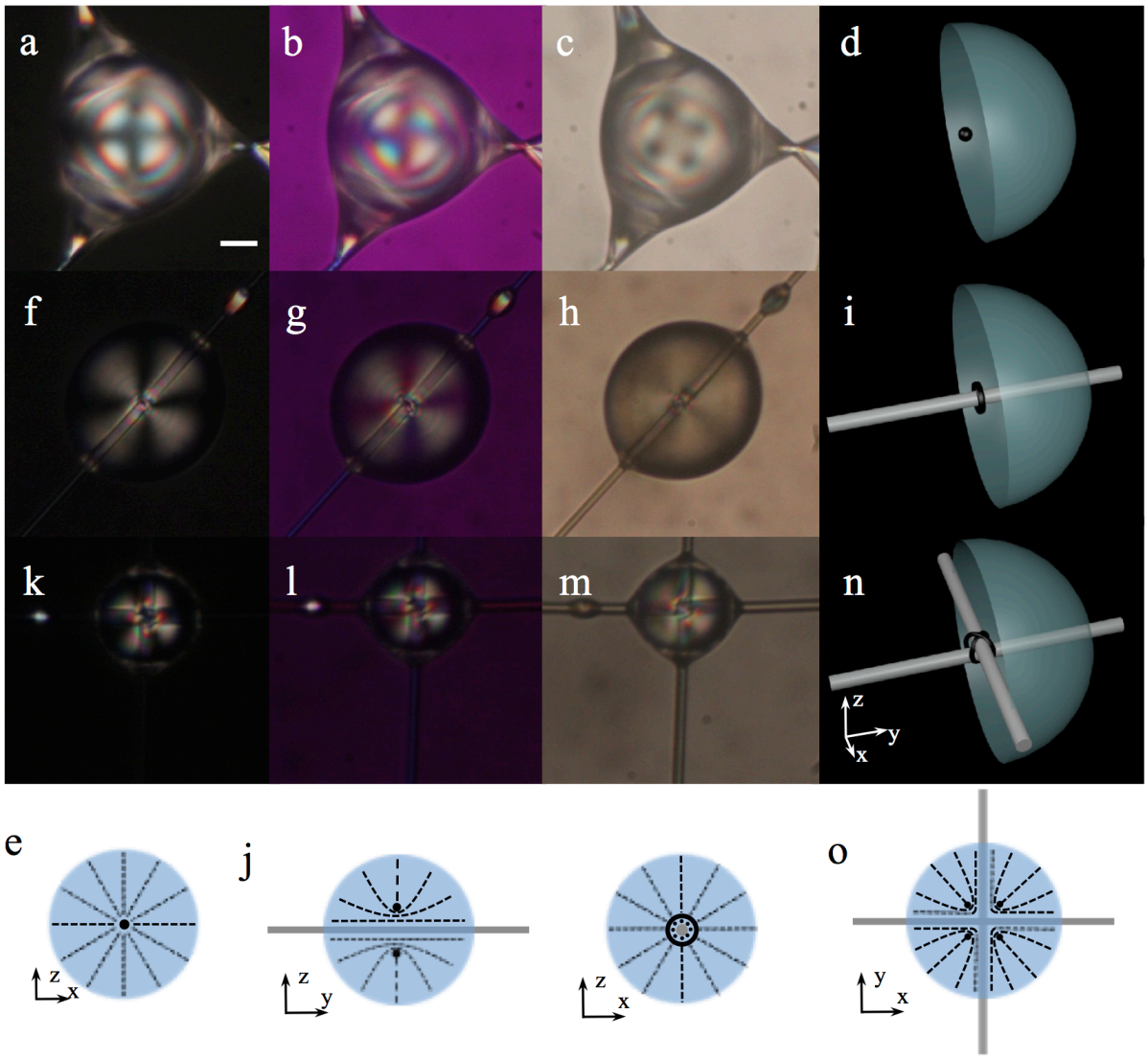

Figure 4-12 Cross-polarized (**a**, **f** and **k**), 530 *nm* retardation plate (**b**, **g** and **l**) and bright field images (**c**, **h** and **m**) of air floating nematic shells constrained in different fiber geometries, at room temperature. (**a-e**) hold up in-between three fibers; (**f-j**) around a fiber and (**k-o**) around two 90º cross fibers. Schematic of the director field configuration (**e**, **j** and **o**) along with 3D (**d**, **i** and **n**) representation allows the visualization of the transformation of the point defect, to a ring defect and to two cross ring lines defects depending on the fibers constrained geometries.

The top view director schematics, Figure 4-12 *e*, indicates the formation of a radial splay-type defect. Figure 4-12 *f – j* show a typical liquid crystal droplet supported by a single 1 μm fiber, which goes through the center of the LC drop generating a stable shape of toroidal topology. Figure 4-12 *k – o* show a droplet straddling between two fibers, which produces a much more complex topology of a ‘‘pretzel,’’ or double-torus, with the Euler characteristic equal to *-2* (compared to *+2* for the sphere and zero for the simple torus).[261, 159]

It was found that the planar alignment of 5CB molecules can be induced by HPC films produced from high polymer concentration solutions, high coating speeds, and thin coating thicknesses.[160] The homogeneous surface alignment of 5CB was attributed to the flow-induced orientation of cellulosic main chain molecules fixed in the vicinity of the film surface.[159] The HPC fibers produced by electrospinning used in this work fulfill all the requirements needed to align the 5CB molecules parallel to their surfaces and along the main axis of the fiber. In fact, we use high-concentration liquid crystalline HPC / DMac precursor solutions and the electrospinning technique ensures high speed and thin diameter fiber production, which generates flow-induced orientation of cellulosic molecules at the fibers surface.

The nematic LC droplet shown in Figure 4-11 *d* and Figure 4-12 *f – h* should have the director tangential near the fiber surface and homeotropic at the air interface, making a hybrid shell. In fact, the alignment of 5CB molecules on a flat HPC shear-aligned film surface was determined by observation of a droplet of liquid crystals deposited on the film with a polarizing microscope. The 5CB molecules were found to uniformly align parallel to the alignment surface due to the gradual director change, from the parallel alignment at the aligned polymer surface to the perpendicular alignment at the air interface. This director distribution was at the origin of the appearance of a straight disclination line perpendicular to the easy axis across the center of the LC nematic droplet.[159] By close observation of Figure 4-12 *d* and Figure 4-12 *f* we identify a ring defect, a circular loop of disclination line in the middle of the droplet around the fiber, as shown schematically in 3D (Figure 4-12 *i*) and top and side (perpendicular to the fiber main axis) (Figure 4-12 *j*) views of the director field configuration.

4.3.1.2 Theoretical study of the stability of the ring defect

It was shown theoretically that a topologically non-trivial point defect (monopole) can be energetically unstable against expanding into a ring defect by taking a nematic liquid crystal as an example:[261-263]

From Equation 1-3 the distortion energy for point and line defects can be estimated, and the free energy for point and line defects are:

$$F_{point} \sim 8\pi K_1 R + F_{p,core}$$

Equation 4-3

And

$$F_{line} \sim \left(\frac{\pi}{8}\right) \cdot (K_1 + K_3) \cdot L \cdot \log\left({}^{D}/_{\xi}\right) + F_{l,core}$$

Equation 4-4

K_1 and K_3 are the Frank elastic constants of splay and bend deformations, respectively, L is the length of the line defect, D is the radius of the system cross section normal to the line defect. $F_{l,core}$ and $F_{p,core}$ are the core energies which come from the singular regions. These terms will be of the order

$$F_{p,core} \sim \xi^3 \cdot \Delta f$$

Equation 4-5

$$F_{l,core} \sim \xi^2 \cdot L \cdot \Delta f$$

Equation 4-6

Where ξ is the nematic coherence length (which is also the approximate radius of disclination core), and Δf the condensation energy density of the defect core, which is related to the average Frank elastic constant and the nematic coherence length: $\Delta f \sim K/\xi^2$. Imagine a sphere of radius αa which encloses the ring defect. Outside the sphere, the configuration can be seen as that of the point defect. Accordingly, the free energy that comes from the region is expected to be about $8\pi K_1(R - a\alpha)$ from Equation 4-3. Inside the sphere, the configuration might be regarded as that of the ring defect that is bent to be a ring. Then distortion energy from this region should be around $(\frac{\pi}{8}) \cdot (K_1 + K_3) \cdot 2\pi a \cdot \log({}^{D}/_{\xi})$ where a is the radius of the ring defect, since L and D should be taken as $2\pi a$ and $a\alpha$ respectively in this case. Therefore the difference of the free energy between the ring and point defect $\Delta F(a) = F_{ring}(a) - F_{point}$ can be roughly estimated as

$$\Delta F(a, \alpha) \sim 2\pi a \cdot \{-4\alpha K_1 + \xi^2 \Delta f + (\pi/8) \cdot (K_1 + K_3) \cdot \log(\alpha a/\xi)\} - \xi^3 \Delta f$$

Equation 4-7

The length $D=\alpha a$ is the radius of the effective sphere which encloses the ring defect (outside this sphere the configuration can be seen as that of the point defect). Expression (Equation 4-7) has two terms which depend on the ring radius a: one proportional to $(-a)$ and other to $(a \log a)$. The first term is related to the relaxation of the distortion inside the ring and the second term represents the "standard" contribution from the line defect of strength s=+1/2 and total length $2\pi a$. The energy of the ring defect can get smaller than that of the point defect, that is, the point defect is unstable, if the $(-4\alpha K_1 + \xi^2 \Delta f)$ term is negative, which is the case when the energy density Δf of the defect core is low enough. In that case the free energy (Equation 4-7) has a minimum at a finite $a \sim 0.1.\xi \exp(5\alpha)$. Mori and Nakanishi[262] used an obscure argument to obtain the ratio $\alpha \approx 1.4$ to predict the equilibrium ring radius: $a \approx 80\xi$. However, in our case the disclination ring observed in Figure 4-12 *f* is determined by the size of the fiber that has 1 μm diameter. If we assume the value of coherence length for a typical thermotropic liquid crystal $\xi \approx 10$ nm,[263] the cut-off ratio is $\alpha \approx 1.21$, which means that the ring defect appears as a +1 radial monopole at distances $R \approx 1.2a$, i.e. in the most of the droplet volume. The diameter of the fibers allows for the experimental control of the ring defects size. By playing with the geometric arrangement of the fibers, more defect rings can be generated in the suspended liquid crystal droplets. An example is shown in Figure 4-12 *k-m* where two crossed rings can be seen tying together 90 º cross micron fibers. Figure 4-12 *n* shows the 3D representation of the two ring defects and Figure 4-12 *o* represents the top view of the director configuration around the cross-fibers.

4.3.1.3 The ring defects generation process

Of interest in this system is also the mechanism of formation of the topological defect structure. In order to investigate how the director structure evolves toward the final equilibrium configuration in the middle of the droplet, we heated the liquid crystal above the nematic-to-isotropic transition to erase all the defects. By cooling back through the isotropic-to-nematic transition we follow the generation and transformation of the defects emerging in the shell. Nematic 5CB with $K_1 < K_3$ forms bipolar drops if the director is parallel to the bounding surface, and radial drops if the director is homeotropic on this surface.[264] Bipolar drops are characterized by two surface defects, or "boojums". Radial droplets only contain a single radial point defect, or "hedgehog" at the droplet center. The transformation from a bipolar to a radial configuration, which can be achieved by changing the nematic anchoring from parallel to perpendicular, at the droplet surface, involves the appearance of new defects via the transformation of the bipolar structure into the axial structure.

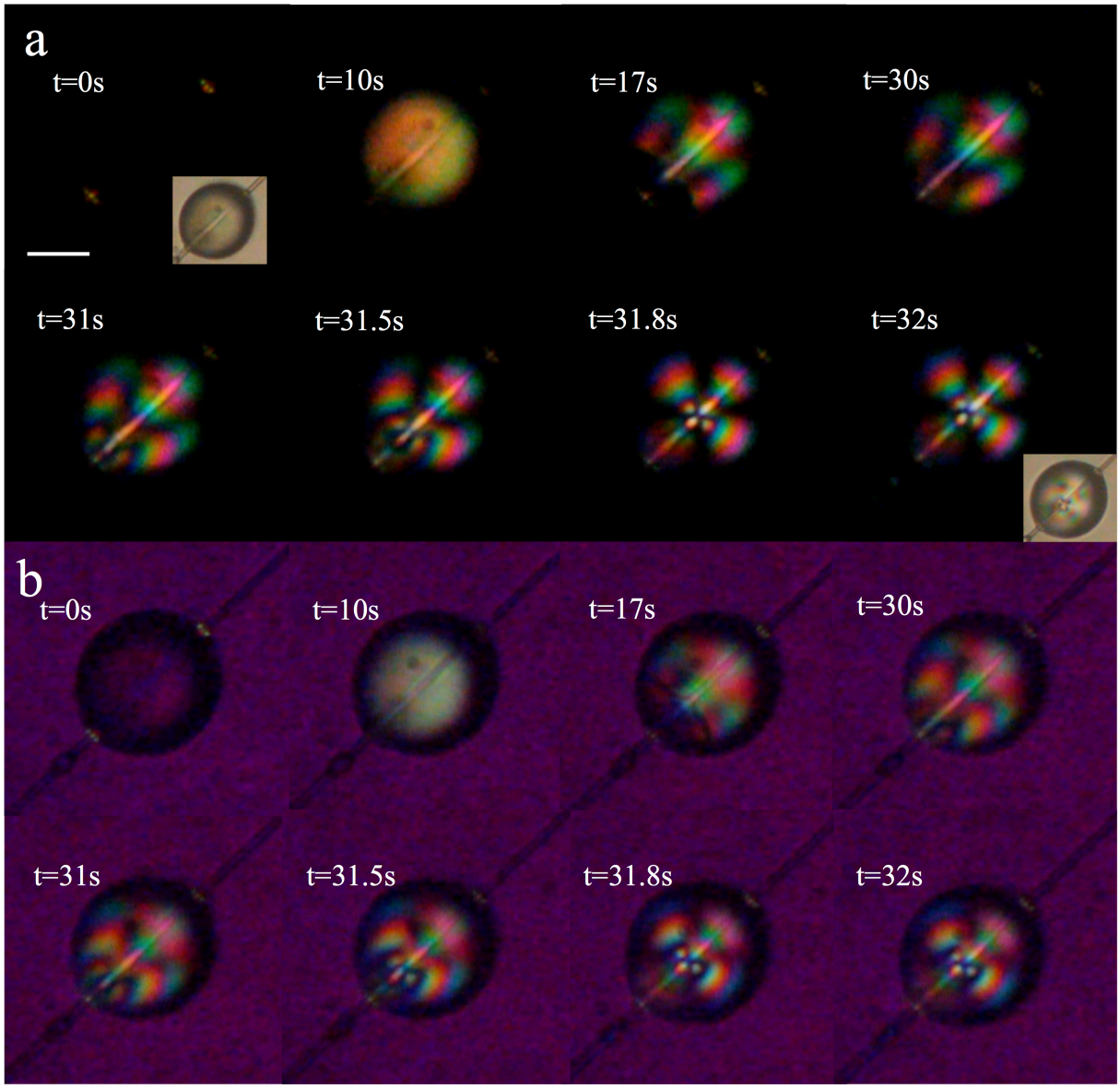

Figure 4-13 Cross-polarized **a.** and 530 *nm* quarter wavelength retardation plate **b.** image snapshots for the time evolution of the nematic shell from the isotropic phase (t = 0 *s*) to the equilibrium nematic configuration (t = 32 *s*). Insets in **a** (t=*0 s* and t=32 *s*) represent bright field images of the shell. The scale bar in **a.** t = 0 *s*, corresponds to 10 μm. The cooling speed is 0.3 ºC min^{-1}.

This is characterized by the emergence of an equatorial disclination line and its migration leading to the formation of a point defect.[215] The symmetrical location of this defect ring with respect to the original location of the point defects in the bipolar drop results from the orientation of the nematic in the bulk of the droplet, which does not change as the drop transforms from bipolar to axial; it remains oriented along the original boojum axis. Subsequently, the closed line shrinks and disappears, leaving a point defect on the surface of the drop. This defect then migrates toward the center; it is a hedgehog, which is a point defect in three dimensions, and characterizes the radial configuration.

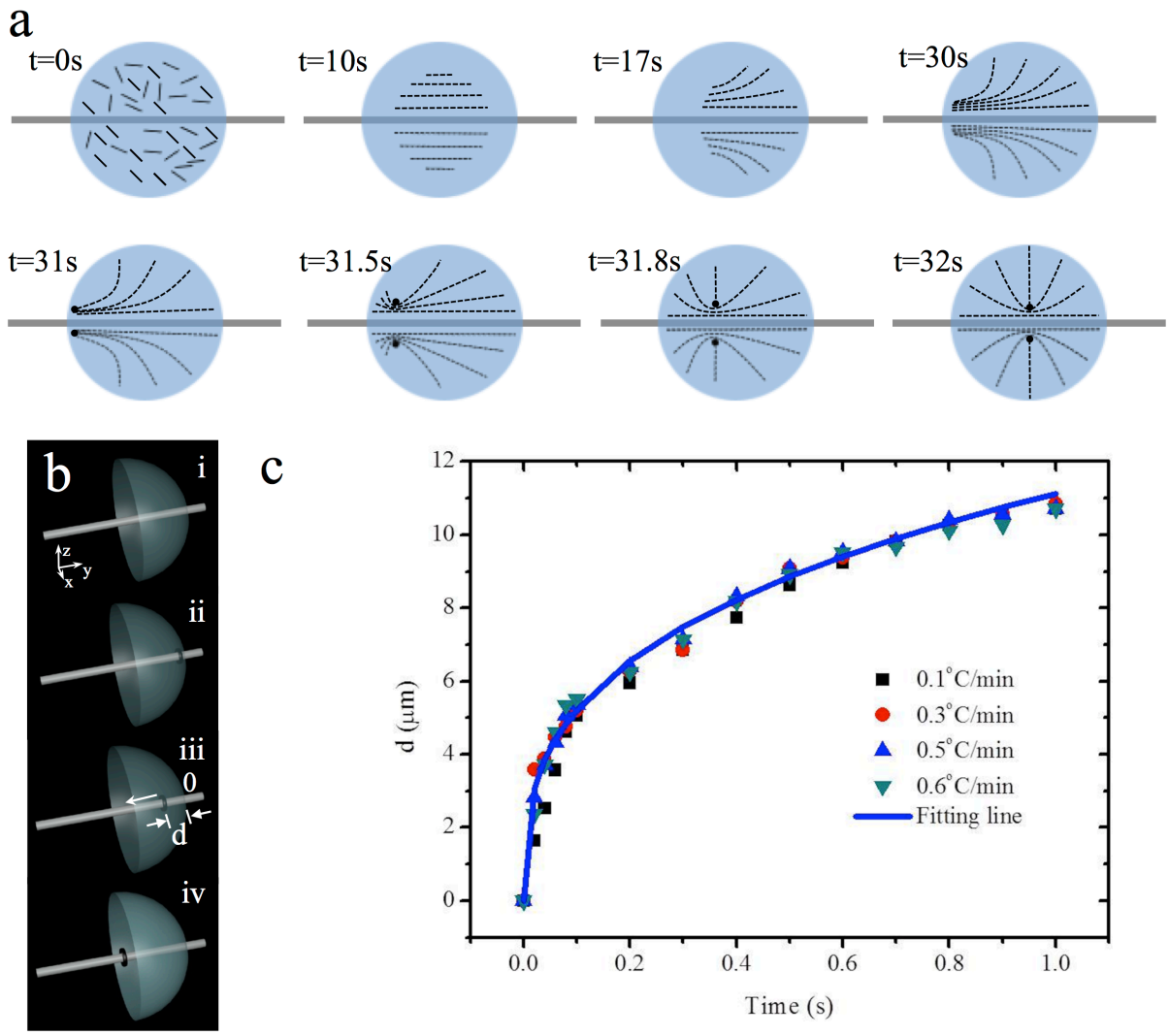

Figure 4-14 The schematics from the photographs in Figure 4-13 **a.** show a cross-section of the drop along the plane containing the fiber and the center of the sphere. The solid line refers to the fiber which passes through the center of the droplet. The dotted lines refer to the director field inside the drop. In this process the isotropic initial drop (t = 0 *s*) transforms into the transient axial drop (t = 10 *s*), characterized by a parallel alignment of the nematic configuration along the fiber. Subsequently, this nematic configuration disappears, leaving a ring defect around the fiber on the surface of the drop. This ring defect in three dimensions is a torus line which then migrates toward the center of the droplet along the fiber main axis. **b.** 3D scheme gives the translational movement of the disclination line along the fiber. **c.** Displacement of the torus disclination line along the fiber for different cooling rates. Within the experimentally observed range, the motion is accelerated along the fiber axis joining the periphery of the droplet and its center. The line corresponds to $d \approx t^{0.33}$.

More recently, the evolution of bipolar defects in shells of liquid crystals, when the boundary condition for the nematic configuration at the outer surface of the shell is changed from parallel to homeotropic, was investigated.[213] It was found that a tangential director configuration at the inner surface and perpendicular at the outer surface involves the generation of a disclination ring that shrinks with time, eventually disappearing. Although the process is reminiscent of that encountered in bulk nematic droplets, in the case of nematic shells the two defects on the inner surface were found to

play a relevant role in the overall evolution process.[213] In our system we observed that upon cooling the shell below the isotropic-to-nematic transition temperature (Figure 4-13 and Figure 4-14) an aligned director configuration region appears at the bulk liquid crystal droplet, close to the fiber, and initially remains oriented parallel to the fiber as shown in Figure 4-13 and Figure 4-14 (t = 10 *s*). Subsequently, the director starts bending towards one side of the droplet near the fiber surface (Figure 4-13 and Figure 4-14, t = 30 *s*). By doing so, the director in the bulk does not distort appreciably; it remains very much tangentially oriented along the fiber main axis. The defect ring forms at one of the sides in which the fiber crosses the nematic liquid crystal droplet (Figure 4-13 and Figure 4-14, t = 31 *s*) and migrates along the fiber main axis to the center of the drop (Figure 4-13 and Figure 4-14, t = 32 *s*). This is the equilibrium structure for the 5CB nematic used in this experiment.

From Figure 4-14 the displacement of the ring defect can be evaluated. We measure the separation between the center of the droplet (distance d in Figure 4-14 *b*) and the moving disclination ring and find that it decelerates as it moves toward the center of the droplet (Figure 4-14). The initial velocity is approximately equal to v = 120 $\mu m\ s^{-1}$, and it reduces to v = 10 $\mu m\ s^{-1}$ as the ring defect approaches the center of the droplet. The *d(t)* time dependence was fitted with the power-law function $d(t) \approx t^{a}$. We obtained $\alpha \approx 0.33$ which correlates well with theoretical predictions.[265]

4.3.1.4 Melting process of the ring defects

The heating process is qualitatively different. In this case, the starting ring defect, located at the center of the drop, starts to increase its diameter, as shown in Figure 4-15 *a* and *b*, in the microscope images for *t* = 15 *s*, and in the corresponding schematics in Figure 4-16. Close to this defect line an isotropic droplet starts to develop (Figure 4-15 *a* and *b*, *t* = 18 *s*) and the radius grows at a rate *v* = 0.79 $\mu m s^{-1}$ in the first 5 seconds decreasing to *v* = 0.235 $\mu m s^{-1}$ in the last 1 second. The density (ρ) difference between 5CB and the inner isotropic drop, $\rho_{5CB\text{-}LC} - \rho_{5CB\text{-}Iso} \approx 2.08 \times 10^{-3}\ g\ cm^{-3}$,[268] causes a local thinning of the shell at one of the drop surfaces. As a consequence, the two drops (anisotropic and isotropic) are not concentric; because of this asymmetry the anchoring effect of nematic molecules at the fiber and air interface boundaries is stabilized at the opposite side to the place where the inner drop touched the outer liquid crystal drop. The director orientation promoted by the boundary surfaces propagates as shown in Figure 4-15 and Figure 4-16 from *t* = 24 *s* to *t* = 25 *s*. Subsequently the process is similar, in the reverse sense, to that observed on cooling. As shown in Figure 4-16, from *t* = 25 *s* to *t* = 40 *s*, the director aligned configuration vanishes from the side of the droplet, around the fiber main

axis, to generate an isotropic drop. The 3D schematic representation of the ring defect disappearance upon heating is shown in Figure 4-16 *a*.

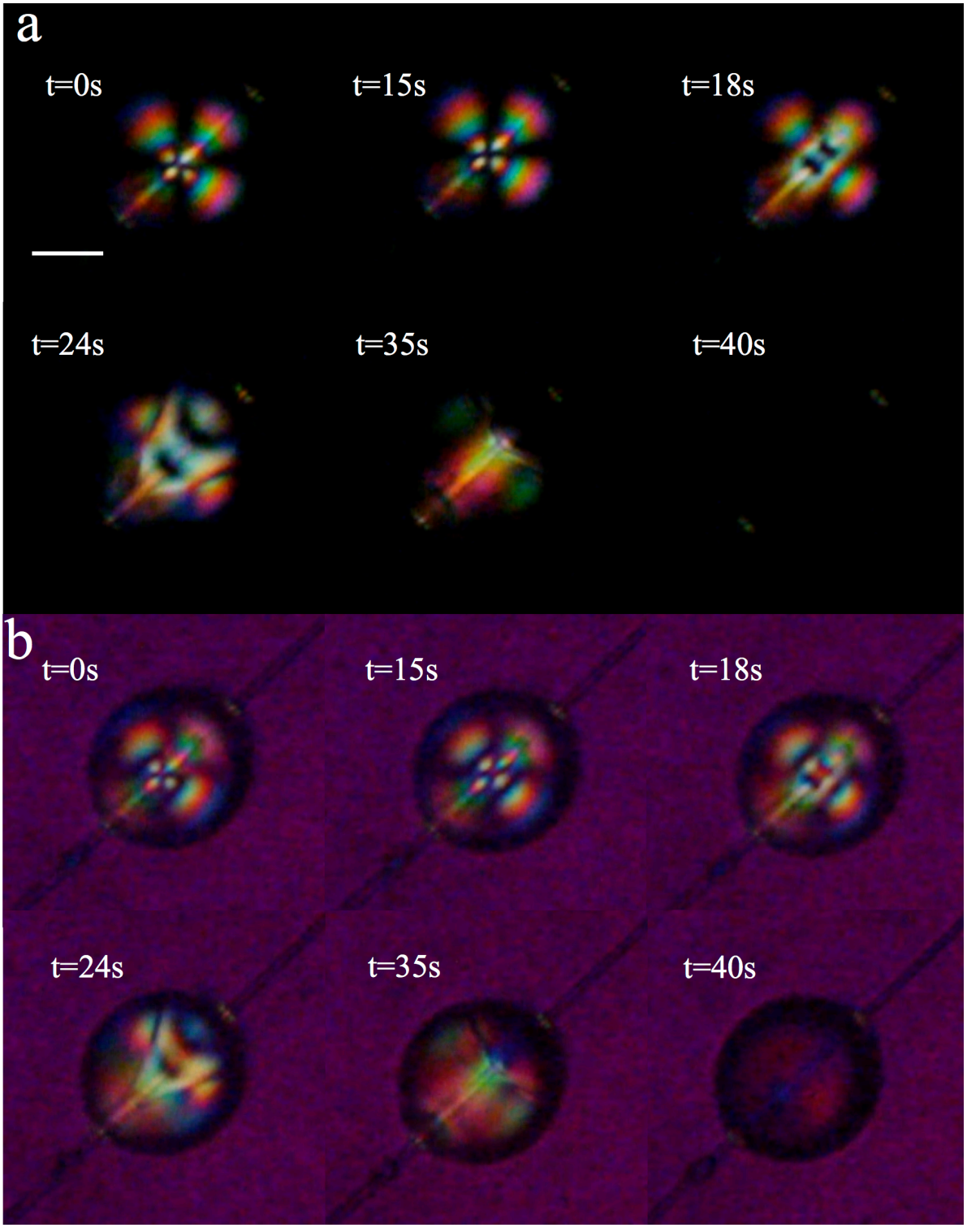

Figure 4-15 Cross-polarized **a.** and 530 *nm* quarter wavelength retardation plate **b.** image snapshots for the time evolution of the nematic shell from the equilibrium director configuration (t = 0 *s*) to the isotropic phase (t = 40 *s*). The scale bar in **a**, t = 0 *s*, corresponds to 10 *μm*. The 5CB nematic droplet is supported in air by a 1 *μm* fiber; the heating speed is 0.3 *°C* min^{-1}.

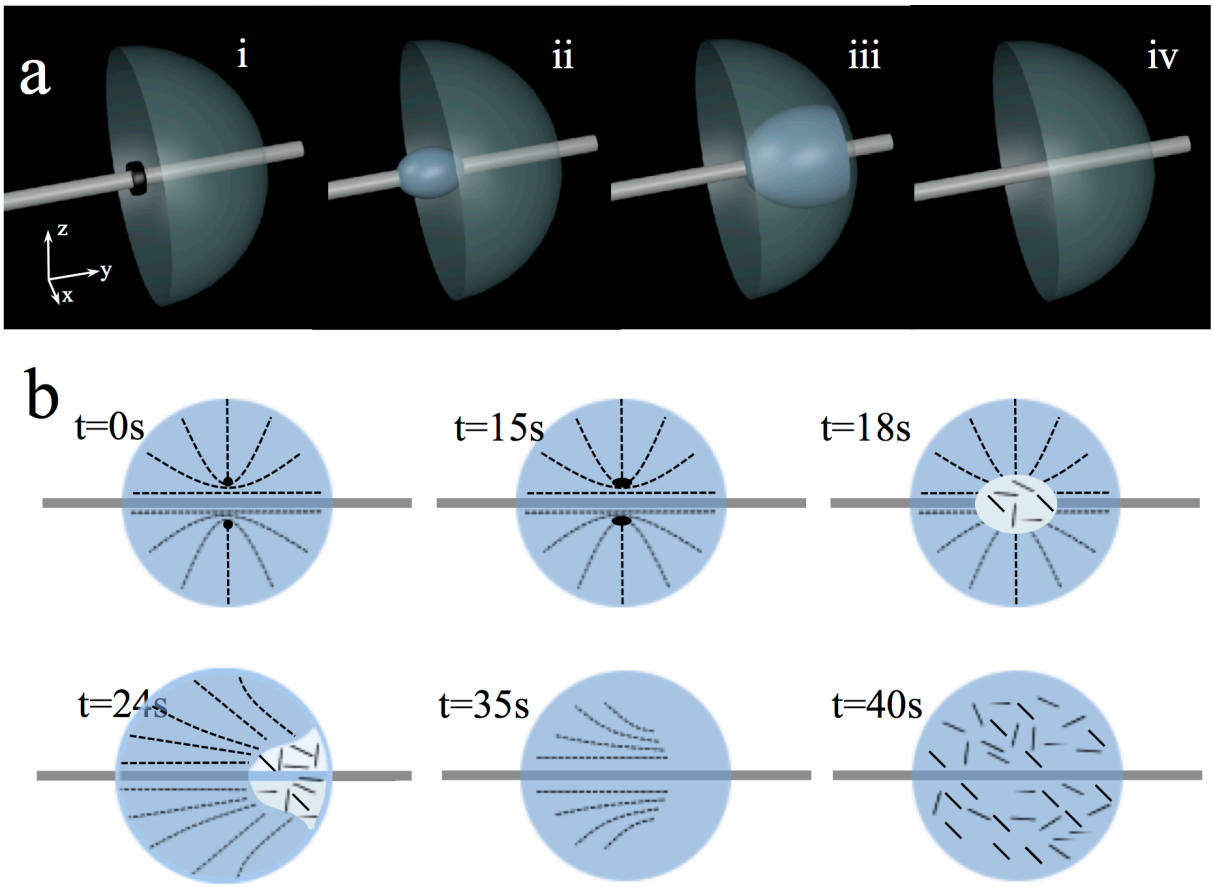

Figure 4-16 The schematics from the photographs in Figure 4-15 **a.** show a 3D representation of the evolution of the ring defect at the center of the droplet upon heating. **b.** A cross-section of the drop along the plane containing the fiber and the center of the sphere. The solid line refers to the fiber which passes through the center of the droplet. The dotted lines refer to the director field inside the drop. In this process the initial ring defect at the center of the drop (t = 0 *s*) first increases the diameter (t = 15 *s*) and then transforms into a transient isotropic drop (t = 18 *s*) which grows (from t ≈ 18 *s* to ≈23 *s*). After reaching a critical diameter touches the outer drop surface and starts to shrink due to the growth of the director alignment from the opposite side of the drop, in around 1 second the inside isotropic drop disappears leaving the director mainly aligned tangential to the fiber (t = 25 *s*). Subsequently (in about 15 *s*), this nematic configuration disappears, leaving an isotropic droplet. Throughout this process the initial diameter of the droplet remains constant.

4.3.1.5 Droplets under the electric field -- microrotors induced by electric field

To study the effect of an external electric field upon the system we focus on a single suspended droplet (diameter 34 μm) shown in Figure 4-17 *a*. The application of an external electric field induces changes in the nematic orientation depending on the voltage. We detected two distinct regimes in the response to the application of an electrical potential difference (AC, 50 *Hz*). First we observed that the radius of the ring disclination increases as the voltage difference applied across the cell was ramped from 3.8 to 5.1 $V\,\mu m^{-1}$.

To better evidence the periodic particle motion we measured the light intensity in a small fixed area on the particle path inside the droplet. In the Figure 4-18 *b*, we plot this light intensity measured from the images of movie. In this way we can clearly observe the periodicity of the particle motion around the fiber main axis as is also shown in the sequence of images plotted in Figure 4-18 *a*. With low electric field intensities, the radial configuration slightly bends to progressively align ***n*** with ***E***, as expected for 5CB with a positive dielectric anisotropy, until a π wall forms in the plane perpendicular to the applied field, which contains the fiber axis. This wall divides the drop into hemispheres, with a π rotation of ***n*** as the wall is crossed from one hemisphere to the other. In each hemisphere, the director is essentially aligned with ***E*** and the drop still contains the original ring disclination line. The direction of the electric field is normal to the fiber main axis, and it promotes a director profile normal to the fiber surface.

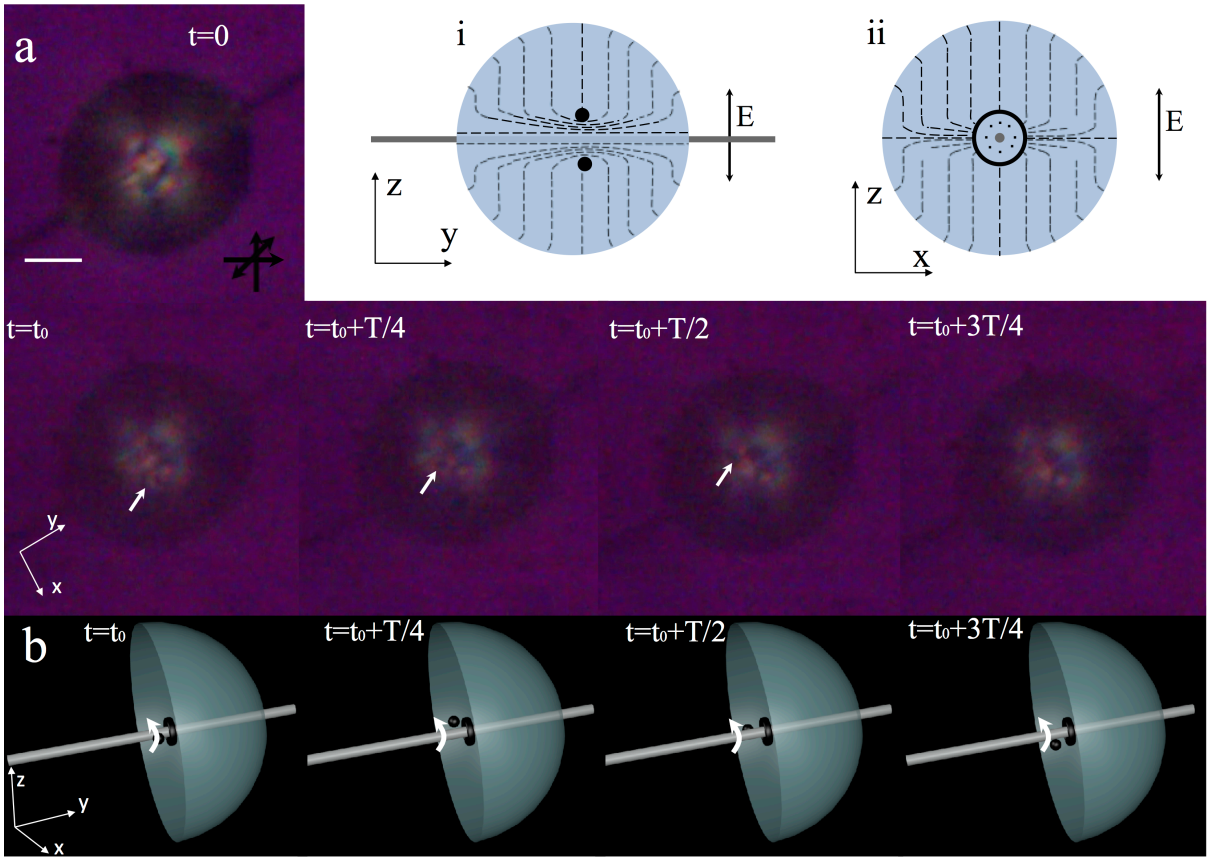

Figure 4-17 (**a.** and **b.**) Electric field-induced (1.05 V/V_c) particle rotation inside a 34 *μm* diameter 5CB drop suspended in a 1 *μm* fiber. The pictures are taken using a 530 *nm* quarter wavelength retardation plate between cross-polars. The white arrow indicates the position of the rotating particle around the fiber main axis. (**i** and **ii**) The effect of the electric field on the cross-sections of the drop along the planes xy and xz containing the fiber and the center of the drop. The solid line refers to the fiber which passes through the center of the droplet. The dotted lines refer to the director field inside the drop. To illustrate the orbit of the particle around the fiber main axis and the position of the ring defect a 3D time sequence is also given.

This effect likely causes the growth of the near surface radial alignments and thus an expansion of the ring disclination. The movement of the ring along the fiber axis can occur because of the unique geometry and boundary conditions on ***n*** near the fiber surface, the only way the ring defect finds to escape is along the fiber axis. In Figure 4-17 *i* and *ii* a scheme is proposed depicting the director field top and side (perpendicular to the fiber main axis) views configuration.

Surprisingly for fields above a certain critical field E_c = 3.796 $V\,\mu m^{-1}$, a small spherical particle-like object of concentrated director deformation starts to orbit around the fiber axis with a constant speed. At the genesis of this moving "particle" should be the initial movement of the disclination ring along the fiber, away from the center of the droplet (Figure 4-17 *b*). The nature and structure of the particle are still undetermined but two main possibilities come to mind; one where it is a soliton generated by the large electric field applied to a highly distorted nematic, the soliton nature does not include the formation of new defects and so preserves the total topological charge.[269] The other possibility is the formation of a more complex defect structure with a nontrivial topological charge that tries to recover the symmetry broken by the presence of the strong external electric field.

The "particle" keeps a constant size and is stabilized by the boundary conditions imposed by the fiber and the electric field, which prevent it from moving out of the sample and to contract and vanish due to the fiber cylindrical shape. The velocity was evaluated experimentally as a function of the applied voltage (Figure 4-18 *a*) and can be roughly determined by equating the viscous torque hindering its motion to the electric field generated torque. Some insight into the particle motion can be gained for the defect structure case by considering the motion of a line defect upon application of an electric field described by *Cladis et al*. which estimates, for 5CB, that $c/V \approx 4.2\ b^{-1}\ \mu m\ V^{-1}\ s^{-1}$,[270] where *c* is the linear speed of the disclination line, *V* the voltage and b a dimensionless number of order unity. The number *b* depends only on the details of the energy dissipation in this region, where the strain is singular.

As a result, *b* will depend on the core size and may show some weak field dependence as well. From Figure 4-18 *a* we can evaluate the value of the slope, which gives ω/V equal to 5.67 rad $V^{-1}\ s^{-1}$. Considering that the initial radius of the ring disclination line is equal to 1.4 μm, in our system, the value of *b* is of the order of 2.0, which is roughly in accordance with the value estimated by theory for 5CB.[271] However the values of *r* vary with voltage (see Figure 4-18 *a*) and the simple model used predicts no variation for *b*.

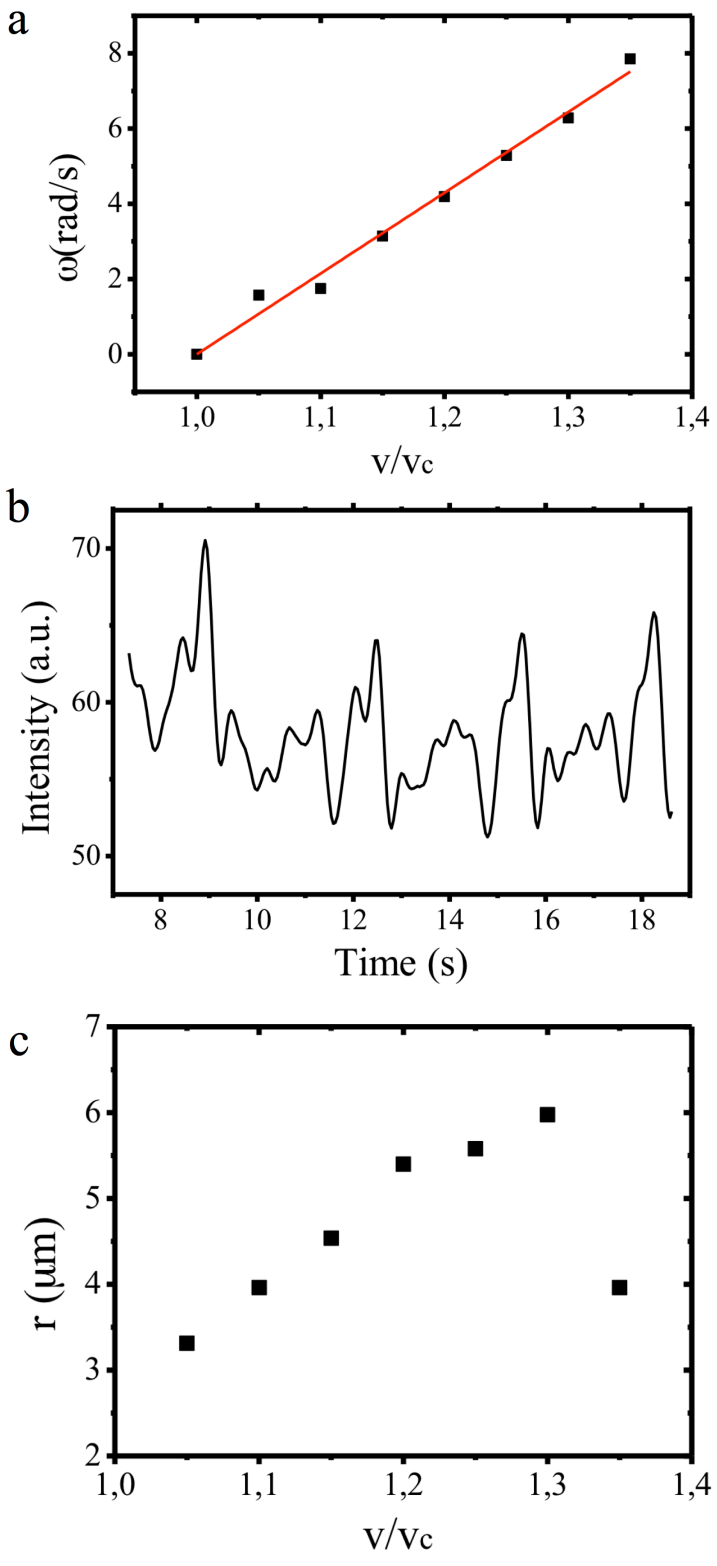

Figure 4-18 **a.** Particle speed versus the applied field perpendicular to the fiber (in the same direction of the ring disclination line) showing that the rotational speed, in the range of the measurements, is linear in the applied voltage. **b.** represents the light intensity measured in a small fixed area placed in the particle path. **c.** represents the variation of the radius of the particle trajectory as a function of the applied voltage. The bar corresponds to 10 μm.

4.3.2 Cholesteric drops threaded in thin cellulosic fibers

We study the structures of cholesteric droplets pierced by cellulose fibers with planar anchoring at droplet and fiber surfaces. By varying the temperature we demonstrate the role of twisting power and droplet diameter on the equilibrium structures. The observed structures are complemented with detailed numerical simulations of possible director fields decorated by defects. Three distinct structures, a bipolar and two ring configurations, are identified experimentally and numerically. We believe that collecting cholesteric liquid crystal microdroplets on thin long threads opens new routes to produce fiber waveguides decorated with complex microresonators.

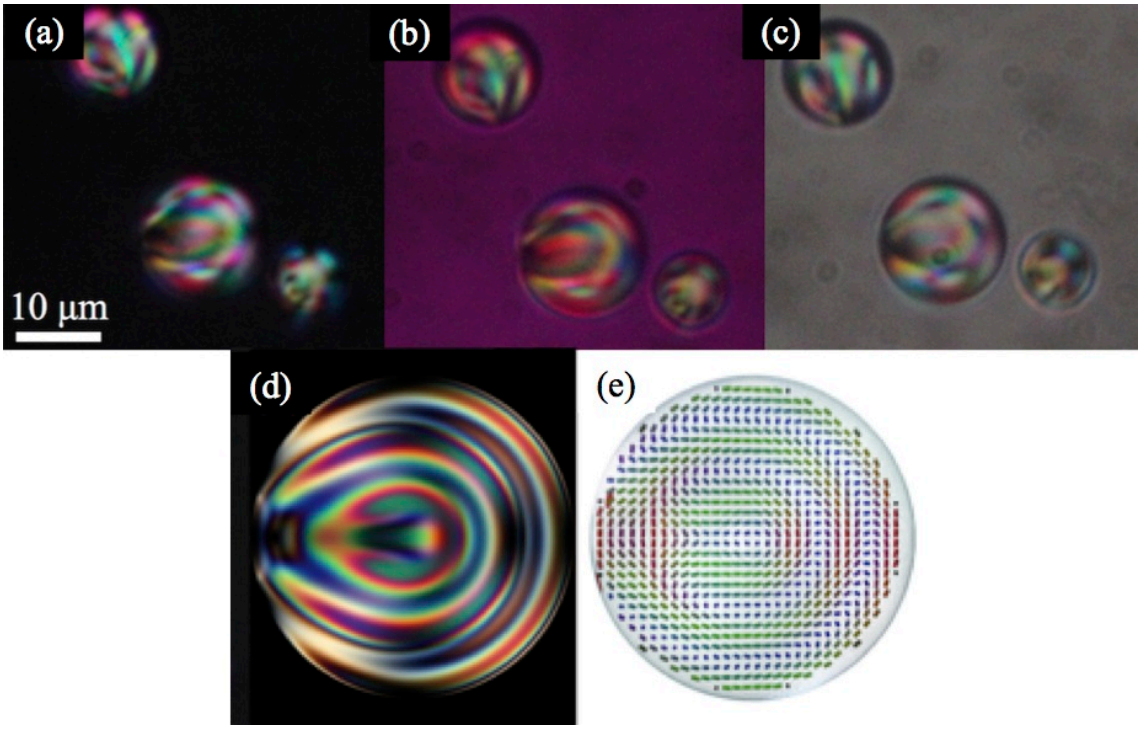

Figure 4-19 POM pictures of cholesteric LC droplets in glycerol with planar anchoring. **a**. under crossed polarizers, **b**. with a 530 *nm* quarter wavelength retardation plate, between cross polarizers, **c**. under parallel polarizers. **d.** Simulated polarization micrograph of the RSS structure and **e.** the corresponding simulated director field.

The droplets, with diameters less than 50 μm, with planar anchoring were observed in glycerol mixture between cross polarizers (Figure 4-19, Figure 4-20, and Figure 4-21) before being collected to the fibers. The cholesteric necklaces, consisting of suspended drops around fibers stretched in air, were observed under a polarizing microscope between cross and parallel polarizers and by using a 530 *nm* retardation plate inserted between cross polars at a 45º position. The liquid crystalline droplets produced satisfy the constraint R>>K/W, for planar anchoring strength W and Frank elastic constant K (for 5CB the surface effects are predicted to dominate and the liquid crystal within the droplet will be strained to satisfy the boundary conditions[272]).

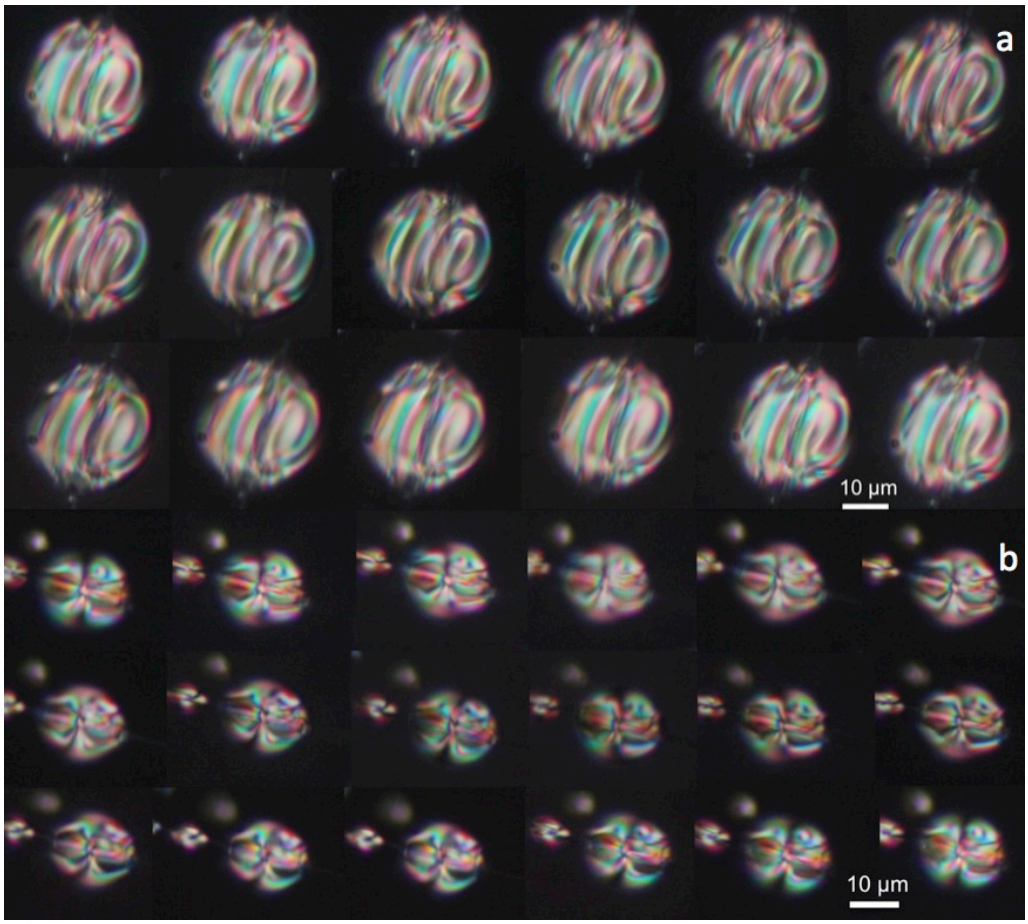

Figure 4-20 POM pictures of two cholesteric LC droplets, with different diameters, threaded by thin cellulose fibers with planar anchoring at the fiber surface and air interface do to the existence of a thin glycerol layer, which encloses the LC drops. In **a.** and **b.** the cross polarizers were rotate 10 º, from picture to picture, under crossed polarizers.

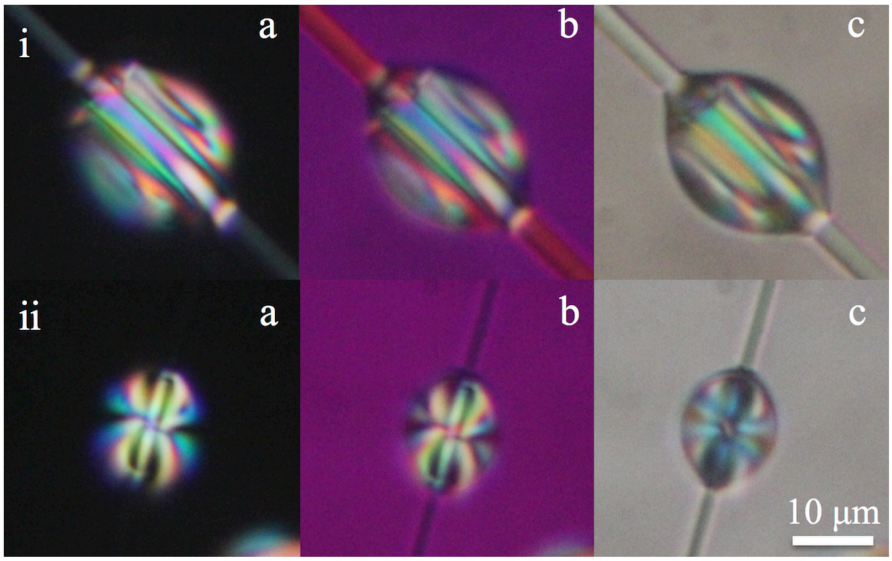

Figure 4-21 Cholesteric bead textures observed by POM. **i** The bipolar structure with cylindrical cholesteric layers; **ii.** small cholesteric bead with totally different distribution of the director. The photos were taken in **a.** under the cross polarizers, in **b.** with a 530 *nm* quarter wavelength retardation plate, between cross polarizers, and in **c.** under parallel polarizers.

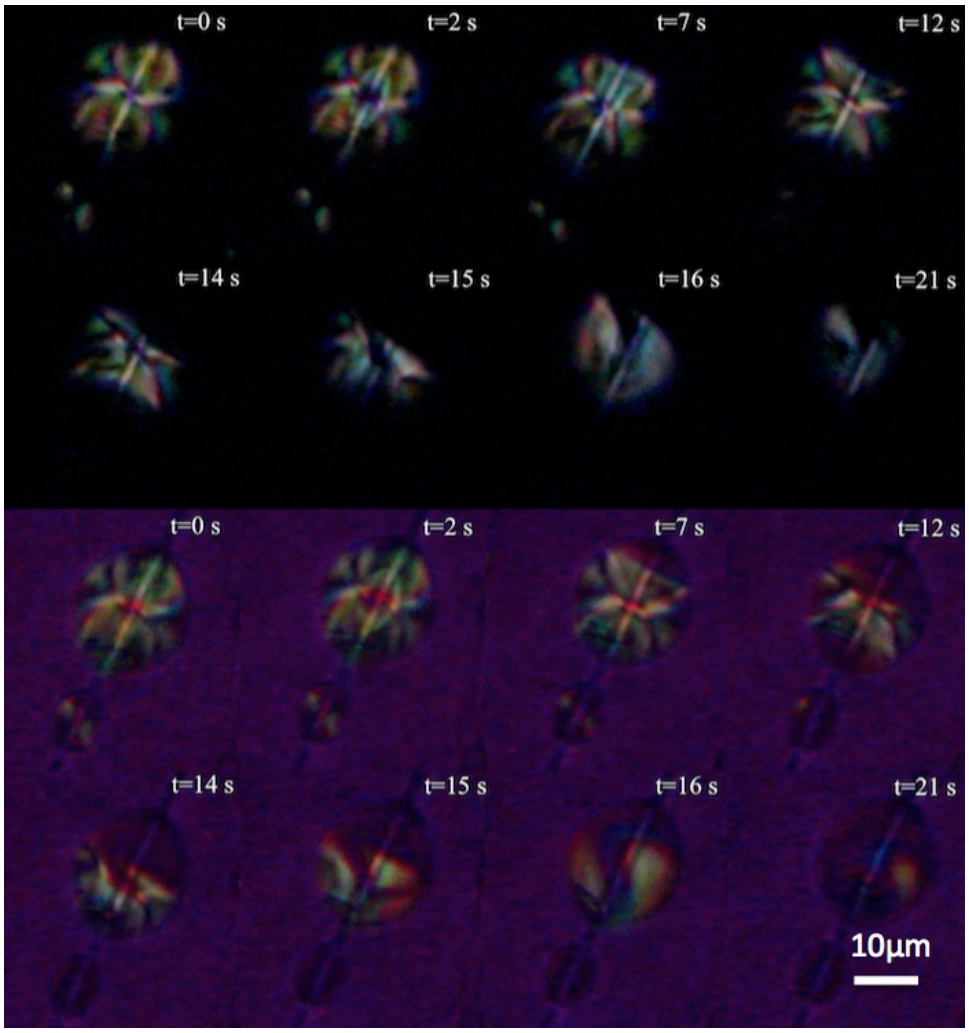

Figure 4-22 Heating of a ring structure cholesteric droplet. The 5CB*Mix drop is surrounded by a shell of glycerol and suspended in air by 1 μm fiber. The heating and cooling rates are both equal to 1 $°C/min$. Heating between cross polarizers (**Upper**) with a 530 nm quarter wavelength retardation plate (**Bottom**) the snapshots images represent the time evolution of the nematic shell from the equilibrium director configuration (t = 0 s) to the isotropic phase (t = 21 s). In this process the initial ring defect at the center of the drop (t = 0 s) first increases the diameter (t = 2 s) and the surface ring defects increase their separation.

Typical examples of two ellipsoidal droplets suspended on a microfiber, 27 μm and 18 μm major axis, given in Figure 4-21 show a series of dark and bright domains that change color by cross polarizers rotation (Figure 4-20) indicating the presence of concentric cylindrical cholesteric layers. By varying the size of the drop relatively to the cholesteric pitch, the configuration changes from a bipolar to a ring structure, as shown by images taken with cross polarizers, with a retardation plate and parallel polarizers, of Figure 4-21 *a*, *b* and *c*, respectively.

In order to investigate how the ring defect structure, observed for droplets with structures similar to those shown in Figure 4-21 *ii*, evolves toward the final equilibrium configuration in the middle of the droplet, we heat the liquid crystal above the cholesteric-to-isotropic transition to obtain the disordered

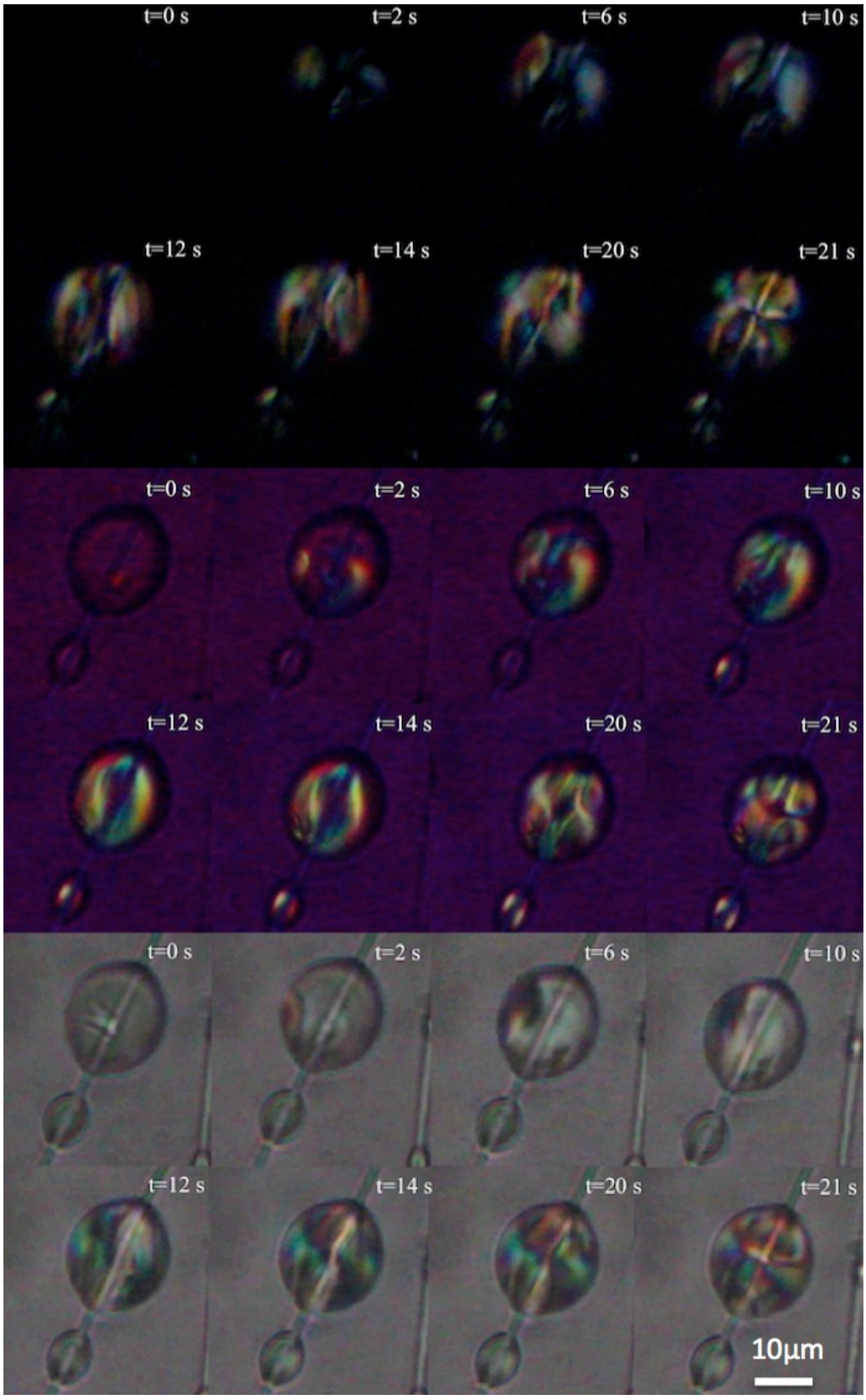

Figure 4-23 Cooling processes of a ring structure cholesteric droplet. Cooling cross polarizers (**Upper**) with a 530 *nm* quarter wavelength retardation plate (**Middle**) parallel polarized (**Bottom**) image snapshots for the time evolution of the 5CB*Mix cholesteric shell from the isotropic phase (t = 0 *s*) to the ring configuration (t = 21 *s*). In this process the initial isotropic droplet transforms into a transient axial drop (t = 14 *s*) that develops ring defects at the centre of the droplet around the fiber at t = 21 *s*.

state. In the heating process, the starting ring defect, located at the center of the drop, starts to increase its diameter, as shown in Figure 4-22 (t = 2 *s*) and close to this defect two symmetric black spots can be observed. For t > 2 *s* the anisotropy, inside the droplet, starts to vanish asymmetrically relatively to the fiber main axis. This can be due to the twisting of the nematic layers. By cooling back the isotropic-to-nematic transition temperature we follow the generation and transformation of the defects generated in the droplet (Figure 4-23). After 21 *s* the central ring defect reappears from shrinking of a black region, which starts to appear. Eventually, the initial state is reproduced.

Numerical modelling

A numerical simulation was performed to try to obtain the same structure that was observed by POM, as an aid to better define the liquid crystalline structure that was visualized. The director field and defects are predominantly controlled by the boundary conditions and the twisting power qR with R being the radius of drops and $q=2\pi/P$ the inverse cholesteric pitch[273]. Initial modelling of cholesteric droplets[221,274,275] with degenerate planar anchoring provided only general features of structures. Recent numerical modelling based on the minimization of the *Landau-de Gennes* free energy that allow a detailed description of structures, unveiled a number of peculiarities in the defect regions[273].

For low twisting powers ($qR < 2\pi$) the stable droplet configuration is the bipolar structure (BS, see Fig.4 *a* in Ref.[273]), with two surface boojums positioned diametrically. The boojums are connected along the diameter of the droplet by a non-singular disclination with winding number +1 (cholesteric λ^{+1} line[95]). For higher twisting power values, $qR > 2\pi$, the bipolar structure continuously evolves into the radial spherical structure (RSS) that is the only one also observed in our dispersed cholesteric droplets. The RSS is characterized by a helicoidal winding of the λ^{+1} disclination into a double helix structure that spans from the center of the droplet to the surface and ends with two singular +1 surface boojums, topologically equivalent to those in the BS. The RSS is thus notably different from the Frank-Pryce model structure[276] where a singular line with winding number +2 spans from the center of the droplet to the surface. Among these two ground states of spherical cholesteric droplets, many intricate metastable states that differ in the topological defects and director fields can appear[273]. It is worth to mention the diametrical spherical structure (DSS) with cylindrical symmetry that is metastable because it consists of a series of ring defects around the symmetry axis (See Fig.2a in Ref.197). The director field can be visualized as a sequence of concentrically positioned tori of deformed double twist cylinders with cross-sections being rather of the banana shape instead of being circular.

In the bipolar structure, the director field in the central region is predominantly in the direction of the escaped disclination. One could thus expect that piercing such droplets with cylindrical microfibers that prefer planar surface orientation would stabilize the bipolar structure. However, the inclusion of such additional surfaces change also the droplet shapes. Since the nematic elasticity is typically much weaker than the surface tension[208], the interfacial energy is thus expected to govern the shape of the threaded droplets. The typical experimental value for the surface tension of the LC-glycerol interface is σ~0.02 J/m^2 [277]. Similar order of magnitude of σ is expected for the LC-air[278] and LC-solid interface. Since the typical estimate for the elastic constant K of a LC is 5 pN, the ratio K/σ that has a dimension of a length, is very small, a few nanometers. It implies that the shape of the threaded droplets that are larger than a few nanometers is controlled mainly by the surface tension rather than by the elastic energy. The high wettability of the cellulose fibers (low contact angle) provokes a change of the spherical shape to an approximately ellipsoidal form. Such deformed shapes could stabilize states that are otherwise metastable. Due to the planar requirements at the surface of the microfiber inside the ellipsoidal droplet, the preferred structures are expected to be close to the BS and DSS, both having a central region that would be the least frustrated by a fiber. Therefore, we used the director field Ansatze of the BS and DSS[273] as initial conditions in the numerical modeling of threaded droplets. We obtained three distinct structures: the bipolar structure and two ring structures. The bipolar structure is essentially the same as BS in spherical droplets with no additional inclusions. It is characterized by the cylindrical symmetry of the director field around the fiber, twisting only in the radial direction perpendicularly from the fiber. It has no bulk defects, only two boojums positioned diametrically at the fiber-droplet surface. Note the similarity between the simulated micrograph and the experimental micrographs in Figure 4-24. Both ring structures are also approximately cylindrically symmetric, however the director field is mostly different in the central region having an additional -1/2 disclination ring around the fiber and one (see Figure 4-24 *b*) or two (Figure 4-24 *c*) surface rings at the fiber surface. A comparison with experimental pictures (Figure 4-21 *ii a-c*) indicates a close resemblance to the double ring structure. The ring structures are a compromise between the cylindrical cholesteric layers of the bipolar structure and additional twisting accommodated by the ring defects. This resembles the DSS structure in simple spherical droplets through the toron-like elements (toroidal shape double-twist cylinders) between the central ring defects and both surface boojums. In the second ring structure, the extra surface ring is thus compensated by the additional cholesteric layer compared to first ring structure. All three structures have similar free energies, and their stability largely depends on the material parameters such as the radius-to-pitch ratio and the curvature of the droplet surface (i.e. the eccentricity of the ellipsoidal droplets). In a preliminary numerical study we also examine further increase of chirality (shorter pitch). Starting from a bipolar configuration in a given droplet shape we show that by lowering the pitch, ring defects are gradually forming and restructure towards a configuration resembling the diametrical spherical structure.

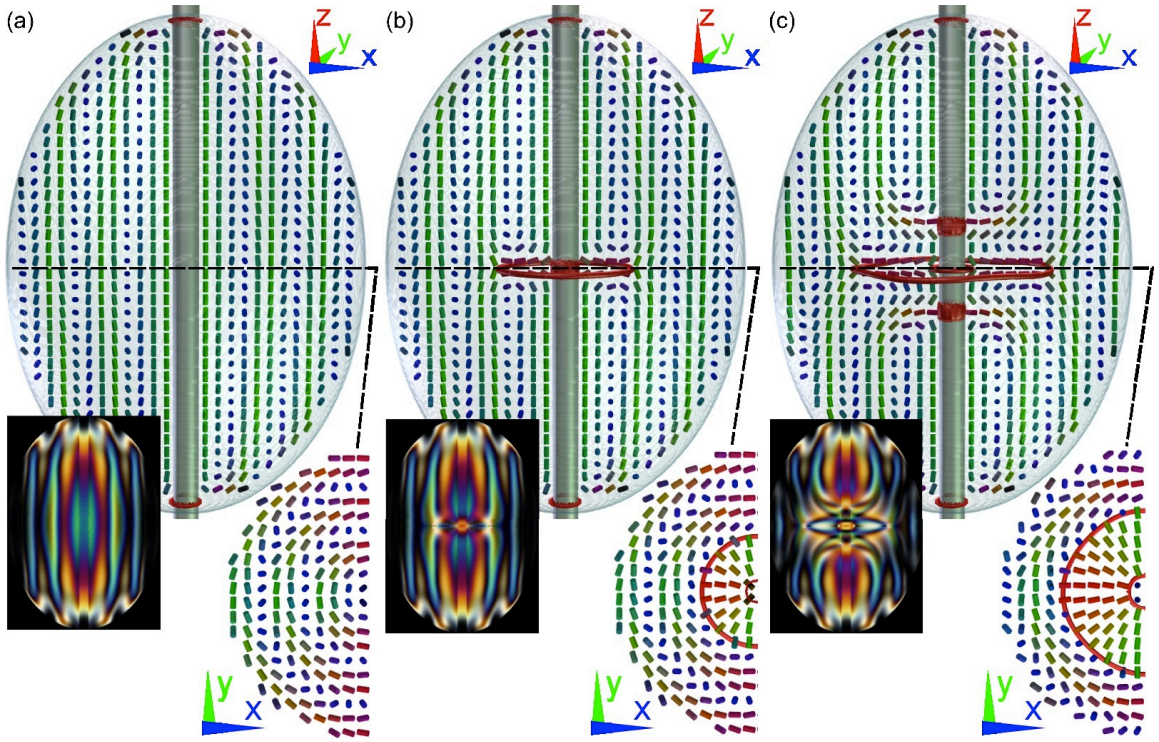

Figure 4-24 Numerically calculated structures in cholesteric drops threaded on thin fibers: **a.** the bipolar structure, **b.** the ring structure, and **c**. the double ring structure, both with additional bulk -1/2 disclination ring around the fiber in the ring structures. In both ring structures the toron-like elements emerge. Note the resemblance of the micrographs with experiments.

The numerical model used is based on a continuum Landau-de Gennes approach, where the tensorial order parameter Q_{ij} is used to construct the total free energy as in Ref.[279]. The free energy minimisation procedure is able to fully characterize (i) the defect regions *i. e.* the areas with depressed nematic degree of order, (ii) elastic distortions induced by intrinsic twisting of a cholesteric state, and (iii) the degenerate planar nematic anchoring at the droplet surface. Focusing on the effect of chirality, one-constant elastic approximation is used. The total free energy F is numerically minimized by using an explicit Euler relaxation finite difference scheme on a cubic mesh[273,280,281]. The surface of the droplet is modelled as an ellipsoidal shell of mesh points (with eccentricity 1.25) and the microfiber as a cylindrical shell of mesh points, both with thickness equal to the mesh resolution. To cover the cholesteric twisting of the director and in particular the defects, typically more than 70 mesh points per pitch are used. For material parameters the values typical for a thermotropic cholesteric liquid crystal are used: $L = 4 \times 10^{-11}$ N, $A = -0.172 \times 10^{6}$ J/m^3, $B = -2.12 \times 10^{6}$ J/m^3, $C = 1.73 \times 10^{6}$ J/m^3, $W_0 = 10^{-3}$ J/m^2.

To compare the calculated structures with experiments, polarization micrographs of simulated structures are calculated with the Jones 2 x 2 matrix formalism using $n_o = 1.5$ and $n_e = 1.7$ as ordinary and extraordinary indices of refraction, respectively. The formalism incorporates only the leading contribution – the local variations in birefringence of the nematic refractive index due to the director

field – and neglects reflections and refractions at the droplet surface[282]. More specifically, in this formalism, the light beam is propagated along a chosen direction and the total phase shift between ordinary and extraordinary polarisations is accumulated. To reproduce color images, we repeat the calculation for 10 different wavelengths in an approximate radiation spectrum of a black body at 6000 *K* (i.e. the white light approximation) and sum the results for each wavelength corresponding to RGB color spectrum weights. The polarization micrographs are calculated for the director structure scaled by a factor of 3 to match the scales of typical experiments and obtain a more quantitative comparison[283].

4.4 Conclusions

As presented in this chapter, we have generated stable closed micro-domains of liquid crystals, having a complex topology, from a simple toroid to more complex structures corresponding to higher number of "holes" in a closed sphere.

The appearance of an electric field induced microrotor brings an added interest and technological potential to these systems in spite of its still elusive nature. The advantage of these liquid crystal microrotors is the simplicity of their formation, their stability and large response to electric fields. We demonstrate that a micro-soft motor can be created and tuned which may be of interest for application in microdevices, tunable micro-cavity lasers and soft matter photonic circuits.

We also experimentally generated stable cholesteric liquid crystal microdomains threaded on a cellulose fibers that exhibit toroidal topology. The otherwise well known structures in spherical cholesteric droplets are indeed modified by a presence of piercing cellulose fibers that change both the droplet shape and also topology. Theoretical analysis together with numerical modeling show possible structures and differences from spherical cholesteric droplets. We demonstrate that suspended chiral droplets exhibit, for higher twisting power values, a stable disclination line ring around the fiber main axis, similar to that in suspended nematic droplets with homeotropic anchoring.

The experimental system presented in this work is highly sensitive to temperature variations resulting in structural changes, which opens new possibilities to the production of enhanced "weightless" weblike thermo-optical devices. Such weblike mats based on electrospun micro/nano cellulose-fibers could therefore make an ideal system for the fundamental and theoretical studies of liquid crystal micro droplets suspended on air. Moreover, the incorporated cellulose thread inherently connected to the liquid crystal-director and defect-structure could possibly couple these systems to diverse external fields, making such systems potentially useful for tunable photonic and waveguide applications.

Chapter 5 Cellulosic nano/micro fibers in liquid crystal (light shutter)

This chapter's work description and discussion was based on the following paper:

Y. Geng, P. Brogueira, J.L. Figueirinhas, M.H. Godinho and P.L. Almeida, "Light shutters from nanocrystalline cellulose rods in a nematic liquid crystal", *Liquid Crystals*, 2013, 40, 769-773.

5.1 Introduction

In this chapter we will describe the application of Nanocrystalline Cellulose (NCC), introduced in chapter 1 (1.1.2) to produce an electro-optical device. We produced light shutter devices that serve the same purpose as the traditional PDLC devices and that were optimized due to the liquid crystal anchoring conditions on cellulose and also due to the large surface contact area between LC and the NCC.

A different type of cellulose based LC electro-optical devices can also be prepared by stacking between two transparent conductive oxide coated glasses, two layers of a nematic liquid crystal having in between a thin film composed of NCC rods. Thin films of NCCs produced by controlled assembly have gained recent attention not only due to a number of emerging applications such as fabrication of advanced materials but also because they can be used to better understand the nature of complex interactions in related systems.[284] NCC rods can be produced from cellulosic biomass into powder, liquid and gel forms. The rigid rod-shaped monocrystalline cellulose domain is in the range 1 - 100 *nm* in diameter and tens to hundreds of nanometers in length. NCC rods have a high average aspect ratio (70) and large surface area (200 m^2/g).[285] These morphological characteristics seem ideal for the present application since the polymer/liquid crystal interaction is maximized giving rise to improved electro-optical properties.

By using NCC rods we were able to improve some of the most relevant parameters characterizing the electro-optical behavior. A brief description of the proposed working mechanism for these devices is presented and numerical simulations based on this mechanism of both the optical transmission and the cells' electrical capacitance are compared with the obtained results validating the underlying working model considered.

5.2 Experimental

To prepare these electro-optical shutters we used a film of NCC rods with a thickness of 4 μm and the commercial Nematic Liquid Crystal (NLC) 4-cyano-4'-pentylbiphenyl (5CB). The NCC rods film was sandwiched in between two layers of NLC with a thickness of 14 μm each and this stack of layers placed between two indium tin oxide-coated glasses. The cell's total thickness excluding the glass substrates was around 32 μm. Figure 5-1 represents the device's assembly.

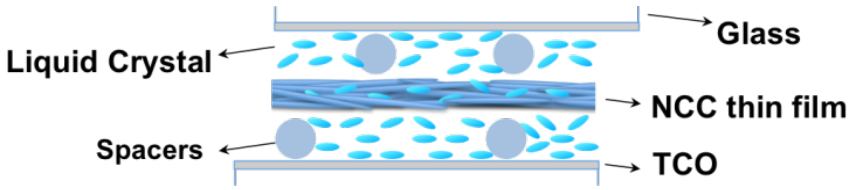

Figure 5-1 Schematic representation of the device's assembly.

The electro-optical (EO) characterization of the samples was carried out using a laser ($\lambda = 0.6328\ \mu m$) equipped optical bench in association with a function generator, a voltage amplifier, and a diode detector. Laser light hits the sample normally and upon crossing it is collected at the diode detector whose output is fed to an amplifier and later recorded with a digital storage scope. To measure the sample switching times (turn ON time t_{on} and turn OFF time t_{off}), AC voltage pulses were used. All measurements were performed at the same controlled temperature of 25 ^{o}C.

5.3 Results and Discussion

The improved device's characteristics can be better evidenced by comparison with those of earlier cellulose based devices.[181,286] Figure 5-2 shows the applied electric field dependence of the light transmission coefficient for three distinct samples. For the NCC rods device, the transmission coefficient reaches a highest value of 78 % while the lowest transmission is 0.2 %. The turn-on field has a very low value of around 1.28 $V/\mu m$ (the electric field required to achieve 90 % of the device's maximum transmission). The response times measured fall in the milliseconds range being the t_{on} a short time of 1 *ms* and the t_{off} a relatively long time of around 17 *ms*. Figure 5-3 shows images of the macroscopic behavior of the device in the ON and OFF states as well as the correspondent Polarized Optical Microscopy (POM) pictures, between cross polarizers. POM pictures show a characteristic nematic texture in the OFF state. In the ON state a non-black image is obtained although the nematic director is now mainly aligned with the applied electric field. The birefringence still observed is due to the NCC rods film as can be viewed in Figure 1-5.

The major step forward in the EO properties of this type of device is the significant reduction of the turn ON electric field as well as the decrease in the response time to reach the ON state, although we observe a worsening in the device's maximum transmission coefficient. Figure 5-2 presents a comparison between the EO characteristics of earlier proposed devices[181,286] and the NCC rods device.

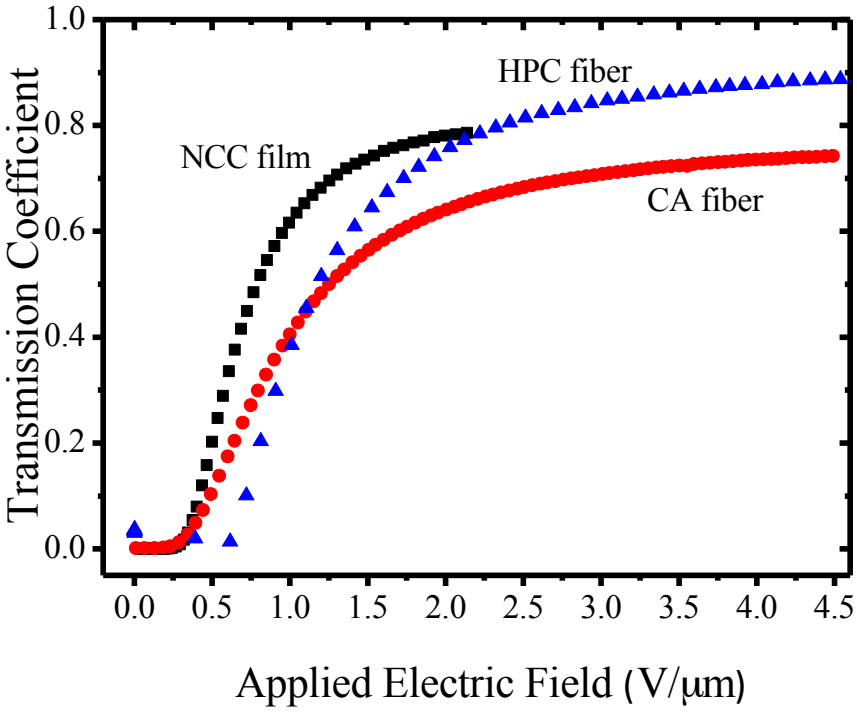

Figure 5-2 Curves of the applied electric field dependence of the light transmission coefficient of these devices compared with electrospun cellulose fiber devices (HPC and CA). [181]

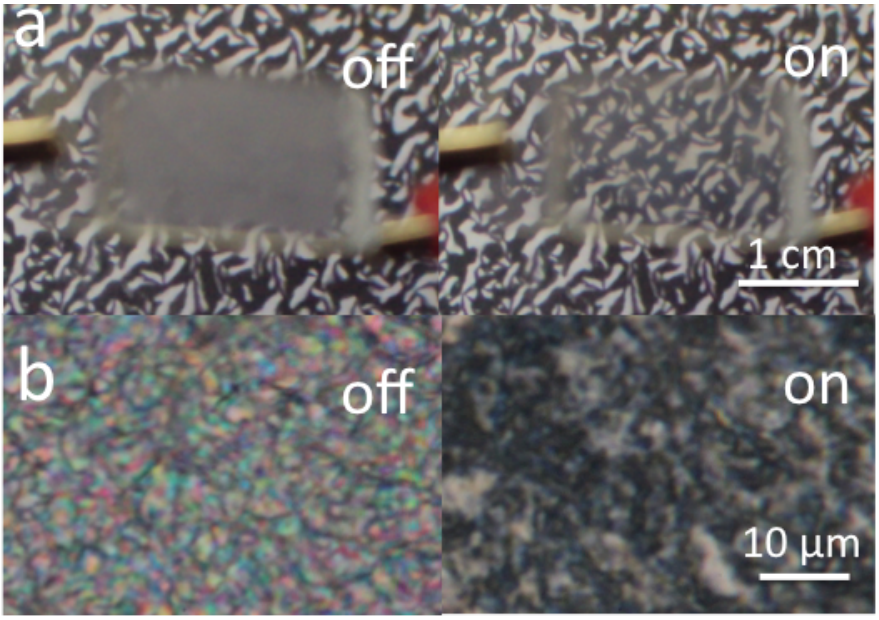

Figure 5-3 **a.** Macroscopic and **b.** POM (between cross polars) photographs of the ON and OFF states.

In the former thin film device produced in a similar way, as the one reported in this work, but using a cellulose derivative (Hydroxypropylcellulose (HPC)) (device *d*) in Table 5-1), the thickness of the film was around 10 μm.[36] In that device, the ON transmission coefficient reached higher values. However it was a rather slow device and a high voltage was needed to switch it, primarily due to the

thickness of the cells (typically around 50 μm, limited by the film mechanical stability). The evolution of cellulose based light shutter technology lead us to produce thinner devices (typically around 13 µm) where a thin layer of fibers (HPC and Cellulose Acetate (CA)) where deposited directly onto the transparent conductive oxide coated glass (devices *b*) and *c*) in Table 5-1).[181] These devices produced using electrospun fibers, had improved transmissions (higher maximum transmissions in the ON state and lower minimum transmissions in the OFF state), lower turn ON voltages and lower response times in the ON and OFF states but higher turn ON fields. This was due to the fact that the polymeric fiber layer was acting as stabilizer of the NLC. The randomly distributed fibers enforce a random orientation of the NLC director in the OFF state close to the polymer-NLC interfaces, improving its scattering characteristics. Due to the good match between the ordinary refractive index of the NLC and the refractive indexes of HPC and CA fibers used, and the reduced thickness of the polymeric layer, a very clear ON state is achieved. Also, the commutation times were greatly reduced.

Table 5-1 Comparison between electro-optical properties of different types of cellulose devices.

Device	T_{max} (%)	T_{min} (%)	E_{on} ($V/\mu m$)	V_{on} (V)	e (μm) [a)]	t_{on} (ms)	t_{off} (ms)
a) NCC film device	78	0.02	1.28	41	32	1.10	17.82
b) CA fiber	74	0.2	2.15	28	13	1.48	6.41
c) HPC fiber	89	1.3	2.41	36	15	1.40	6.33
d) Cellulose film device	82	0.4	1.70	57	33	12.04	10.54

[a)] e represents the distance between electrodes of each studied device.

Regarding the device produced using NCC rods (device *a*) in Table 5-1), we observe that the maximum transmission in the ON state is slightly lower (78 %) but the minimum transmission in the OFF state is very low, significantly lower than the one presented by the CA fiber sample. These facts may be due to higher mismatch between the ordinary refractive index of the NLC (1.527) and the refractive index of the NCC rods film (1.499).[287] The E_{on} field was reduced as can be observed from the shift, to the left, of the respective curve presented in Figure 5-3.

This fact is linked with the presence of the NCC rods aligned film that locally induces alignment of the LC director reducing the defect network concentration when compared with devices *b*) and *c*) in Table 5-1. This fact is observable in the concurrent simulation of both the transmission coefficient and the cell´s capacitance shown in Figure 5-4 and Figure 5-5, which was carried out using for the 5CB NLC physical parameters, values very similar to the known bulk values.[181] Simulations carried out in HPC and CA fibers cells on the contrary required two times higher average elastic constants, which we believe to originate from a larger density of the director defects network induced by the locally randomly distributed fibers. The NCC rods device with a lower defect density allows the NLC director to align more easily and faster with the applied electric field.

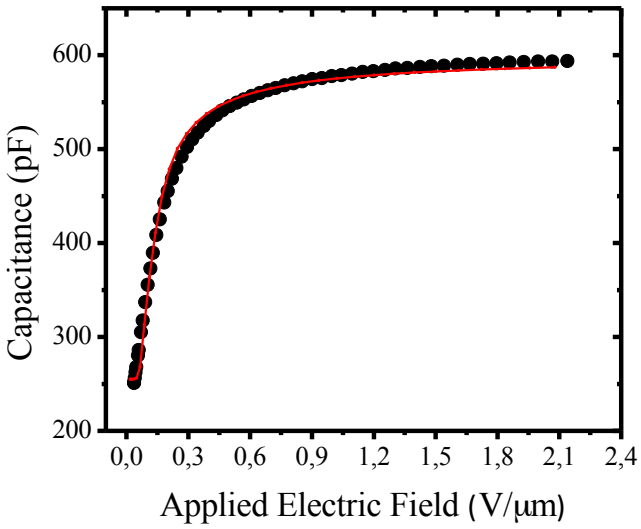

Figure 5-4 Experimental data and simulation of the applied electric field dependence of the device's capacitance.

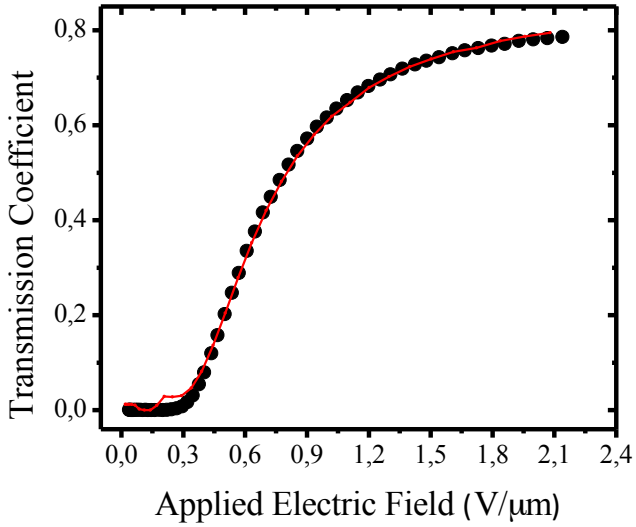

Figure 5-5 Experimental data and simulation of the applied electric field dependence of the light transmission coefficient.

To better understand the working mechanism of these devices we have carried out a simulation of their electro-optical response using a model that determines the director orientation within the LC layers using the nematic continuum theory based on the Frank elastic free energy and evaluates the optical response in the anomalous diffraction approach considering that the optical paths through the LC layers and polymer film are modulated by a random variable corresponding to a optical path change within the LC layers. This optical path change corresponding to a film thickness fluctuation in the micron range is most probably due to long wavelength static undulations of the aligned film surface.

The simulation shown in Figure 5-4 was obtained considering the dielectric and the Frank elastic constants and the indices of refraction of the NLC very similar to the values reported for bulk 5CB along with the cells physical characteristics.[288,289] Exact match to 5CB material parameters may not apply due to a small contamination of the NLC by NCC rods that can detach from the solid film.

5.5 Conclusions

We propose a new application for NCC rods by presenting a different method of preparation cellulose based light scattering shutters. We have identified the working mechanism of these light shutters by successfully simulating their electro-optical response. By using NCC rods we were able to tune the optical shutter characteristics, the turn ON field as well as the turn ON time were notably lowered when compared with other cellulose based LC devices. The production process is extremely simple and the device cost is smaller since a small amount of raw materials is needed to produce it.

Chapter 6 Conclusions and Future Work

6.1 Conclusions

During the studies performed and through the acquired knowledge on cellulose and liquid crystal systems the following main conclusions can be drawn:

- In order to understand more about the cellulose processing-structure-properties relationship, the precursor liquid crystalline cellulosic solutions were studied by Rheo-NMR. The NMR spectra allow the identification of five different stable ordering states, within shear and relaxation, which are well integrated in a mesoscopic picture of the system's structural evolution under shear and relaxation. This picture emerging from the large body of studies available for this system, by other experimental techniques, accounts well for the NMR data and is in good agreement with the three distinct regions of steady shear flow recognized for some lyotropic LC polymers.

- Shear transparent cellulosic freestanding films (≈ 22 μm thickness) can develop iridescence similar to that found in the petals of the tulip variety "Queen of the Night". The film's iridescence arises from the modulation of the surface into bands that periodically spread perpendicular to the shear direction. The incorporation of small quantities of nanocrystalline cellulose (NCC) rods in the precursor liquid crystalline solutions does not disturb much the optical properties of the solutions but enhance the mechanical characteristics of the films and affects their iridescence. Small bands periodicity, not affected by the presence of NCC rods, in the order of hundreds of nanometers, slightly deviated from the shear direction is also observed. The presence of NCC rods is crucial to tune and understand the film´s surface features formation. Our findings could lead to the improvement of new materials for application in soft reflective screens and devices. We report for the first time that those banded films can show iridescence, which is very similar to those found in Tulip "Queen of the Night" petals. This simple and low cost cellulosic material seems ideal to mimic the structures that can be found in plants, namely the type of gratings observed in the petals of many plant species.

- The orientational order of the sheared cellulosic films can be changed by a wide variety of stimuli, including the presence of moisture. Changes in the orientation of constituents give rise to stresses and strains, which result in changes in sample shape. This effect was used to build a soft cellulose-based motor driven by humidity. The motor consists of a circular loop of cellulose film, which passes over two wheels. When humid air is present near one of the wheels on one side of the film, with drier air elsewhere, rotation of the wheels results. As the wheels rotate, the humid film dries. The motor runs so long as the difference in humidity is maintained. Our cellulose liquid crystal motor thus extracts mechanical work from a difference in humidity.

- For the first time electrospun HPC fibers were used as a support for liquid crystal droplets, generating a new system ideal for the study of liquid crystal droplets under different anchoring,

confinement and external stimuli conditions. We found that different defects can be generated under the confinement of the fibers in both nematic and cholesteric liquid crystals. A unique phenomenon was also found under different stimuli like temperature and electric field.

- We also propose an application of nanocrystalline cellulose rods and liquid crystal system as light scattering shutters. We have identified the working mechanism of these light shutters by successfully simulating their electro-optical response. By using NCC rods we were able to tune the optical shutter characteristics, the turn ON field as well as the turn ON time were notably lowered when compared with other cellulose based LC devices. The production process is extremely simple and the device cost is smaller since a small amount of raw materials is needed to produce it.

6.2 Future work

Based on the obtained results achieved in this work I am still interested on cellulose based systems processing-structure-property relationships. Cellulose liquid crystalline lyotropic and thermotropic systems are complicated due to the polymer chain rigidity and also to the network of inter- and intra-molecular interactions. So in the future, a proper way will be choose to study this system to understand more about the processing-structure-property relationships.

Understand more about the liquid crystal drops confined on different support materials and geometries. Try to find more application such as in liquid crystal laser or sensor area. [249,250,290]

References:

1. Hayashi, T. *The Science and Lore of the Plant Cell Wall: Biosynthesis, Structure and Function*. (Brown Walker Press, 2006).
2. Krassig, H. A. *Cellulose*. (Archives contemporaines Editions, 1993).
3. Zugenmaier, P. *Crystalline cellulose and cellulose derivatives: Characterization and structures*. (Springer, 2008).
4. Attala, R. H., American Chemical Society. Cellulose, P., Division, T. & Meeting, A. C. S. *The Structures of cellulose: characteristics of the solid state*. (American Chemical Society, 1987).
5. Kamide, K. *Cellulose and Cellulose Derivatives*. (Elsevier Science, 2005).
6. Siqueira, G., Bras, J. & Dufresne, A. Cellulosic bionanocomposites: A review of preparation, properties and applications. *Polymers* **2**, 728-765, (2010).
7. http://www.fibersource.com/f-tutor/cellulose.htm.
8. Jarvis, M. Cellulose stacks up. *Nature* **426**, 611-612, (2003).
9. Gorham, W. & Niegisch, W. Encyclopedia of Polymer Science and Technology. *edited by Mark, HF, Gaylord, N. and Bikales, NM, Interscience, New York*, (1971).
10. Langan, P., Sukumar, N., Nishiyama, Y. & Chanzy, H. Synchrotron X-ray structures of cellulose Iβ and regenerated cellulose II at ambient temperature and 100 K. *Cellulose* **12**, 551-562, (2005).
11. Nishiyama, Y., Langan, P. & Chanzy, H. Crystal structure and hydrogen-bonding system in cellulose Iβ from synchrotron X-ray and neutron fiber diffraction. *J Am Chem Soc* **124**, 9074-9082, (2002).
12. Nishiyama, Y., Sugiyama, J., Chanzy, H. & Langan, P. Crystal structure and hydrogen bonding system in cellulose Ia from synchrotron X-ray and neutron fiber diffraction. *J Am Chem Soc* **125**, 14300-14306, (2003).
13. http://sitimardianayaakob.blogspot.pt/2010/03/carbohydrates.html.
14. O-Sullvan, A. Cellulose: the structure slowly unravels. *Cellulose* **4**, 173-207, (1997).
15. Azizi Samir, M. A. S., Alloin, F., Sanchez, J.-Y. & Dufresne, A. Cellulose nanocrystals reinforced poly (oxyethylene). *Polymer* **45**, 4149-4157, (2004).
16. Beck-Candanedo, S., Roman, M. & Gray, D. G. Effect of reaction conditions on the properties and behavior of wood cellulose nanocrystal suspensions. *Biomacromolecules* **6**, 1048-1054, (2005).
17. Dong, X. M., Kimura, T., Revol, J. F. & Gray, D. G. Effects of ionic strength on the isotropic-chiral nematic phase transition of suspensions of cellulose crystallites. *Langmuir* **12**, 2076-2082, (1996).

18. Eichhorn, S., Dufresne, A., Aranguren, M., Marcovich, N., Capadona, J., Rowan, S., Weder, C., Thielemans, W., Roman, M. & Renneckar, S. Review: current international research into cellulose nanofibers and nanocomposites. *J Mater Sci* **45**, 1-33, (2010).
19. Favier, V., Chanzy, H. & Cavaille, J. Polymer nanocomposites reinforced by cellulose whiskers. *Macromolecules* **28**, 6365-6367, (1995).
20. Habibi, Y., Lucia, L. A. & Rojas, O. J. Cellulose nanocrystals: chemistry, self-assembly, and applications. *Chemical reviews* **110**, 3479, (2010).
21. Petersson, L., Kvien, I. & Oksman, K. Structure and thermal properties of poly (lactic acid)/cellulose whiskers nanocomposite materials. *Composites science and technology* **67**, 2535-2544, (2007).
22. Tokoh, C., Takabe, K., Fujita, M. & Saiki, H. Cellulose synthesized by Acetobacter xylinum in the presence of acetyl glucomannan. *Cellulose* **5**, 249-261, (1998).
23. Klemm, D., Kramer, F., Moritz, S., Lindström, T., Ankerfors, M., Gray, D. & Dorris, A. Nanocelluloses: A New Family of Nature‐Based Materials. *Angewandte Chemie International Edition* **50**, 5438-5466, (2011).
24. Cannon, R. E. & Anderson, S. M. Biogenesis of bacterial cellulose. *Critical Reviews in Microbiology* **17**, 435-447, (1991).
25. Klemm, D., Heublein, B., Fink, H. P. & Bohn, A. Cellulose: fascinating biopolymer and sustainable raw material. *Angewandte Chemie International Edition* **44**, 3358-3393, (2005).
26. Klemm, D., Schumann, D., Kramer, F., Heßler, N., Koth, D. & Sultanova, B. in *Macromolecular Symposia.* 60-71 (Wiley Online Library).
27. Klemm, D., Schumann, D., Udhardt, U. & Marsch, S. Bacterial synthesized cellulose—artificial blood vessels for microsurgery. *Progress in Polymer Science* **26**, 1561-1603, (2001).
28. Yamanaka, S., Watanabe, K., Kitamura, N., Iguchi, M., Mitsuhashi, S., Nishi, Y. & Uryu, M. The structure and mechanical properties of sheets prepared from bacterial cellulose. *J Mater Sci* **24**, 3141-3145, (1989).
29. Araki, J., Wada, M., Kuga, S. & Okano, T. Flow properties of microcrystalline cellulose suspension prepared by acid treatment of native cellulose. *Colloids and Surfaces A: Physicochemical and Engineering Aspects* **142**, 75-82, (1998).
30. Braun, B. & Dorgan, J. R. Single-step method for the isolation and surface functionalization of cellulosic nanowhiskers. *Biomacromolecules* **10**, 334-341, (2008).
31. Goussé, C., Chanzy, H., Excoffier, G., Soubeyrand, L. & Fleury, E. Stable suspensions of partially silylated cellulose whiskers dispersed in organic solvents. *Polymer* **43**, 2645-2651, (2002).
32. Grunert, M. & Winter, W. T. Nanocomposites of cellulose acetate butyrate reinforced with cellulose nanocrystals. *Journal of Polymers and the Environment* **10**, 27-30, (2002).
33. Yuan, H., Nishiyama, Y., Wada, M. & Kuga, S. Surface acylation of cellulose whiskers by drying aqueous emulsion. *Biomacromolecules* **7**, 696-700, (2006).
34. Ranby, B. G. Aqueous colloidal solutions of cellulose micelles. *Acta Chemica Scandinavica* **3**, 649-650, (1949).
35. Nickerson, R. & Habrle, J. Cellulose intercrystalline structure. *Industrial & Engineering Chemistry* **39**, 1507-1512, (1947).
36. Rånby, B. G. Fibrous macromolecular systems. Cellulose and muscle. The colloidal properties of cellulose micelles. *Discussions of the Faraday Society* **11**, 158-164, (1951).
37. Bondeson, D., Mathew, A. & Oksman, K. Optimization of the isolation of nanocrystals from microcrystalline cellulose by acid hydrolysis. *Cellulose* **13**, 171-180, (2006).
38. Marchessault, R., Koch, M. J. & Yang, J. Some hydrodynamic properties of ramie crystallites in phosphate buffer. *J Coll Sci Imp U Tok* **16**, 345-360, (1961).
39. Marchessault, R., Morehead, F. & Walter, N. Liquid crystal systems from fibrillar polysaccharides. (1959).
40. Araki, J., Wada, M., Kuga, S. & Okano, T. Birefringent glassy phase of a cellulose microcrystal suspension. *Langmuir* **16**, 2413-2415, (2000).
41. Revol, J.-F., Godbout, L., Dong, X.-M., Gray, D. G., Chanzy, H. & Maret, G. Chiral nematic suspensions of cellulose crystallites; phase separation and magnetic field orientation. *Liq Cryst* **16**, 127-134, (1994).

42. Battista, O. A. Hydrolysis and crystallization of cellulose. *Industrial & Engineering Chemistry* **42**, 502-507, (1950).
43. Battista, O., Coppick, S., Howsmon, J., Morehead, F. & Sisson, W. A. Level-off degree of polymerization. *Industrial & Engineering Chemistry* **48**, 333-335, (1956).
44. Dong, X. M., Kimura, T., Revol, J.-F. & Gray, D. G. Effects of ionic strength on the isotropic-chiral nematic phase transition of suspensions of cellulose crystallites. *Langmuir* **12**, 2076-2082, (1996).
45. Araki, J., Wada, M., Kuga, S. & Okano, T. Influence of surface charge on viscosity behavior of cellulose microcrystal suspension. *Journal of wood science* **45**, 258-261, (1999).
46. Favier, V., Canova, G., Cavaillé, J., Chanzy, H., Dufresne, A. & Gauthier, C. Nanocomposite materials from latex and cellulose whiskers. *Polymers for Advanced Technologies* **6**, 351-355, (1995).
47. Terech, P., Chazeau, L. & Cavaille, J. A small-angle scattering study of cellulose whiskers in aqueous suspensions. *Macromolecules* **32**, 1872-1875, (1999).
48. Hanley, S. J., Giasson, J., Revol, J.-F. & Gray, D. G. Atomic force microscopy of cellulose microfibrils: comparison with transmission electron microscopy. *Polymer* **33**, 4639-4642, (1992).
49. Hamad, W. On the development and applications of cellulosic nanofibrillar and nanocrystalline materials. *The Canadian Journal of Chemical Engineering* **84**, 513-519, (2006).
50. Cranston, E. D. & Gray, D. G. Morphological and optical characterization of polyelectrolyte multilayers incorporating nanocrystalline cellulose. *Biomacromolecules* **7**, 2522-2530, (2006).
51. Edgar, C. D. & Gray, D. G. Influence of dextran on the phase behavior of suspensions of cellulose nanocrystals. *Macromolecules* **35**, 7400-7406, (2002).
52. Edgar, C. D. & Gray, D. G. Smooth model cellulose I surfaces from nanocrystal suspensions. *Cellulose* **10**, 299-306, (2003).
53. Hasani, M., Cranston, E. D., Westman, G. & Gray, D. G. Cationic surface functionalization of cellulose nanocrystals. *Soft Matter* **4**, 2238-2244, (2008).
54. Lu, P. & Hsieh, Y.-L. Preparation and properties of cellulose nanocrystals: Rods, spheres, and network. *Carbohydrate Polymers* **82**, 329-336, (2010).
55. Shin, Y., Bae, I.-T., Arey, B. W. & Exarhos, G. J. Simple preparation and stabilization of nickel nanocrystals on cellulose nanocrystal. *Mater Lett* **61**, 3215-3217, (2007).
56. Taylor, B. R., Kauzlarich, S. M., Lee, H. W. & Delgado, G. R. Solution synthesis of germanium nanocrystals demonstrating quantum confinement. *Chemistry of materials* **10**, 22-24, (1998).
57. Helbert, W., Nishiyama, Y., Okano, T. & Sugiyama, J. Molecular Imaging of< i> Halocynthia papillosa</i> Cellulose. *Journal of structural biology* **124**, 42-50, (1998).
58. Rao, J. P. & Geckeler, K. E. Polymer nanoparticles: Preparation techniques and size-control parameters. *Progress in Polymer Science* **36**, 887-913, (2011).
59. Mukherjee, S., Sikorski, J. & Woods, H. Electron-microscopy of degraded cellulose fibers. (1952).
60. Mukherjee, S. & Woods, H. X-ray and electron microscope studies of the degradation of cellulose by sulphuric acid. *Biochimica et biophysica acta* **10**, 499-511, (1953).
61. Nishino, T., Takano, K. & Nakamae, K. Elastic modulus of the crystalline regions of cellulose polymorphs. *Journal of Polymer Science Part B: Polymer Physics* **33**, 1647-1651, (1995).
62. Chazeau, L., Cavaille, J., Canova, G., Dendievel, R. & Boutherin, B. Viscoelastic properties of plasticized PVC reinforced with cellulose whiskers. *J Appl Polym Sci* **71**, 1797-1808, (1999).
63. Helbert, W., Cavaille, J. & Dufresne, A. Thermoplastic nanocomposites filled with wheat straw cellulose whiskers. Part I: processing and mechanical behavior. *Polymer Composites* **17**, 604-611, (1996).
64. Ruiz, M. M., Cavaille, J. Y., Dufresne, A., Graillat, C. & Gérard, J. F. in *Macromolecular Symposia.* 211-222 (Wiley Online Library).
65. Angles, M. N. & Dufresne, A. Plasticized starch/tunicin whiskers nanocomposites. 1. Structural analysis. *Macromolecules* **33**, 8344-8353, (2000).
66. Dubief, D., Samain, E. & Dufresne, A. Polysaccharide microcrystals reinforced amorphous poly (β-hydroxyoctanoate) nanocomposite materials. *Macromolecules* **32**, 5765-5771, (1999).
67. Dufresne, A. Interfacial phenomena in nanocomposites based on polysaccharide nanocrystals. *Composite Interfaces* **10**, 369-387, (2003).
68. Dufresne, A., Kellerhals, M. B. & Witholt, B. Transcrystallization in Mcl-PHAs/cellulose whiskers composites. *Macromolecules* **32**, 7396-7401, (1999).

69. Noishiki, Y., Nishiyama, Y., Wada, M., Kuga, S. & Magoshi, J. Mechanical properties of silk fibroin–microcrystalline cellulose composite films. *J Appl Polym Sci* **86**, 3425-3429, (2002).
70. Morandi, G., Heath, L. & Thielemans, W. Cellulose nanocrystals grafted with polystyrene chains through surface-initiated atom transfer radical polymerization (SI-ATRP). *Langmuir* **25**, 8280-8286, (2009).
71. Gopalan Nair, K., Dufresne, A., Gandini, A. & Belgacem, M. N. Crab shell chitin whiskers reinforced natural rubber nanocomposites. 3. Effect of chemical modification of chitin whiskers. *Biomacromolecules* **4**, 1835-1842, (2003).
72. Gopalan Nair, K. & Dufresne, A. Crab shell chitin whisker reinforced natural rubber nanocomposites. 1. Processing and swelling behavior. *Biomacromolecules* **4**, 657-665, (2003).
73. Nair, K. G. & Dufresne, A. Crab shell chitin whisker reinforced natural rubber nanocomposites. 2. Mechanical behavior. *BIOMACROMOLECULES-WASHINGTON-* **4**, 666-674, (2003).
74. Capadona, J. R., Shanmuganathan, K., Tyler, D. J., Rowan, S. J. & Weder, C. Stimuli-responsive polymer nanocomposites inspired by the sea cucumber dermis. *Science* **319**, 1370-1374, (2008).
75. Liu, H., Liu, D., Yao, F. & Wu, Q. Fabrication and properties of transparent polymethylmethacrylate/cellulose nanocrystals composites. *Bioresource technology* **101**, 5685-5692, (2010).
76. Klemm, D., Philpp, B., Heinze, T., Heinze, U. & Wagenknecht, W. *Comprehensive cellulose chemistry. Volume 1: Fundamentals and analytical methods*. 130-155 (Wiley-VCH Verlag GmbH, 1998).
77. Klemm, D., Philpp, B., Heinze, T., Heinze, U. & Wagenknecht, W. *Comprehensive cellulose chemistry. Volume 1: Fundamentals and analytical methods*. 31-82 (Wiley-VCH Verlag GmbH, 1998).
78. Klemm, D., Philipp, B., Heinze, T., Heinze, U. & Wagenknecht, W. *Comprehensive cellulose chemistry: v. 2: functionalization of cellulose: functionalization of cellulose*. (Wiley-VCH, Weinheim, 1998).
79. Dumitriu, S. *Polysaccharides: structural diversity and functional versatility*. (CRC Press, 2005).
80. French, A. D., Bertoniere, N. R., Brown, R. M., Chanzy, H., Gray, D., Hattori, K. & Glasser, W., (John Wiley & Sons, Inc., 2002).
81. Wertz, J.-L., Bédué, O. & Mercier, J. P. *Cellulose science and technology*. (Efpl Press, 2010).
82. French, A. D., Bertoniere, N. R., Brown, R. M., Chanzy, H. & Gray, D., (John Wiley & Sons, Inc., 2002).
83. http://www.cefic.be/Templates/shwAssocDetails.asp?NID=5&HID=27&ID=50.
84. Klemm, D., Philpp, B., Heinze, T., Heinze, U. & Wagenknecht, W. *Comprehensive cellulose chemistry. Volume 1: Fundamentals and analytical methods*. (Wiley-VCH Verlag GmbH, 1998).
85. Kittel, C. & McEuen, P. *Introduction to solid state physics*. Vol. 7 (Wiley New York, 1996).
86. Zallen, R. *The physics of amorphous solids*. (Wiley-VCH, 2008).
87. Lehmann, O. On flowing crystals. *Zeitschrift für Physikalische Chemie* **4**, 462, (1889).
88. Reinitzer, F. Beiträge zur kenntniss des cholesterins. *Monatshefte für Chemie/Chemical Monthly* **9**, 421-441, (1888).
89. de Gennes, P. G. *The physics of liquid crystals*. (Clarendon Press, 1974).
90. Singh, S. & Dunmur, D. A. *Liquid crystals: fundamentals*. (World Scientific Publishing Company Incorporated, 2002).
91. Pincus, P. Magnetic Properties of Liquid Crystals. *Journal of Applied Physics* **41**, 974-979, (1970).
92. Khoo, I.-C. *Liquid crystals*. Vol. 64 (Wiley-Interscience, 2007).
93. Friedel, G. The mesomorphic states of matter. *Ann. Phys* **18**, 273-474, (1922).
94. Oseen, C. The theory of liquid crystals. *Transactions of the Faraday Society* **29**, 883-899, (1933).
95. de Gennes, P. & Prost, J. *The Physics of L iquid Crystals*. (Oxford University Press, Oxford, 1993).
96. Ornstein, L. & Kast, W. New arguments for the Swarm theory of liquid crystals. *Transactions of the Faraday Society* **29**, 931-944, (1933).
97. http://barrett-group.mcgill.ca/teaching/liquid_crystal/LC02.htm.
98. de Gennes, P.-G., Prost, J. & Pelcovits, R. The physics of liquid crystals. *Physics Today* **48**, 70, (1995).

99. de Gennes, P. Short range order effects in the isotropic phase of nematics and cholesterics. *Mol Cryst Liq Cryst* **12**, 193-214, (1971).
100. Landau, L. D. & Lifshitz, E. M. *Statistical Physics*. (Elsevier Science, 1996).
101. Sheng, P. & Priestley, E. B. The Landau-de Gennes Theory of Liquid Crystal Phase Transitions. 143-201 (Springer US, 1976).143-201.
102. Gramsbergen, E. F., Longa, L. & de Jeu, W. H. Landau theory of the nematic-isotropic phase transition. *Physics Reports* **135**, 195-257, (1986).
103. Vertogen, G. & Jeu, W. H. *Thermotropic liquid crystals, fundamentals*. (Springer-Verlag, 1988).
104. Mauguin, C. Sur les cristaux liquides de Lehmann. *Bull. Soc. Fr. Mineral* **34**, 71-117, (1911).
105. Brinkman, W. F. & Cladis, P. E. Defects in liquid crystals. *Physics Today* **35**, 48, (1982).
106. Kléman, M. Defects in liquid crystals. *Reports on Progress in Physics* **52**, 555, (1989).
107. Kléman, M. *Points, lines, and walls: in liquid crystals, magnetic systems, and various ordered media*. (J. Wiley, 1983).
108. Chandrasekhar, S. & Ranganath, G. The structure and energetics of defects in liquid crystals. *Adv Phys* **35**, 507-596, (1986).
109. Dierking, I. *Textures of Liquid Crystals*. (John Wiley & Sons Australia, Limited, 2003).
110. Wright, D. C. & Mermin, N. D. Crystalline liquids: the blue phases. *Rev Mod Phys* **61**, 385, (1989).
111. Goodby, J. W. Twist grain boundary (TGB) phases. *Structure and bonding*, 83-148, (1999).
112. Kralj, S., Zumer, S. & Allender, D. W. Nematic-Isotropic Phase-Transition in a Liquid-Crystal Droplet. *Phys Rev A* **43**, 2943-2954, (1991).
113. Suzuki, K. Liquid crystal display device. US20040183987, (1991).
114. Terentjev, E. Liquid crystals: Interplay of topologies. *Nat Mater* **12**, 187-189, (2013).
115. Oswald, P. & Pieranski, P. *Nematic and Cholesteric Liquid Crystals: Concepts and Physical Properties Illustrated by Experiments*. (Taylor & Francis, 2006).
116. Bouligand, Y. Recherches sur les textures des états mésomorphes. 3. Les plages à éventails dans les cholestériques. *J Phys-Paris* **34**, 603-614, (1973).
117. Revol, J.-F. On the cross-sectional shape of cellulose crystallites in Valonia ventricosa. *Carbohydrate Polymers* **2**, 123-134, (1982).
118. Revol, J. F., Bradford, H., Giasson, J., Marchessault, R. & Gray, D. Helicoidal self-ordering of cellulose microfibrils in aqueous suspension. *International journal of biological macromolecules* **14**, 170-172, (1992).
119. Dong, X. M., Revol, J.-f. & Gray, D. G. Effect of microcrystallite preparation conditions on the formation of colloid crystals of cellulose. *Cellulose* **5**, 19-32, (1998).
120. Podsiadlo, P., Sui, L., Elkasabi, Y., Burgardt, P., Lee, J., Miryala, A., Kusumaatmaja, W., Carman, M. R., Shtein, M. & Kieffer, J. Layer-by-layer assembled films of cellulose nanowires with antireflective properties. *Langmuir* **23**, 7901-7906, (2007).
121. Yoshiharu, N., Shigenori, K., Masahisa, W. & Takeshi, O. Cellulose microcrystal film of high uniaxial orientation. *Macromolecules* **30**, 6395-6397, (1997).
122. Roman, M. & Gray, D. G. Parabolic focal conics in self-assembled solid films of cellulose nanocrystals. *Langmuir* **21**, 5555-5561, (2005).
123. Li, J., Revol, J., Naranjo, E. & Marchessault, R. Effect of electrostatic interaction on phase separation behavior of chitin crystallite suspensions. *International journal of biological macromolecules* **18**, 177-187, (1996).
124. Shopsowitz, K. E., Qi, H., Hamad, W. Y. & MacLachlan, M. J. Free-standing mesoporous silica films with tunable chiral nematic structures. *Nature* **468**, 422-425, (2010).
125. Gray, D. Chiral nematic ordering of polysaccharides. *Carbohydrate Polymers* **25**, 277-284, (1994).
126. Werbowyj, R. S. & Gray, D. G. Liquid-Crystalline Structure in Aqueous Hydroxypropyl Cellulose Solutions. *Mol Cryst Liq Cryst* **34**, 97-103, (1976).
127. Gray, D. G. in *J. Appl. Polym. Sci.: Appl. Polym. Symp.;(United States).* (McGill Univ., Montreal, Quebec).
128. Werbowyj, R. S. & Gray, D. G. Ordered phase formation in concentrated hydroxpropylcellulose solutions. *Macromolecules* **13**, 69-73, (1980).

129. Werbowyj, R. S. & Gray, D. G. Liquid crystalline structure in aqueous hydroxypropyl cellulose solutions. *Mol Cryst Liq Cryst* **34**, 97-103, (1976).
130. Werbowyj, R. S. & Gray, D. G. Ordered Phase Formation in Concentrated Hydroxypropylcellulose Solutions. *Macromolecules* **13**, 69-73, (1980).
131. Fortin, S. & Charlet, G. Phase diagram of aqueous solutions of (hydroxypropyl) cellulose. *Macromolecules* **22**, 2286-2292, (1989).
132. Streletzky, K. A., John, T. & Mohieddine, R. Spectral time moment analysis of microgel structure and dynamics. *J Polym Sci Pol Phys* **46**, 771-781, (2008).
133. Werbowyj, R. S. & Gray, D. G. Optical-Properties of (Hydroxypropyl)Cellulose Liquid-Crystals - Cholesteric Pitch and Polymer Concentration. *Macromolecules* **17**, 1512-1520, (1984).
134. Dadmun, M. D. & Han, C. C. A Neutron-Scattering Study of the Orientation of a Liquid-Crystalline Polymer by Shear-Flow. *Macromolecules* **27**, 7522-7532, (1994).
135. Guido, S. & Grizzuti, N. Phase-Separation Effects in the Rheology of Aqueous-Solutions of Hydroxypropylcellulose. *Rheol Acta* **34**, 137-146, (1995).
136. Hongladarom, K., Secakusuma, V. & Burghardt, W. R. Relation between Molecular-Orientation and Rheology in Lyotropic Hydroxypropylcellulose Solutions. *J Rheol* **38**, 1505-1523, (1994).
137. Walker, L. & Wagner, N. Rheology of region I flow in a lyotropic liquid-crystal polymer: The effects of defect texture. *J Rheol* **38**, 1525-1548, (1994).
138. Onogi, S. & Asada, T. Rheology and rheo-optics of polymer liquid crystals. *Rheology* **1**, 127-147, (1980).
139. Larson, R. Arrested tumbling in shearing flows of liquid-crystal polymers. *Macromolecules* **23**, 3983-3992, (1990).
140. Larson, R. G. & Ottinger, H. C. Effect of Molecular Elasticity on out-of-Plane Orientations in Shearing Flows of Liquid-Crystalline Polymers. *Macromolecules* **24**, 6270-6282, (1991).
141. Immaneni, A., Kuba, A. & McHugh, A. Effects of temperature and solvent on the rheo-optical behavior of hydroxypropylcellulose solutions. *Macromolecules* **30**, 4613-4618, (1997).
142. Barthlott, W. & Neinhuis, C. Purity of the sacred lotus, or escape from contamination in biological surfaces. *Planta* **202**, 1-8, (1997).
143. Li, H. Y., Ke, Y. C. & Hu, Y. L. Polymer nanofibers prepared by template melt extrusion. *J Appl Polym Sci* **99**, 1018-1023, (2006).
144. Yang, Z. & Xu, B. Supramolecular hydrogels based on biofunctional nanofibers of self-assembled small molecules. *J Mater Chem* **17**, 2385-2393, (2007).
145. Woo, K. M., Chen, V. J. & Ma, P. X. Nano-fibrous scaffolding architecture selectively enhances protein adsorption contributing to cell attachment. *J Biomed Mater Res A* **67A**, 531-537, (2003).
146. Ellison, C. J., Phatak, A., Giles, D. W., Macosko, C. W. & Bates, F. S. Melt blown nanofibers: Fiber diameter distributions and onset of fiber breakup (vol 48, pg 3306, 2007). *Polymer* **48**, 6180-6180, (2007).
147. Gu, B. K., Shin, M. K., Sohn, K. W., Kim, S. I., Kim, S. J., Kim, S. K., Lee, H. & Park, J. S. Direct fabrication of twisted nanofibers by electrospinning. *Appl Phys Lett* **90**, 263902-263903, (2007).
148. Kim, G. & Kim, W. Formation of oriented nanofibers using electrospinning. *Appl Phys Lett* **88**, (2006).
149. Panda, P. K. & Ramakrishna, S. Electrospinning of alumina nanofibers using different precursors. *J Mater Sci* **42**, 2189-2193, (2007).
150. Teo, W. E. & Ramakrishna, S. A review on electrospinning design and nanofiber assemblies. *Nanotechnology* **17**, R89-R106, (2006).
151. Li, D. & Xia, Y. N. Electrospinning of nanofibers: Reinventing the wheel? *Adv Mater* **16**, 1151-1170, (2004).
152. Greiner, A. & Wendorff, J. H. Electrospinning: A fascinating method for the preparation of ultrathin fibers. *Angew Chem Int Edit* **46**, 5670-5703, (2007).
153. A, F. Process and apparatus for preparing artificial threads. (1934).
154. Reneker, D. H. & Chun, I. Nanometre diameter fibers of polymer, produced by electrospinning. *Nanotechnology* **7**, 216-223, (1996).
155. Godinho, M. H., Canejo, J. P., Feio, G. & Terentjev, E. M. Self-winding of helices in plant tendrils and cellulose liquid crystal fibers. *Soft Matter* **6**, 5965-5970, (2010).

156. Canejo, J. P., Borges, J. P., Godinho, M. H., Brogueira, P., Teixeira, P. I. & Terentjev, E. M. Helical Twisting of Electrospun Liquid Crystalline Cellulose Micro‐and Nanofibers. *Adv Mater* **20**, 4821-4825, (2008).
157. Godinho, M., Canejo, J., Feio, G. & Terentjev, E. Self-winding of helices in plant tendrils and cellulose liquid crystal fibers. *Soft Matter* **6**, 5965-5970, (2010).
158. Godinho, M., Canejo, J., Pinto, L., Borges, J. & Teixeira, P. How to mimic the shapes of plant tendrils on the nano and microscale: spirals and helices of electrospun liquid crystalline cellulose derivatives. *Soft Matter* **5**, 2772-2776, (2009).
159. Mori, N., Morimoto, M. & Nakamura, K. Hydroxypropylcellulose films as alignment layers for liquid crystals. *Macromolecules* **32**, 1488-1492, (1999).
160. Mori, N., Morimoto, M. & Nakamura, K. Cellulose Films as Alignment Layers for Liquid Crystals: Application of Flow‐Induced Molecular Orientation. *Adv Mater* **11**, 1049-1051, (1999).
161. Sena, C., Godinho, M., Oliveira, C. L. P. & Figueiredo Neto, A. Liquid crystalline cellulosic elastomers: free standing anisotropic films under stretching. *Cellulose* **18**, 1151-1163, (2011).
162. Godinho, M., Fonseca, J., Ribeiro, A., Melo, L. & Brogueira, P. Atomic force microscopy study of hydroxypropylcellulose films prepared from liquid crystalline aqueous solutions. *Macromolecules* **35**, 5932-5936, (2002).
163. Patnaik, S. S., Bunning, T. J., Adams, W. W., Wang, J. & Labes, M. Atomic force microscopy and high-resolution scanning electron microscopy study of the banded surface morphology of hydroxypropyl cellulose thin films. *Macromolecules* **28**, 393-395, (1995).
164. Aharoni, S. M. Rigid backbone polymers. 2. Polyisocyanates and their liquid-crystal behavior. *Macromolecules* **12**, 94-103, (1979).
165. Navard, P. & Zachariades, A. Optical properties of a shear‐deformed thermotropic cellulose derivative. *Journal of Polymer Science Part B: Polymer Physics* **25**, 1089-1098, (1987).
166. Nishio, Y., Yamane, T. & Takahashi, T. Morphological studies of liquid‐crystalline cellulose derivatives. I. Liquid‐crystalline characteristics of hydroxypropyl cellulose in 2‐hydroxyethyl methacrylate solutions and in polymer composites prepared by bulk polymerization. *Journal of Polymer Science: Polymer Physics Edition* **23**, 1043-1052, (1985).
167. Wang, J., Bhattacharya, S. & Labes, M. Solvent evaporation induced torsad texture of sheared liquid-crystalline polymers. *Macromolecules* **24**, 4942-4947, (1991).
168. Zhao, C., Zhang, G., Cai, B. & Xu, M. Solvent composition dependence of band morphology in sheared lyotropic ethylcellulose liquid crystals. *Macromol Chem Physic* **199**, 1485-1488, (1998).
169. Wang, J. & Labes, M. Control of the anisotropic mechanical properties of liquid crystal polymer films by variations in their banded texture. *Macromolecules* **25**, 5790-5793, (1992).
170. Zentel, R., Müiller, M. & Keller, H. Solid opalescent films originating from urethanes of cellulose. *Adv Mater* **9**, 159-162, (1997).
171. Kitzerow, H.-S. Polymer-dispersed liquid crystals from the nematic curvilinear aligned phase to ferroelectric films. *Liq Cryst* **16**, 1-31, (1994).
172. Godinho, M., Martins, A. & Figueirinhas, J. Novel PDLC type display based on cellulose derivatives. *Liq Cryst* **20**, 373-376, (1996).
173. Almeida, P. L., Kundu, S., Beja, D., Fonseca, J., Figueirinhas, J. & Godinho, M. Deformation of isotropic and anisotropic liquid droplets dispersed in a cellulose liquid crystalline derivative. *Cellulose* **16**, 427-434, (2009).
174. Fergason, J. L. in *SID Int. Symp. Dig.* 268-270.
175. Doane, J. W., Vaz, N. A., Wu, B. G. & Zumer, S. Field Controlled Light-Scattering from Nematic Microdroplets. *Appl Phys Lett* **48**, 269-271, (1986).
176. Wu, B. G., Erdmann, J. H. & Doane, J. W. Response times and voltages for PDLC light shutters. *Liq Cryst* **5**, 1453-1465, (1989).
177. Sheraw, C., Zhou, L., Huang, J., Gundlach, D., Jackson, T., Kane, M., Hill, I., Hammond, M., Campi, J. & Greening, B. Organic thin-film transistor-driven polymer-dispersed liquid crystal displays on flexible polymeric substrates. *Appl Phys Lett* **80**, 1088-1090, (2002).
178. Xiong, G. R., Han, G. Z., Sun, C., Xu, H., Wei, H. & Gu, Z. Z. Phototunable Microlens Array Based on Polymer Dispersed Liquid Crystals. *Advanced Functional Materials* **19**, 1082-1086, (2009).

179. Liu, Y., Sun, X., Elim, H. & Ji, W. Effect of liquid crystal concentration on the lasing properties of dye-doped holographic polymer-dispersed liquid crystal transmission gratings. *Appl Phys Lett* **90**, 011109-011109-011103, (2007).
180. Liu, Y. & Sun, X. Electrically switchable computer-generated hologram recorded in polymer-dispersed liquid crystals. *Appl Phys Lett* **90**, 191118-191118-191113, (2007).
181. Almeida, P. L., Kundu, S., Borges, J., Godinho, M. & Figueirinhas, J. Electro-optical light scattering shutter using electrospun cellulose-based nano-and microfibers. *Appl Phys Lett* **95**, 043501-043501-043503, (2009).
182. Vshivkov, S. A. & Rusinova, E. V. Liquid crystal phase transitions and rheological properties of cellulose ethers. *Russ J Appl Chem+* **84**, 1830-1835, (2011).
183. Godinho, M. H., van der Klink, J. J. & Martins, A. F. Shear-history dependent 'equilibrium' states of liquid-crystalline hydroxypropylcellulose solutions detected by rheo-nuclear magnetic resonance. *J Phys-Condens Mat* **15**, 5461-5468, (2003).
184. Burghardt, W. R. Molecular orientation and rheology in sheared lyotropic liquid crystalline polymers. *Macromol Chem Physic* **199**, 471-488, (1998).
185. Ludwig, R., Weinhold, F. & Farrar, T. Experimental and theoretical determination of the temperature dependence of deuteron and oxygen quadrupole coupling constants of liquid water. *The Journal of Chemical Physics* **103**, 6941-6950, (1995).
186. Fernandes, S. N., Geng, Y., Vignolini, S., Glover, B. J., Trindade, A. C., Canejo, J. P., Almeida, P. L., Brogueira, P. & Godinho, M. H. Structural Color and Iridescence in Transparent Sheared Cellulosic Films. *Macromol Chem Physic* **214**, 25-32, (2013).
187. Whitney, H. M., Kolle, M., Andrew, P., Chittka, L., Steiner, U. & Glover, B. J. Floral iridescence, produced by diffractive optics, acts as a cue for animal pollinators. *Science* **323**, 130-133, (2009).
188. Glover, B. J. & Whitney, H. M. Structural color and iridescence in plants: the poorly studied relations of pigment colour. *Annals of botany* **105**, 505-511, (2010).
189. Vignolini, S., Thomas, M. M., Kolle, M., Wenzel, T., Rowland, A., Rudall, P. J., Baumberg, J. J., Glover, B. J. & Steiner, U. Directional scattering from the glossy flower of Ranunculus: how the buttercup lights up your chin. *Journal of The Royal Society Interface* **9**, 1295-1301, (2012).
190. Hébant, C. & Lee, D. W. Ultrastructural basis and developmental control of blue iridescence in Selaginella leaves. *American Journal of Botany*, 216-219, (1984).
191. Thomas, A. & Antonietti, M. Silica Nanocasting of Simple Cellulose Derivatives: Towards Chiral Pore Systems with Long‐Range Order and Chiral Optical Coatings. *Advanced Functional Materials* **13**, 763-766, (2003).
192. de Vries, H. Rotatory power and other optical properties of certain liquid crystals. *Acta Crystallographica* **4**, 219-226, (1951).
193. Kimura, H., Hosino, M. & Nakano, H. Statistical theory of cholesteric ordering in hard-rod fluids and liquid crystalline properties of polypeptide solutions. *J. PHYS. SOC. JAPAN.* **51**, 1584-1590, (1982).
194. Onogi, Y., White, J. L. & Fellers, J. F. Structural investigations of polymer liquid‐crystalline solutions: Aromatic polyamides, hydroxy propyl cellulose, and poly (γ‐benzyl‐L‐glutamate). *Journal of Polymer Science: Polymer Physics Edition* **18**, 663-682, (2003).
195. Kisst, G. & Porter, R. Rheo-optical studies of liquid crystalline solutions of helical polypeptides. *Mol Cryst Liq Cryst* **60**, 267-280, (1980).
196. Ernst, B. & Navard, P. Band textures in mesomorphic (hydroxypropyl) cellulose solutions. *Macromolecules* **22**, 1419-1422, (1989).
197. Godinho, M., Filip, D., Costa, I., Carvalho, A. L., Figueirinhas, J. & Terentjev, E. Liquid crystalline cellulose derivative elastomer films under uniaxial strain. *Cellulose* **16**, 199-205, (2009).
198. Mitov, M. & Dessaud, N. Going beyond the reflectance limit of cholesteric liquid crystals. *Nat Mater* **5**, 361-364, (2006).
199. Bouligand, Y. Liquid crystals and their analogs in biological systems. *Solid State Physics, supplement* **14**, (1978).
200. http://www.itp.uni-hannover.del-zawischa/ITP/origins.html.
201. Reis, D., Vian, B. & Roland, J. C. Cellulose-glucuronoxylans and plant cell wallstructure. *Micron* **25**, 171-187, (1994).

202. Godinho, M. H., Filip, D., Costa, I., Carvalho, A. L., Figueirinhas, J. L. & Terentjev, E. M. Liquid crystalline cellulose derivative elastomer films under uniaxial strain. *Cellulose* **16**, 199-205, (2009).
203. Warner, M. & Terentjev, E. M. *Liquid crystal elastomers*. (Oxford University Press, 2007).
204. Favier, V., Canova, G., Cavaillé, J., Chanzy, H., Dufresne, A. & Gauthier, C. Nanocomposite materials from latex and cellulose whiskers. *Polymers for Advanced Technologies* **6**, 351-355, (2003).
205. Mertens, J., Rogero, C., Calleja, M., Ramos, D., Martin-Gago, J. A., Briones, C. & Tamayo, J. Label-free detection of DNA hybridization based on hydration-induced tension in nucleic acid films. *Nat Nanotechnol* **3**, 301-307, (2008).
206. Harris, K. D., Bastiaansen, C. W. M. & Broer, D. J. A glassy bending-mode polymeric actuator which deforms in response to solvent polarity. *Macromolecular Rapid Communications* **27**, 1323-1329, (2006).
207. Abraham, N. & Palffy-Muhoray, P. A dunking bird of the second kind. *Am J Phys* **72**, 782-785, (2004).
208. Steinberg, I. Z., Oplatka, A. & Katchalsky.A. Mechanochemical Engines. *Nature* **210**, 568-571, (1966).
209. Lavrentovich, O. D. Topological defects in dispersed liquid crystals, or words and worlds around liquid crystal drops. *Liq Cryst* **24**, 117-125, (1998).
210. Candau, S., Leroy, P. & Debeauva.F. Magnetic-Field Effects in Nematic and Cholesteric Droplets Suspended in an Isotropic Liquid. *Mol Cryst Liq Cryst* **23**, 283-297, (1973).
211. Jacob, G. A Novel Crystal-Growth Method for Gaas - the Liquid Encapsulated Kyropoulos Method. *J Cryst Growth* **58**, 455-459, (1982).
212. Ondriscrawford, R., Boyko, E. P., Wagner, B. G., Erdmann, J. H., Zumer, S. & Doane, J. W. Microscope Textures of Nematic Droplets in Polymer Dispersed Liquid-Crystals. *Journal of Applied Physics* **69**, 6380-6386, (1991).
213. Lopez-Leon, T. & Fernandez-Nieves, A. Drops and shells of liquid crystal. *Colloid Polym Sci* **289**, 345-359, (2011).
214. Alexander, G. P., Chen, B. G. G., Matsumoto, E. A. & Kamien, R. D. Colloquium: Disclination loops, point defects, and all that in nematic liquid crystals (vol 84, pg 497, 2012). *Rev Mod Phys* **84**, (2012).
215. Volovik, G. E. & Lavrentovich, O. D. The Topological Dynamics of Defects - Boojums in Nematic Drops. *Zh Eksp Teor Fiz+* **85**, 1997-2010, (1983).
216. Chen, X. M., Hamlington, B. D. & Shen, A. Q. Isotropic-to-nematic phase transition in a liquid-crystal droplet. *Langmuir* **24**, 541-546, (2008).
217. Davies, J. B., Day, S., DiPasquale, F. & Fernandez, F. A. Finite-element modelling in 2-D of nematic liquid crystal structures. *Electron Lett* **32**, 582-583, (1996).
218. Di Pasquale, F., Fernandez, F. A., Day, S. E. & Davies, J. B. Two-dimensional finite-element modeling of nematic liquid crystal devices for optical communications and displays. *Ieee J Sel Top Quant* **2**, 128-134, (1996).
219. Dridi, M. & Vial, A. FDTD modelling of gold nanoparticle pairs in a nematic liquid crystal cell. *J Phys D Appl Phys* **43**, (2010).
220. Dridi, M. & Vial, A. FDTD Modeling of Gold Nanoparticles in a Nematic Liquid Crystal: Quantitative and Qualitative Analysis of the Spectral Tunability. *J Phys Chem C* **114**, 9541-9545, (2010).
221. Kirkman, N. T., Stirner, T. & Hagston, W. E. Continuum modelling of hybrid-aligned nematic liquid crystal cells: optical response and flexoelectricity-induced voltage shift. *Liq Cryst* **30**, 1115-1122, (2003).
222. Liu, C., Shen, J. & Yang, X. F. Dynamics of defect motion in nematic liquid crystal flow: Modeling and numerical simulation. *Commun Comput Phys* **2**, 1184-1198, (2007).
223. Ong, H. L. Modeling of Guest-Host and General Twisted-Nematic Liquid-Crystal Displays. *P Sid* **29**, 161-165, (1988).
224. Pawlik, G., Mitus, A. C. & Miniewicz, A. Modelling of Enhanced Photoinduced Reorientation of Nematic Liquid Crystal Molecules in Twisted Geometry: Monte Carlo Approach. *Mol Cryst Liq Cryst* **554**, 56-64, (2012).

225. Xu, F. & Crooker, P. P. Chiral nematic droplets with parallel surface anchoring. *Phys Rev E* **56**, 6853-6860, (1997).
226. Ravnik, M. & Zumer, S. Landau-de Gennes modelling of nematic liquid crystal colloids. *Liq Cryst* **36**, 1201-1214, (2009).
227. David Sec, T. P., Miha Ravnik and Slobodan Zumer. Geometrical frustration of chiral ordering in cholesteric droplets. *Soft Matter*, 1-8, (2012).
228. Bodnar, V. G., Lavrentovich, O. D. & Pergamenshchik, V. M. The Threshold for the Hedgehog - Ring Structural Transition in Nematic Drops in an Alternating Electric-Field. *Zh Eksp Teor Fiz+* **101**, 111-125, (1992).
229. Peccianti, M., Conti, C., Assanto, G., De Luca, A. & Umeton, C. Routing of anisotropic spatial solitons and modulational instability in liquid crystals. *Nature* **432**, 733-737, (2004).
230. Assanto, G. & Peccianti, M. Spatial solitons in nematic liquid crystals. *Ieee J Quantum Elect* **39**, 13-21, (2003).
231. Assanto, G., Fratalocchi, A. & Peccianti, M. Spatial solitons in nematic liquid crystals: from bulk to discrete. *Opt Express* **15**, 5248-5259, (2007).
232. Assanto, G., Peccianti, M., Brzdakiewicz, K. A., De Luca, A. & Umeton, C. Nonlinear wave propagation and spatial solitons in nematic liquid crystals. *J Nonlinear Opt Phys* **12**, 123-134, (2003).
233. Assanto, G., Peccianti, M. & Conti, C. Light-confinement, accessible spatial solitons and their interactions via nonlocal reorientation in nematic liquid crystals. *Ieee Leos Ann Mtg*, 211-212, (2002).
234. Assanto, G., Peccianti, M. & Conti, C. Spatial optical solitons in bulk nematic liquid crystals. *Acta Phys Pol A* **103**, 161-167, (2003).
235. Assanto, G., Peccianti, M., De Rossi, A., Umeton, C. & Khoo, I. C. Spatial solitons in voltage-biased nematic liquid crystals. *Leos 2000 - Ieee Annual Meeting Conference Proceedings, Vols. 1 & 2*, 195-196, (2000).
236. Assanto, G., Peccianti, M., Umeton, C., De Luca, A. & Khoo, I. C. Coherent and incoherent spatial solitons in bulk nematic liquid crystals. *Mol Cryst Liq Cryst* **375**, 617-629, (2002).
237. Peccianti, M. & Assanto, G. Signal readdressing by steering of spatial solitons in bulk nematic liquid crystals. *Opt Lett* **26**, 1690-1692, (2001).
238. Peccianti, M., DeLuca, A. & Assanto, G. Incoherent spatial solitons in nematic liquid crystals. *Icton 2001: 3rd International Conference on Transparent Optical Networks, Conference Proceedings*, 147-150, (2001).
239. Peccianti, M., Umeton, C., Khoo, I. C., deRossi, A. & Assanto, G. Two-dimensional spatial, solitons in nematic liquid crystals. *P Soc Photo-Opt Ins* **4271**, 372-379, (2001).
240. Piccardi, A., Alberucci, A., Buchnev, O., Kaczmarek, M., Khoo, I. C. & Assanto, G. Frequency-controlled deflection of spatial solitons in nematic liquid crystals. *Appl Phys Lett* **101**, (2012).
241. Trebin, H. R. The Topology of Nonuniform Media in Condensed Matter Physics. *Adv Phys* **31**, 195-254, (1982).
242. Kurik, M. V. & Lavrentovich, O. D. Defects in Liquid-Crystals - Homotopy-Theory and Experimental Investigations. *Usp Fiz Nauk+* **154**, 381-431, (1988).
243. Skyrme, T. H. R. The effective nuclear potential. *Nuclear physics* **9**, 556-569, (1962).
244. Williams, D. W. G. Spinning particle-like solitons in superfluid 3He-B. *Z. Phys. B-Condensed Matter* **88**, 265-270, (1992).
245. Jain, S. C. R., D. K. . Electro‐optic response of polymer dispersed liquid‐crystal films. *Journal of Applied Physics* **70**, (1991).
246. Erdmann, J. H., Zumer, S. & Doane, J. W. Configuration Transition in a Nematic Liquid-Crystal Confined to a Small Spherical Cavity. *Phys Rev Lett* **64**, 1907-1910, (1990).
247. Pishnyak, O., Sato, S. & Lavrentovich, O. D. Electrically tunable lens based on a dual-frequency nematic liquid crystal. *Appl Optics* **45**, 4576-4582, (2006).
248. Penterman, R., Klink, S. L., de Koning, H., Nisato, G. & Broer, D. J. Single-substrate liquid-crystal displays by photo-enforced stratification. *Nature* **417**, 55-58, (2002).
249. Humar, M., Ravnik, M., Pajk, S. & Musevic, I. Electrically tunable liquid crystal optical microresonators. *Nat Photonics* **3**, 595-600, (2009).
250. Humar, M. & Musevic, I. 3D microlasers from self-assembled cholesteric liquid-crystal microdroplets. *Opt Express* **18**, 26995-27003, (2010).

251. Moreira, M. F., Carvalho, I. C. S., Cao, W., Bailey, C., Taheri, B. & Palffy-Muhoray, P. Cholesteric liquid-crystal laser as an optic fiber-based temperature sensor. *Appl Phys Lett* **85**, 2691-2693, (2004).
252. Almeida, P. L., Kundu, S., Borges, J. P., Godinho, M. H. & Figueirinhas, J. L. Electro-optical light scattering shutter using electrospun cellulose-based nano- and microfibers. *Appl Phys Lett* **95**, (2009).
253. Lin, I. H., Miller, D. S., Bertics, P. J., Murphy, C. J., de Pablo, J. J. & Abbott, N. L. Endotoxin-Induced Structural Transformations in Liquid Crystalline Droplets. *Science* **332**, 1297-1300, (2011).
254. Pairam, E. & Fernandez-Nieves, A. Generation and Stability of Toroidal Droplets in a Viscous Liquid. *Phys Rev Lett* **102**, (2009).
255. Renardy, Y., Popinet, S., Duchemin, L., Renardy, M., Zaleski, S., Josserand, C., Drumright-Clarke, M. A., Richard, D., Clanet, C. & Quere, D. Pyramidal and toroidal water drops after impact on a solid surface. *J Fluid Mech* **484**, 69-83, (2003).
256. AV Kovalchuk, M. K., OD Lavrentovich. Encapsulated nematic liquid crystals: a new class of display units. *Zarubezhnaja radioelektronika* **94**, (1988).
257. Gray, G. & McDonnell, D. Synthesis and liquid crystal properties of chiral alkyl-cyano-biphenyls (and-p-terphenyls) and of some related chiral compounds derived from biphenyl. *Mol Cryst Liq Cryst* **37**, 189-211, (1976).
258. Sebastião, P., Gradišek, A., Pinto, L., Apih, T., Godinho, M. & Vilfan, M. Fast Field-Cycling NMR Relaxometry Study of Chiral and Nonchiral Nematic Liquid Crystals. *The Journal of Physical Chemistry B* **115**, 14348-14358, (2011).
259. Rakhmanov, A. N. & Shmalgauzen, V. I. Modeling of the Dynamics of Parameters of Nematic Liquid-Crystal Layers. *Kvantovaya Elektron+* **21**, 878-882, (1994).
260. Singh, H. K., Jain, S. C. & Chandra, S. Computer Modeling of the Director Configuration in a Supertwist Nematic Liquid-Crystal Cell. *Liq Cryst* **5**, 1373-1379, (1989).
261. Lavrentovich, O. D., Ishikawa, T. & Terentjev, E. M. Disclination loop in Mori-Nakanishi ansatz: Role of the divergence elasticity. *Mol Cryst Liq Crys A* **299**, 301-306, (1997).
262. Mori, H. & Nakanishi, H. On the Stability of Topologically Non-Trivial Point-Defects. *J Phys Soc Jpn* **57**, 1281-1286, (1988).
263. Terentjev, E. M. Disclination Loops, Standing Alone and around Solid Particles, in Nematic Liquid-Crystals. *Phys Rev E* **51**, 1330-1337, (1995).
264. Kleman, M. & Lavrentovich, O. D. Topological point defects in nematic liquid crystals. *Philos Mag* **86**, 4117-4137, (2006).
265. Chuang, I., Turok, N. & Yurke, B. Late-Time Coarsening Dynamics in a Nematic Liquid-Crystal. *Phys Rev Lett* **66**, 2472-2479, (1991).
266. Imura, H. & Okano, K. Friction Coefficient for a Moving Disinclination in a Nematic Liquid-Crystal. *Phys Lett A* **A 42**, 403-404, (1973).
267. Madhusudana, N. V. & Pratibha, R. Elasticity and Orientational Order in Some Cyanobiphenyls .4. Reanalysis of the Data. *Mol Cryst Liq Cryst* **89**, 249-257, (1982).
268. Oweimreen, G. A., Shihab, A. K., Halhouli, K. & Sikander, S. F. Density-Measurements in the Nematic and Isotropic Phases of 5cb and Dilute-Solutions of Tetraethylmethane in 5cb. *Mol Cryst Liq Cryst* **138**, 327-338, (1986).
269. Threlfall, H. S. W. *A Textbook of Topology*. (Academic Press, 1980).
270. P. E. Cladis, W. v. S. *Some Nonlinear Problems inAnisotropic Systems, in Solitons in Liquid Crystals*. (Springer-Verlag, 1991).
271. M. Kleman, O. D. L. *Soft Matter Physics*. (Springer-Verlag, 2003).
272. Geng, Y., Almeida, P. L., Figueirinhas, J. L., Terentjev, E. M. & Godinho, M. H. Liquid crystal beads constrained on thin cellulosic fibers: electric field induced microrotors and N–I transition. *Soft Matter* **8**, 3634-3640, (2012).
273. Seč, D., Porenta, T., Ravnik, M. & Žumer, S. Geometrical frustration of chiral ordering in cholesteric droplets. *Soft Matter* **8**, 11982-11988, (2012).
274. Bezić, J. & Žumer, S. Structures of the cholesteric liquid crystal droplets with parallel surface anchoring. *Liq Cryst* **11**, 593-619, (1992).
275. Kurik, M. & Lavrentovich, O. Topological defects of cholesteric liquid crystals for volumes with spherical shape. *Mol Cryst Liq Cryst* **72**, 239-246, (1982).

276. Robinson, C., Ward, J. & Beevers, R. Liquid crystalline structure in polypeptide solutions. Part 2. *Discussions of the Faraday Society* **25**, 29-42, (1958).
277. Lavrentovich, O. Topological defects in dispersed words and worlds around liquid crystals, or liquid crystal drops. *Liq Cryst* **24**, 117-126, (1998).
278. Tarakhan, O. D. L. a. L. N. Temperature dependence of the surfacetension coefficient at the liquid crystal-isotropic fluid interface. *Poverkhnost(In Russian with English Abstract)* **1**, 39-44, (1990).
279. Ravnik, M., Alexander, G. P., Yeomans, J. M. & Zumer, S. Mesoscopic modelling of colloids in chiral nematics. *Faraday Discussions* **144**, 159-169, (2010).
280. Ravnik, M. & Žumer, S. Nematic colloids entangled by topological defects. *Soft Matter* **5**, 269-274, (2009).
281. Ravnik, M. & Žumer, S. Landau–de Gennes modelling of nematic liquid crystal colloids. *Liq Cryst* **36**, 1201-1214, (2009).
282. Ondris‐Crawford, R., Boyko, E. P., Wagner, B. G., Erdmann, J. H., Zumer, S. & Doane, J. W. Microscope textures of nematic droplets in polymer dispersed liquid crystals. *Journal of Applied Physics* **69**, 6380-6386, (1991).
283. McCamley, M. K., Crawford, G. P., Ravnik, M., Zumer, S., Artenstein, A. W. & Opal, S. M. Optical detection of anchoring at free and fluid surfaces using a nematic liquid crystal sensor. *Appl Phys Lett* **91**, 141916, (2007).
284. Cranston, E. & Gray, D. Formation of cellulose-based electrostatic layer-by-layer films in a magnetic field. *Science and Technology of Advanced Materials* **7**, 319-321, (2006).
285. de Souza Lima, M. M. & Borsali, R. Rodlike cellulose microcrystals: structure, properties, and applications. *Macromolecular Rapid Communications* **25**, 771-787, (2004).
286. Almeida, P. L., Tavares, S., Martins, A., Godinho, M., Cidade, M. & Figueirinhas, J. Cross-linked hydroxypropylcellulose films: mechanical behavior and electro-optical properties of PDLC type cells. *Optical Materials* **20**, 97-100, (2002).
287. Landry, V., Alemdar, A. & Blanchet, P. Nanocrystalline cellulose: morphological, physical, and mechanical properties. *Forest products journal* **61**, 104-112, (2011).
288. Ratna, B. & Shashidhar, R. Dielectric studies on liquid crystals of strong positive dielectric anisotropy. *Mol Cryst Liq Cryst* **42**, 113-125, (1977).
289. Bradshaw, M., Raynes, E., Bunning, J. & Faber, T. The Frank constants of some nematic liquid crystals. *J Phys-Paris* **46**, 1513-1520, (1985).
290. Alison D. Ford, S. M. M., Harry J. Coles. Photonics and lasing in liquidcrystals. *materials today* **9**, 36-42, (2006).